THE UNIVERSITY *of* EDINBURGH

Microwave remote sensing of snow and the lower atmosphere in polar regions

Spencer Edward Read

Master of Philosophy

The University of Edinburgh

School of Geosciences

February 2025

Declaration

I declare that this thesis was composed by myself, that the work contained herein is my own except where explicitly stated otherwise in the text, and that this work has not been submitted for any other degree or professional qualification except as specified.

Spencer Read

February 2025

Abstract

Europe faces an increasing vulnerability to frequent extreme weather events, requiring enhanced predictive capabilities within the high latitudes through improved Numerical Weather Prediction (NWP) models. Currently, limited data availability due to sparse weather station networks prevents high-latitude predictive accuracy. Microwave sounding radiances, notably at 50 and 183 GHz, offer vital atmospheric temperature and humidity profile data, vital for correcting forecast initial conditions. However, challenges arise from variable snow and sea ice emissions, inhibiting data assimilation into forecast models. The refinement of snow emissivity modelling enables atmospheric observation assimilation, thereby improving NWP models.

This thesis presents a coupling of two models to illustrate the assimilation of microwave radiances into NWP models: the Factorial Snow Model (FSM) simulates snow microphysical properties influencing microwave emissions and the Snow Microwave Radiative Transfer (SMRT) model accurately simulates microwave emissivity across frequencies.

Initial research integrates and validates these models using data from Trail Valley Creek (TVC), Northwest Territories, Canada. Comparison of in-situ snow pit data with FSM-generated snowpack profiles reveals a precise simulation of density and snow grain size profiles characteristic of Arctic tundra snowpacks. However, FSM fails to capture variability in snow pit profiles. Coupling FSM with SMRT, simulated brightness temperatures (T_B) at 89 GHz are compared to ground-based radiometer observations. SMRT's superior performance using FSM-simulated snow inputs (mean error: -4.4 K) contrasts with snow pit data (mean error: 11.9 K). Sensitivity tests indicate snow grain size as the most influential factor in snow surface emissivity.

In the thesis's concluding phase, SMRT-driven simulations expand to the NWP grid scale across frequencies from 10.65 to 234 GHz. T_B generally increases with frequency, except at atmospheric window channels (157 and 243 GHz). Spatial variability, frequency-dependent, is minimal at the lowest (≤ 18.7 GHz)

and highest frequencies (≥ 118 GHz) due to reduced scattering. Intermediate frequencies (37 and 89 GHz) exhibit greater spatial variability due to increased snowpack scattering.

In summary, large spatial and temporal variations in Arctic tundra snow emissivity highlight the necessity for precise emissivity simulations grounded in accurately modelled or observed microphysical snow properties. This approach contrasts with the static emissivity values prevalent in many NWP systems.

Lay Summary

Extreme weather in Europe is becoming more frequent, so accurate weather forecasting is becoming more important. Arctic weather patterns strongly influence weather in Europe, so improving weather forecasting in the Arctic has global benefits. Weather forecasting in the Arctic is less reliable due to a lack of weather stations – a key data source for weather models. This can be improved by obtaining data from other sources so that the quality and quantity of data going into models increases. Satellites already provide valuable information about temperature and humidity in the atmosphere. However, poor understanding of snow and ice on the ground limits the use of this data. These satellites use sensors that measure the natural radiation from the Earth, but as they travel through the snow in waves, they scatter which disrupts the readings. The amount of scattering depends on the wavelength or the frequency of the waves and the type of surface they interact with, i.e., snow, ice, water, or soil.

This thesis used two computer models to solve this issue. The first replicates the structure of snow, including properties such as snow grain size and snow density. The second model uses these snow properties to simulate how the Earth's natural radiation behaves at different wavelengths, like satellite sensors but without the interference caused by snow scattering. Both models were tested using data collected during a field campaign at Trail Valley Creek, a research station in the Canadian Arctic.

Results showed that the way snow in the Arctic affects satellite signals can change a lot depending on location and over time. This means that to forecast the weather more accurately, we need more precise measurements of snow properties, like grain size, rather than using fixed values. Applying this approach globally will enhance the accuracy of weather models and help improve predictions of extreme weather across Europe.

Acknowledgements

First and foremost, I would like to thank my supervisor, Richard Essery. His patience, knowledge, and guidance have helped me get through this thesis. It has been a long road, and I am thankful for all his support along the way. I would like to thank the funding bodies, NERC, the E3 DTP, my CASE partner - the Met Office, and the University of Edinburgh for giving me a chance to do this project. All the PGR staff, School of Geoscience staff, and E3 DTP staff at Edinburgh, especially Stephanie Robin, Sophie Ramette, and more recently, Agapi and Mhiri, who have been very patient and supportive of me through some tough times, it was very much appreciated! I met some wonderful people in Edinburgh, and I would like to thank every one of you, especially the Crew lunch crew and E3 DTP gang.

Thank you to everyone I met during my placement at the Met Office. A special thanks to Stuart Fox who not only supervised me during the placement but also throughout my project, giving me regular guidance. I would like to thank Kirsty Wivell for helping me during the placement and beyond and for collaborating with me to write a report for the Met Office. I am grateful to Mel Sandells for the SMRT training and all the help with radiative transfer modelling.

Finally, I want to thank all my family and friends who have supported me throughout the years—especially my Mum and Dad. I wouldn't have been able to complete this thesis without their support. Thank you both for giving me the freedom, encouragement, and confidence to see it through.

Contents

List of Figures

List of Tables

List of Acronyms and Abbreviations

ACF	Autocorrelation Functions
AOIs	Areas of Interest
ARTS	Atmospheric Radiative Transfer Simulator
AWS	Automatic Weather Station
CanSWE	The Canadian Historical SWE dataset
DEM	Digital Elevation Model
DMRT	Dense Media Radiative Transfer
DORT	Discrete Ordinate and Eigenvalue
DSM	Digital Surface Model
ECCC	Environment and Climate Change Canada
ECMWF	European Centre for Medium-Range Weather Forecasts
EM	Electromagnetic
FSM	Factorial Snow Model
IBA	Improved Born Approximation
JMA	Japanese Meteorological Agency
JULES	Joint UK Land Environment Simulator
LW	Longwave Radiation
MAE	Mean Absolute Error
MBE	Mean Bias Error
NASA	National Aeronautics and Space Administration

NCEP	National Centre for Environmental Weather Prediction
NSE	Nash-Sutcliffe Efficiency
NWP	Numerical Weather Predictions
PBIAS	Percent Bias
RH	Relative Humidity
RMSE	Root Mean Square Error
SfM	Structure-from-Motion
SMRT	Snow Microwave Radiative Transfer
SNTHERM	Snow Thermal Model
SSA	Specific Surface Area
SW	Shortwave Radiation
SWE	Snow Water Equivalent
T_B	Brightness Temperature
TVC	Trail Valley Creek
UM	Unified Model
WATCH	WATer and global CHange
WFD	WATCH Forcing Data
WLU	Wilfrid Laurier University

Chapter 1 Introduction

1.1 Introduction

Polar Regions have a sensitive, complex, and variable climate system that is an important component of the global climate system (Goosse et al., 2018; Singarayer & Valdes, 2010). Surface air temperatures in the northern polar regions have increased by more than double the global average in the last two decades, resulting in extensive warming, decline in snow cover, and sea-ice loss (Notz & Stroeve, 2016; Osborne et al., 2018). In contrast, the southern Polar Regions have experienced no significant changes in the east of Antarctica as well as warming and sea ice loss in the west of Antarctica (Jones et al., 2016; Nicolas & Bromwich, 2014)

Arctic amplification of temperature is a complex and widely debated phenomenon. Still, it has been attributed to several positive feedback mechanisms, including reduced albedo due to sea ice and snow cover loss and treeline advance, increased cloud cover in the summer, and increased water vapour in the atmosphere (Pithan & Mauritsen, 2014; Serreze et al., 2009; Stuecker et al., 2018). Such feedbacks have been observed in the Antarctic, but the warming is much weaker due to deep ocean mixing and ocean heat uptake over the Southern Ocean (Collins et al., 2013). The processes that control the changes in climate in the Polar Regions are complex and not yet fully understood (Goosse et al., 2018). In addition, a lack of reliable in-situ data (Williamson et al., 2017) and the quality of reanalysis products (Bitz & Fu, 2008) have resulted in forecast and climate model uncertainty (Blanchard-Wrigglesworth et al., 2017; Flato et al., 2013; Screen & Simmonds, 2013). The need for more data in Polar Regions is becoming increasingly apparent, as shown by the global distribution of weather stations in Figure 1.1. Weather stations are densely distributed in North America and central Europe (Hijmans et al., 2005) and sparse in both polar regions. As a result, the use of remotely sensed data obtained from polar-orbiting satellites is becoming increasingly common.

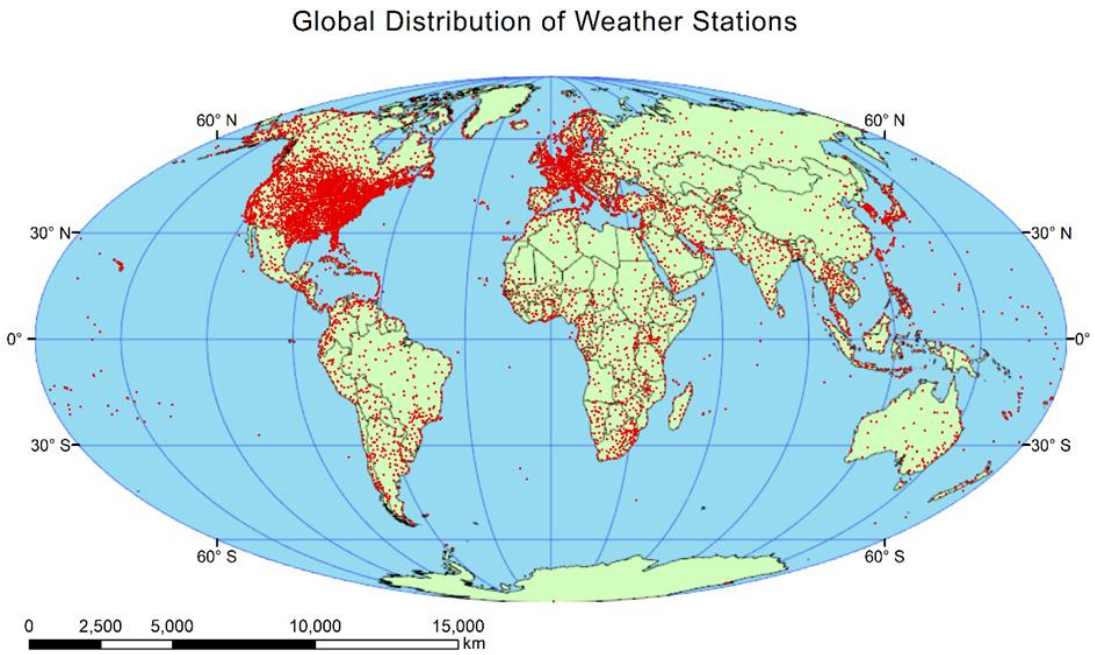

Figure 1.1 Global distribution of weather stations from METAR (airport reports), NEXRAD (weather radar data), radiosonde data, wind profiler data, Airmen's Meteorological Information stations, weather forecasting offices, WMO Radio Frequency Coordination sites, NCEP sites, and Air Route Traffic Control Centres. Data from NCAR is available at: http://www.rap.ucar.edu/weather/surface/stations.txt

Remote sensing is the retrieval of information from an object, without being in direct contact with the object in question (Lillesand et al., 2015). Technological advances have led to remote sensing becoming a popular method for obtaining information in recent years in a wide range of applications, including in meteorology (e.g. Tomlinson et al., 2011), glaciology (e.g. Raup et al., 2014) and hydrology (Tang et al., 2009). Remote sensing uses different wavelengths or frequencies in the electromagnetic (EM) spectrum to detect and record radiant energy emitted or reflected from radiating objects or surfaces) (Lillesand et al., 2015).

The microwave (wavelengths between 1 mm and 1 m or frequencies between 300 MHz and 300 GHz) and optical (wavelengths between 100 nm and 1 mm) parts of the EM spectrum are commonly used in remote sensing as the atmosphere is mostly transparent at these frequencies (Lillesand et al., 2015). However, at optical wavelengths, radiation cannot penetrate clouds (Østby et al., 2014) and reflects off the top of a surface, providing little information on the underlying surface (Kontu, 2018). Clouds do not obstruct microwaves at higher frequencies because they have larger wavelengths, so no or very little

radiation is absorbed by water vapour, dust, etc. (Lillesand et al., 2015). Also, at low microwave frequencies (below ≈ 36.5 GHz), information through the whole snowpack as well as the surface can be obtained (Zheng et al., 2016). At much higher microwave frequencies (between 24 and 183 GHz), atmospheric temperature and humidity profiles can be obtained and assimilated into Numerical Weather Predictions (NWP; English et al., 2000; Harlow, 2009; Liu et al., 2016). This could increase the temporal range of NWP models and eventually improve climate models (Harlow & Essery, 2012)

Polar Regions are dominated by seasonal and perennial snow cover and sea-ice which have highly variable microwave emissivities and temperatures. This can make microwave sounding of the atmosphere at wavelengths, where atmospheric absorption is low, difficult over snow. Therefore, atmosphere observations of temperature and humidity at microwave frequencies over snow-covered surfaces are often absent and are not assimilated in NWP and climate models (Geer et al., 2014). The emissivity of snow and ice is dependent on frequency but also depends on the properties of snowpack such as snow stratigraphy, snow grain type, snow density, and snow depth (Harlow, 2009). Recent advances in microwave radiative transfer theory over snow (Gallet et al., 2009; Picard et al., 2018) have led to the development of models that can separate snow and atmospheric emissivities. Sandells et al. (2017) coupled the microwave emissions model and snow microstructure models to enable the retrieval of snow water equivalent (SWE). Therefore, the coupling of a radiative transfer model and snow model could allow the assimilation of atmospheric observations at microwave frequencies in NWP models, which has been strongly argued for but is yet to be implemented (Bonavita et al., 2017; Karbou et al., 2014)

1.2 Aim, Research Questions and Objectives

The overall aim of the project is to enhance the understanding and predictive accuracy of snowpack and surface microwave emissions in Arctic environments by evaluating and integrating sophisticated snow models (Factorial Snow Model, FSM; Essery, 2015) and microwave emission models

(Snow Microwave Radiative Transfer, SMRT; Picard et al., 2018) through observations and simulations at Trail Valley Creek (TVC) in the Canadian Arctic, with an emphasis on operational scalability and the development of reliable snow and microwave retrieval products. Previous studies have used in-situ snow observations as inputs for SMRT, comparing brightness temperatures (T_B) with ground-based and airborne measurements (Sandells et al., 2024; Wivell et al., 2023). Others have coupled snow models with radiative transfer models and simulated T_Bs at lower frequencies (Sandells et al., 2017) or in alpine regions (Skiles & Painter, 2019). This thesis will build on these approaches by using simulated snow properties to run SMRT at multiple frequencies in the Canadian Arctic, expanding its applicability to high-latitude environments.

1.2.1 Research Question 1

How well can sophisticated snow models reproduce observed snowpack?

1.2.1.1 Objectives

i. Evaluate meteorological forcing data available to determine which are adequate to drive FSM.
ii. Compare FSM outputs with in-situ observations of snow properties.
iii. Assess FSM at a single point in the Arctic (TVC).

1.2.2 Research Question 2

How well can microwave emission models, driven by ground measurements or model predictions of snow structure, simulate airborne observations of surface microwave emissions?

1.2.2.1 Objectives

i. Drive SMRT with snow pit data in the Arctic (TVC).
ii. Obtain T_Bs from SMRT using FSM outputs as driving data at a single point in the Arctic (TVC).
iii. Assess which snow properties affect the simulated T_B.
iv. Compare simulated T_B with ground-based observations.

1.2.3 Research Question 3

How can surface emissivities be predicted with enough accuracy and computational efficiency for operational applications?

1.2.3.1 Objectives

i. Scale FSM and SMRT to run at multiple points across the Canadian Arctic using NWP.
ii. Assess the spatial variability of simulated T_Bs.
iii. Compare T_Bs with surface properties to establish relationships.

1.3 Study Area

The main study area of the project is TVC, a well-characterized Arctic tundra watershed located at approximately 68°44′N, 133°29′W, about 55 km north of Inuvik, Northwest Territories, Canada. The project utilizes ground-based snow microstructure and microwave emissions measurements collected as part of the MACSSIMIZE (Measurements of Arctic Clouds, Snow, and Sea Ice nearby the Marginal Ice ZonE) field campaign. TVC serves as a key research site for studying tundra snow processes, permafrost dynamics, and climate variability in the Arctic.

The land cover at TVC is primarily comprised of continuous permafrost, tundra, and numerous lakes that shape the region's hydrology. Patches of boreal forest and shrubs are present, particularly in lower-elevation areas, with vegetation consisting of low shrubs (≤ 3 m in height), grasses, lichens, and mosses (*Trail Valley Creek Research Station*, 2025). The topography of TVC is highly variable, featuring rolling hills with elevations below 190 m, incised river valleys, and flat upland plateaus. Located at the northern edge of the boreal forest, TVC represents a transitional landscape between boreal and Arctic ecosystems, making it an ideal site for studying climate and snowpack variability. TVC experiences a cold climate, characterized by long winters and short summers, with a mean annual air temperature of -7.9°C (Grünberg et al., 2020).

Snow dominates the landscape for nearly eight months of the year, from October to May, with 66% of the annual precipitation (266 mm) falling as snow (*Trail Valley Creek Research Station*, 2025). Throughout the winter months, the numerous lakes across the region remain completely frozen, contributing to the permafrost-dominated landscape and affecting hydrological processes. This prolonged snow and ice cover significantly influences permafrost conditions, water storage, and energy balance in the region. Given that tundra snow makes up the majority of Arctic snow cover, TVC is an important site for understanding Arctic snow hydrology and climate interactions (Sturm et al., 1995).

The MACSSIMIZE field campaign involved a combination of ground-based and remote sensing measurements to capture detailed snowpack characteristics. Observations included snow microstructure properties, which provide insights into Arctic snowpack dynamics, and microwave emissions monitoring, which is essential for improving remote sensing applications in cold environments. The field campaign also incorporated traditional snow pit measurements to analyse snowpack stratigraphy, while meteorological observations were obtained from two Automatic Weather Stations (AWS) managed by Wilfrid Laurier University (WLU) and Environment and Climate Change Canada (ECCC).

As shown in Figure 1.2a the elevation gradient across TVC, ranging from 21 m to 189 m, is variable with incised valleys, steep slopes, and flat plateaus. The snow pits are located across these elevation changes to reflect the variability. Figure 1.2b shows the land cover consists of shrubs and grasslands with small patches of forest. Numerous lakes in the region will freeze during the colder months.

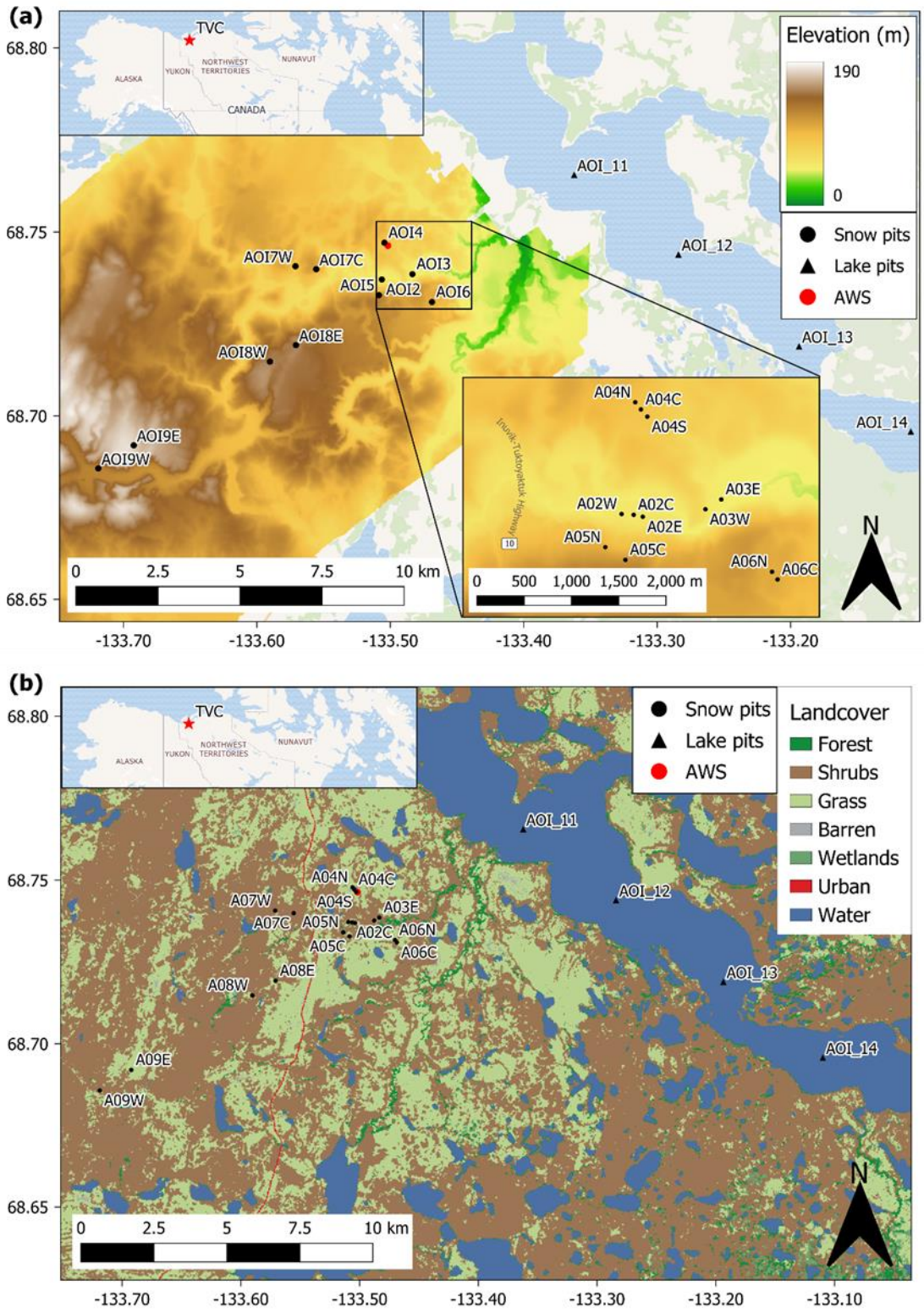

Figure 1.2 Location maps showing (a) elevation (m) and (b) land cover. Snow pit locations are shown in both maps, and the inset map shows the location concerning North America. Landcover data obtained from ('Natural Resources Canada, Canada Centre for Remote Sensing', 2024)

Chapter 2 Meteorological Forcing Datasets

2.1 Introduction

To address Research Question 1 (Section 1.2.1), a robust and comprehensive meteorological forcing dataset is essential to drive the FSM model. This chapter focuses on the critical role of meteorological datasets in climate, snow, and hydrological modelling. It will first explore the challenges of accessing in-situ meteorological data in remote, cold regions such as the Arctic. Next, alternative data sources, including reanalysis products and NWP models, will be discussed and evaluated against in-situ observations. By the end of the chapter, a justification for the choice of dataset to drive FSM for the remainder of the thesis will be provided.

2.1.1 The Importance of Model Forcing Datasets

Physically-based models, whether they are used to simulate climate or snow, require robust meteorological data as inputs (Slater et al., 2013). However, complete meteorological datasets are often unavailable in the most remote regions, either due to the absence of weather stations or instrument failures. This lack of data can severely impact the accuracy of model outputs, particularly in regions like the Arctic, where environmental conditions are extreme and variable.

AWS are a key source of in-situ meteorological data, but they do not always measure all the variables needed to drive physically based snow models. Most of these models require at least six essential meteorological variables: air temperature, precipitation, downward shortwave radiation, downward longwave radiation, wind speed, and relative humidity (Raleigh et al., 2016). However, AWS might not capture all these variables, leading to a disparity between the observations measured and the data needed for accurate snow modelling (Raleigh et al., 2016).

This gap between available and required data necessitates the use of alternative datasets, such as reanalysis datasets (Cucchi et al., 2020; Terzago et al., 2020), NWP output (Förster et al., 2014; Piotrowski et al., 2019),

satellite-derived data (Ma & Pinker, 2012; Zhang et al., 2022) and geostatistical interpolations (Jabot et al., 2012; Sun & Xu, 2021), to fill in missing variables and ensure that the models are driven by the most complete and accurate information possible. Evaluating the quality and completeness of the model forcing datasets is therefore crucial for ensuring the reliability of the simulations, especially in the Arctic. By combining AWS data with reanalysis or other supplementary datasets, it is possible to mitigate the impact of missing data and improve the performance of physically-based models in these remote regions.

2.2 Meteorological Datasets

2.2.1 In-situ Weather Station Data

AWS are an important source of in-situ ground observations in the Arctic. They have the advantage of being able to operate autonomously in remote environments where human presence is limited or impractical. These stations are equipped with sensors to record data on temperature, humidity, wind speed and direction, atmospheric pressure, and sometimes even precipitation and solar radiation.

AWS provide high-resolution temporal data, often at intervals of minutes to hours, which is crucial for understanding the dynamics of Arctic weather patterns and their impact on global climate systems. Moreover, AWS have the advantage of delivering accurate point-based data. This high-resolution, localized data is essential for capturing the specific meteorological conditions at a given location, which is particularly important in the Arctic, where weather can vary significantly over short distances. Unlike satellite observations, which cover broad areas and may lack the fine detail needed for certain analyses, AWS provide precise measurements at a single point, making them invaluable for detailed studies of local climate dynamics. Additionally, AWS can transmit data in real-time or near-real-time via satellite or other communication methods, ensuring that researchers and meteorologists have access to up-to-date information. This capability is vital for validating climate models, studying the effects of climate change in the Arctic, and improving the accuracy of

weather predictions in this sensitive and rapidly changing region. The combination of high-resolution temporal data and accurate point-based measurements makes AWS a powerful tool for advancing our understanding of Arctic weather and its broader implications.

However, AWSs also face several challenges that can affect the quality and reliability of the data they collect. AWSs usually run on batteries connected to solar panels, but battery performance declines in cold temperatures (Pimentel et al., 2010). High winds and low temperatures can cause rime ice to form on equipment, leading to erroneous measurements. At unmanned AWS, these problems can be expensive and time-consuming to fix, and therefore may not be fixed immediately, resulting in incomplete datasets. Specific issues frequently occur with instruments such as precipitation gauges, temperature loggers, and anemometers. Wind measurements are often the most inaccurate measurements (e.g. Stearns et al., 1993). Strong winds and freezing temperatures can damage or freeze up the anemometers, resulting in erroneous zero wind readings and constant wind directions (Lazzara et al., 2012). High winds can also impact pressure measurements by vibrating the instruments and affecting the measurements (Lazzara et al., 2012). Temperature sensors can record erroneously high values if not correctly shielded from radiation and sufficiently ventilated (Lazzara et al., 2012). Precipitation gauges can produce systematic errors due to losses from evaporation and wind (Sevruk et al., 2009).

Meteorological data from an AWS maintained by WLU includes hourly measurements of key atmospheric variables, such as air temperature, relative humidity, precipitation (rain and snow), wind speed, wind direction, and radiation (both shortwave and longwave). This dataset is supplemented by comprehensive metadata, including data quality flags to ensure transparency in measurement reliability. Additionally, an adjacent AWS operated by ECCC (Environment and Climate Change Canada, 2018) provides data on air pressure and offers gap-filling measurements for air temperature, relative humidity, and wind speed. However, as is common in Arctic environments,

these datasets may exhibit gaps due to the challenges inherent in data collection under extreme conditions.

2.2.2 Reanalysis Datasets

In recent years, climate reanalysis products have become important in climate studies (Brönnimann et al., 2018; Lindsay et al., 2014; Rohrer et al., 2018) and climate modelling (Olauson 2018; Albergel et al. 2018; Mizukami et al. 2013). Reanalysis datasets often have high spatial and temporal resolutions, and global coverage of key meteorological variables including air temperature, precipitation, wind speed and direction, humidity, and solar radiation. This makes them useful for studies in areas where observations are sparse, e.g., polar regions, alpine regions, etc. (Raleigh et al., 2016).

A reanalysis produces a high-quality dataset of meteorological variables that are representative of atmospheric states, generated by a constant forecast model and a constant data assimilation system, constrained by observations (Gelaro et al., 2017; Kobayashi et al., 2015; Saha et al., 2010). In the past decades, improved satellite data have meant that reanalysis datasets span from 1979 (the beginning of satellite records) to near real-time (Mooney et al., 2011). Reanalysis products have been produced by many meteorological and climate research centres, including the National Centre for Environmental Weather Prediction (NCEP), the National Aeronautics and Space Administration (NASA), the Japanese Meteorological Agency (JMA), and the European Centre for Medium-Range Weather Forecasts (ECMWF). The next section will discuss the data assimilation methods, forecast model, and observations that are used in ERA-Interim, and how the recently developed ERA5 has improved the quality of the reanalysis product.

2.2.2.1 ERA-Interim

ERA-Interim uses a four-dimensional variational (4D-Var) data assimilation scheme. In each 12-hour cycle, the forecast model performs variational analyses of the upper-air parameters (including temperature, wind, and humidity) and surface parameters (2 m air temperature and 2 m humidity) to obtain a short-range forecast and the initial state of the global atmosphere and

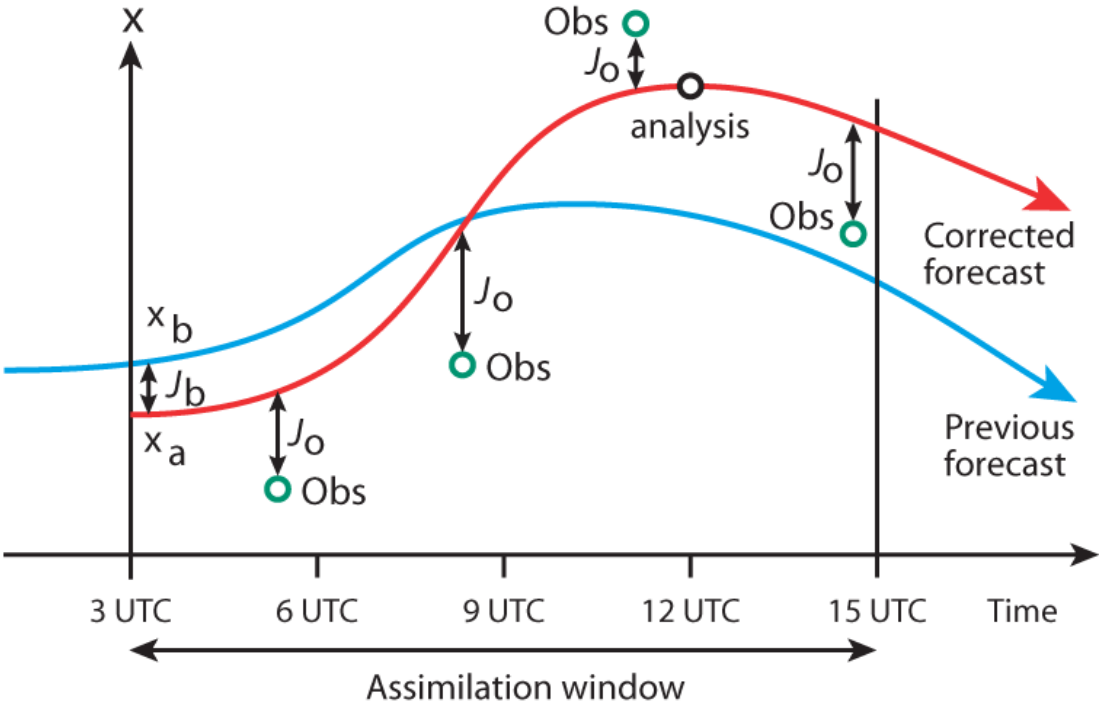

Figure 2.1. Diagram illustrating how 4D-Var assimilates data in ERA-Interim. Parameter X_b represents the initial state of the atmosphere and is compared to observations after a short-range forecast is run in a 12-hour assimilation window. X_a is the modified initial state of the atmosphere after the first forecast is run and J_b represents the fit to X_b. J_o represents the fit to all observations over the assimilation window. Retrieved from (Andersson & Thépaut, 2008).

underlying surface. When all the observations are received in the 12-hour assimilation window, the forecast is adjusted and then rerun. This produces a record of global atmospheric evolution constrained by the forecast model and observations (Dee et al., 2011). This process is shown by the conceptual diagram in Figure 2.1 (Andersson & Thépaut, 2008). ERA-Interim uses the ECMWF Cy31r2 Integrated Forecast System (IFS) forecast model that incorporates the atmosphere, land surface, and ocean waves. The model has a 30-minute time step, a horizontal resolution of 79 km on a reduced Gaussian grid, and sixty layers in the vertical up to the top of the atmosphere at 0.1 hPa.

The number of points on a reduced Gaussian grid changes at different latitudes so that the distance between grid points is approximately preserved (Olauson, 2018).

Observation assimilated in ERA-interim are mainly sourced from satellite datasets, but *in-situ* or conventional datasets are still a crucial constraint on the reanalysis (Thépaut and Kelly, 2006; Dee et al. 2011; Berrisford et al. 2011). Before observations are assimilated, they go through a quality control process that involves data thinning and block-listing. Thinning involves cutting down data that has been duplicated or over-sampled, for example, if a data source has a much higher spatial or temporal resolution compared to the analysis output, the data will need to be thinned. Conventional observations (e.g. land stations, drifting buoys, etc.) are evaluated monthly at station level, and data that systematically deviate from background fields are excluded from the analysis or blacklisted (Tavolato & Isaksen, 2010).

Conventional observations consist of air temperature (upper air and 2 m above the surface), surface pressure, wind speed (u/v, upper-air, and 10 m above the surface), specific humidity (upper-air), and relative humidity (2 m above the surface). These are obtained from a variety of sources including radiosondes, land stations, ships, and drifting buoys. This also includes 2 m temperature, relative humidity, and surface pressure from all SYNOP (Land surface synoptic report) stations. Near-surface wind observations over land, surface pressure observations over high terrain (> 1500 m), and near-surface relative humidity observations at night-time are omitted (Dee et al., 2011). A timeline of all conventional data sources is shown in Figure 2.2.

Satellite datasets have increased the number of observations assimilated into ERA-interim in recent years. Most satellite observations are clear-sky radiances that are converted into T_Bs. In previous ECMWF products (e.g. ERA-40), clear-sky satellite radiance data were affected by instrument and calibration errors, as well as systematic errors present in radiative transfer models embedded in the assimilation system (Dee & Uppala, 2009).

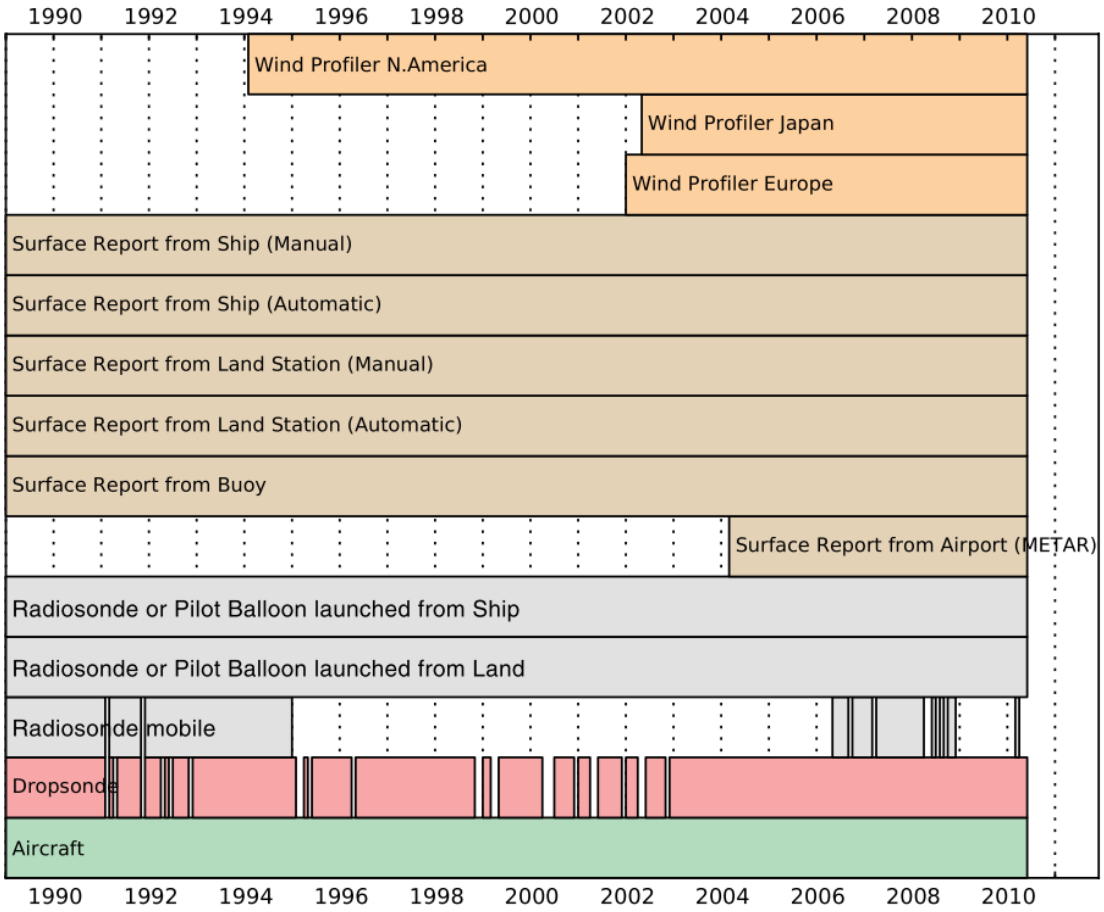

Figure 2.2 A timeline of the in situ or conventional observations assimilated in ERA-Interim. Retrieved from Dee et al. (2011).

ERA-Interim benefits from an automated variational bias correction of satellite radiances within 4D-Var. Radiance data from different satellites, sensors, and channels are calibrated using observations from conventional sources (i.e., radiosondes, land stations, etc.). If few observations are available then the variational bias correction scheme will use uncorrected radiance data, to prevent model background bias from affecting bias corrections (Dee et al., 2011). Improvements in radiative transfer modelling have meant that data from instruments can be directly assimilated into ERA-Interim. This includes simulations of surface emissivity and upper-stratospheric radiances obtained by AMSU-A (Advanced Microwave Sounding Unit A) and SSU (Stratospheric Sounding Unit; Dee et al., 2011). Satellite data is usually blacklisted at the individual channel level to prevent erroneous radiance values from being assimilated, for example, radiance contaminated by the surface or clouds (Tavolato & Isaksen, 2010). In particular, atmospheric sounding data from

microwave satellites over snow-covered surfaces are often excluded from forecast models, including the ECMWF model (Bauer et al., 2016), due to the challenges associated with accurately representing the effects of surface snow (Guedj et al., 2010; Hirahara et al., 2020; Karbou et al., 2014)

2.2.2.2 ERA5

ERA-Interim was replaced by ERA5 (Hersbach et al., 2023) in August 2019. Table 2.1 displays the key differences between ERA5 and ERA-Interim as well as a comparison with other global reanalysis products. Improvements in ERA5 have come as a result of the development of more sophisticated models since ERA-Interim was first released (Hersbach, 2019). ERA5 has much higher horizontal, vertical, and temporal resolutions. A better representation of global precipitation and evaporation has also been noted (Albergel et al., 2018). Dee *et al.* (2011) suggested this is an improvement, as well as noting that soil hydrology and snow will be better represented due to improvement in land-surface models. Variational bias schemes for ozone, aircraft, and surface pressure data have also been implemented, along with the satellite radiance variation bias scheme used in ERA-Interim. Observations have increased from 0.75 million per day on average to 24 million per day in 2018 (Hersbach et al., 2019). Although conventional observations are still a crucial data source, much of the increase in observations has come from new sources of satellite data. ERA5 assimilates all-sky satellite data instead of just the clear-sky satellite data that was used in ERA-interim (Hersbach et al., 2019). ERA5 also assimilates temperature observations from land stations that were previously omitted from ERA-Interim.

Table 2.1 Global reanalysis products. ERA5 will be the only reanalysis product used in this study. For comparison, ERA-Interim, the Modern-Era Retrospective analysis for Research and Applications, Version 2 (MERRA-2), the Climate Forecast System Reanalysis (CFSR), and the Japanese 55-year Reanalysis (JRA-55) have been included. "Present" is near real-time as there is usually a 2–3-month lag.

	ERA5	ERA-INTERIM	MERRA-2	CFSR	JRA-55
SOURCE	ECMWF	ECMWF	NASA	NCEP	JMA
PERIOD COVERED	1979 to present	1979 to 2019	1980 to present	1979 to present	1957 to present
ASSIMILATION SYSTEM	4D-VAR	4D-VAR	3D-VAR	3D-VAR	4D-VAR
HORIZONTAL RESOLUTION	≈31 km ≈0.28^0 x 0.28^0	≈79 km ≈0.75^0 x 0.75^0	≈50 km ≈0.5^0 x 0.625^0	≈38 km ≈0.5^0 x 0.5^0	≈55 km ≈0.56^0 x 0.56^0
VERTICAL RESOLUTION	Surface and 137 Levels to 0.01 hPa	Surface and 60 levels to 0.1 hPa	Surface and 72 Levels to 0.01 hPa	Surface and 64 Levels to 0.266 hPa	Surface and 60 Levels up to 0.1 hPa
TEMPORAL RESOLUTION	Hourly	6-hourly	Hourly	Hourly	3-hourly
REFERENCE	(Hersbach et al., 2019)	(Berrisford et al., 2011)	(Gelaro et al., 2017)	(Saha et al., 2010)	(Kobayashi et al., 2015)

2.2.3 Numerical Weather Prediction Models

NWP models use current weather observations as initial conditions to solve mathematical equations and simulate future weather conditions. They are another important source of meteorological data particularly for hydrological, climate, and snow modelling (Bauer et al., 2015; Billecocq et al., 2024; Fleming et al., 2015). NWP models solve the complex equations governing atmospheric dynamics, thermodynamics, and other relevant processes to generate forecasts. By integrating observational data and physical principles, NWP models produce datasets that are both temporally and spatially detailed, making them invaluable for driving a wide range of models.

NWP datasets are generated through a multi-step process involving data assimilation, model integration, and post-processing. The process begins with

data assimilation, where observational data from sources such as satellites, ground-based stations, and aircraft are integrated into the model to create an accurate representation of the current state of the atmosphere. This initial state is then used as the starting point for model integration, where the NWP model's dynamical core solves the equations of motion and other governing equations to forecast future atmospheric conditions (Bannister, 2017). The output from this integration is a dataset that includes variables such as temperature, wind speed, humidity, and precipitation, typically provided at regular intervals (e.g., hourly, 3-hourly, or daily) over a specified forecast period.

The datasets are often post-processed to correct systematic biases, downscale to higher resolutions, or derive additional variables not directly predicted by the model. For example, the study by James and Benjamin (2020) highlights how commercial aircraft-based observations are used in NWP models to improve global coverage and data quality, particularly during the COVID-19 pandemic when traditional observation networks were disrupted. Similarly, Case et al. (2013) describe the development of a real-time MODIS vegetation product for land surface models, which is integrated into NWP datasets to enhance the accuracy of land-atmosphere interactions.

NWP datasets are used to drive a wide variety of models across different scientific and operational domains. In hydrology, these datasets provide the necessary inputs for models that simulate river flow, snowmelt, and flood forecasting, as demonstrated by Fleming et al. (2015) in their development of a super-ensemble AI flood forecast model. In air quality modelling, NWP datasets are crucial for predicting the dispersion of pollutants, as shown in the study by Gao et al. (2022), which reviews the impacts of aerosol feedbacks on meteorology and air quality in Asia. Additionally, NWP datasets are used in agricultural modelling, where they help simulate soil moisture, evapotranspiration, and crop yields, providing valuable insights for food security and resource management (Hewage & Padmasiri, 2020).

One of the primary advantages of NWP datasets is their high temporal and spatial resolution, which allows for detailed simulations of atmospheric

processes. This resolution is particularly beneficial for applications that require fine-scale inputs, such as localized weather forecasting or regional climate modelling. NWP datasets also offer global coverage, making them suitable for a wide range of applications, from large-scale climate studies to localized environmental assessments. Moreover, the continuous improvement in NWP models, driven by advancements in data assimilation techniques and increased computational power, has led to more accurate and reliable datasets (Smith Sr et al. 2015)

NWP datasets are valuable resources for driving snow and hydrological models, facilitating the simulation and prediction of snowpack dynamics, snowmelt runoff, and hydrological processes. Studies have highlighted the significance of NWP data for driving snow and hydrological models. For instance, Essery et al. (2013) compared various snow models using observed data and emphasised the use of NWP datasets as input for driving snow models.

Despite their strengths, NWP datasets also have several limitations. Model biases, arising from simplifications in physical representations and numerical approximations, can introduce errors in the datasets, affecting the accuracy of the models that rely on them. For instance, Kurzrock et al. (2018) discuss the challenges in using geostationary satellite observations in regional-scale models for short-term cloud forecasting, highlighting the potential biases in NWP models. Additionally, the spatial resolution of NWP datasets, while high, may still be insufficient for capturing small-scale processes in complex terrain, such as mountainous regions, leading to inaccuracies in hydrological and snowmelt models.

Another challenge is the computational cost associated with generating NWP datasets, particularly at high resolutions. This cost can limit the frequency of updates and accessibility for some users, especially in operational settings where real-time data is critical (Waqas et al., 2024). Furthermore, the reliance on observational data for data assimilation can lead to gaps or inaccuracies in

regions with sparse observation networks, impacting the overall quality of the NWP datasets (James et al., 2020).

One of the most widely used NWP models for operational forecasting and climate applications is the Met Office Unified Model (UM).

2.2.3.1 The Met Office Unified Model

The Met Office UM is a numerical weather and climate prediction system developed by the UK Met Office. It is designed to operate across different spatial and temporal scales, making it suitable for short-term weather forecasting, seasonal climate projections, and long-term climate simulations (Walters et al., 2019). Unlike many NWP models that use separate configurations for different forecasting applications, UM integrates multiple atmospheric and surface processes within a single, flexible modelling framework. The UM has spatial resolutions of 1.875° x 1.25° for global climate, 0.14° x 0.09° for global forecasts, and 1.5 km for UK forecasts.

A key component of the UM is the Joint UK Land Environment Simulator (JULES), which serves as its land surface model. JULES simulates energy, water, and carbon exchanges between the land and atmosphere (Walters et al., 2019). This integration enhances UM's ability to represent land-atmosphere interactions, improving hydrological and snowpack predictions. It also improves surface temperature and energy balance simulations, which are crucial for regional weather forecasting and enables the simulation of vegetation growth and carbon cycling, making UM applicable in Earth system modelling.

The continuous improvement of the UM—driven by advancements in data assimilation, cloud microphysics, and turbulence parameterization—has led to more accurate and reliable forecasts, reinforcing its role in both operational meteorology and climate science.

This thesis will utilize NWP data from the Met Office UM (Met Office, 2016) at 1.5 km spatial resolution and hourly intervals between 2nd October 2017 and

1st April 2018 (see Table 2.2). This was a special run for the MACSSIMIZE project.

2.2.4 WFDE5

The WFDE5 (WATCH Forcing Data methodology applied to ERA5 reanalysis data) is a high-resolution, bias-adjusted meteorological dataset designed to support climate impact studies, particularly in the fields of hydrology, agriculture, and environmental modelling. This dataset, developed by Cucchi et al. (2020), offers a spatial resolution of 0.5 degrees and an hourly temporal resolution, which is an improvement over the previous WFDEI dataset that had a 3-hour temporal resolution. The creation of WFDE5 involved applying a well-established bias correction methodology to the ERA5 reanalysis, resulting in a dataset that offers both enhanced temporal and spatial resolution.

WFDE5 was derived by applying the WATCH Forcing Data (WFD) methodology, originally developed for ERA-40 and ERA-Interim, to the ERA5 reanalysis (Weedon et al., 2014). This process involves several key steps:

1. **Aggregation and Regridding:** ERA5 data, originally provided at a resolution of 0.25° x 0.25°, was aggregated to a coarser 0.5° x 0.5° grid to match the spatial resolution used in the WFD methodology. This aggregation was necessary to ensure consistency with previous datasets like WFDEI and to facilitate comparison with other climate models.

2. **Elevation and Bias Correction:** The regridded ERA5 data underwent sequential elevation correction and monthly bias correction. These corrections were performed using observational datasets such as the Climate Research Unit (CRU) TS4.03 and the Global Precipitation Climatology Centre (GPCC) v2018, which provide high-quality reference data for various meteorological variables. The bias correction process adjusted key variables like temperature, precipitation, and radiation to reduce systematic errors and align the reanalysis data more closely with ground observations (Cucchi et al., 2020).

3. **Radiative Forcing Adjustments:** An additional step involved adjusting shortwave radiation fluxes to account for the impact of aerosols, which is not fully represented in ERA5. This was done by incorporating aerosol optical depth data from the CAMS Reanalysis and other sources to correct for aerosol-radiation and aerosol-cloud interactions (Hersbach et al., 2020).

4. **Final Processing:** The final WFDE5 dataset includes hourly data for eleven key meteorological variables, covering the period from 1979 to 2019, with future expansions expected to extend back to 1950 and up to the most recent year. The dataset is available in NetCDF format and can be accessed through the Copernicus Climate Data Store (C3S).

WFDE5 is primarily used for climate impact studies, where accurate meteorological forcing data is critical. The dataset's high temporal resolution makes it particularly valuable for hydrological modelling, where hourly data is necessary to capture the dynamics of water flow and storage (Cucchi et al., 2020). Additionally, WFDE5 serves as a reference dataset for bias-correcting future climate projections, ensuring that simulated future climates are more consistent with observed historical climates. This makes it a crucial tool for studies conducted under initiatives like the Inter-Sectoral Impact Model Intercomparison Project (ISI-MIP; Warszawski et al., 2014), which aims to assess the impacts of climate change across various sectors.

One of the key advantages of WFDE5 is its enhanced accuracy compared to previous datasets like WFDEI. The bias corrections applied during its derivation process significantly reduce errors in critical variables such as temperature and precipitation, leading to more reliable climate impact assessments. The hourly temporal resolution of WFDE5 also represents a significant improvement, providing finer temporal detail that is essential for capturing short-term meteorological events and their impacts (Hersbach et al., 2020)

However, there are also some limitations associated with WFDE5. The aggregation of ERA5 data to a 0.5° x 0.5° grid, while necessary for consistency

with previous datasets, results in a loss of spatial detail. This coarser resolution may limit the dataset's applicability in studies requiring high spatial resolution, such as localized hydrological modelling in regions with complex terrain. Additionally, while the bias correction process improves the overall accuracy of the dataset, it cannot eliminate all sources of error, particularly in regions where observational data is sparse or of low quality (Cucchi et al., 2020)

2.3 Climate of Trail Valley Creek – 1979 to 2019

Figure 2.3 illustrates the seasonal patterns of eight meteorological variables recorded at TVC over 40 years (1979–2019) from WFDE5 dataset. The downward shortwave radiation (SW) exhibits pronounced seasonality, driven by the annual solar cycle at high latitudes. During winter, the polar night results in negligible SW radiation values (0 W m^{-2}). Conversely, the summer months experience a sharp increase, peaking above 250 W m^{-2} in June, before gradually declining through autumn. The absence of SW radiation during winter months highlights the unique climatic dynamics of Arctic regions. Downward longwave radiation (LW), however, remains above zero throughout the year. Although lower during winter months, LW radiation peaks during summer due to increased surface and atmospheric temperatures, reflecting the continuous emission of infrared energy.

Precipitation patterns show distinct seasonal variability. Snowfall rates begin increasing significantly in September as temperatures drop below freezing, remaining elevated throughout the winter. These rates decline gradually in April as temperatures rise, transitioning precipitation from snow to rain. Rainfall rates exhibit an inverse seasonal relationship, with negligible values during winter and peaks occurring during the summer months, particularly between May and September. This inverse relationship highlights the temperature-dependent phase changes in precipitation. Air temperature closely mirrors these trends, exhibiting a predictable seasonal pattern. Winter months are dominated by sub-zero temperatures, often dropping below -25°C, while summer months observe above-freezing conditions between May and

October. This seasonal variation aligns strongly with changes in both SW and LW radiation.

Relative humidity fluctuates throughout the year, with the lowest levels (~55%) recorded during the winter months of January to March. A sharp increase in humidity occurs in May, coinciding with snowmelt and warmer temperatures, before peaking at approximately 85% in September. As snow returns in autumn, humidity levels gradually decline to around 60%. Wind speeds, in contrast, remain stable, ranging between 2.9 and 3.2 m s^{-1}. Minor seasonal variations are observed, with the lowest wind speeds in March and slightly higher values recorded in January and June. Surface air pressure follows a similar seasonal trend, ranging between 999 and 1007 hPa. Low-pressure systems dominate the warmer months (June to October), coinciding with higher humidity and precipitation levels. In contrast, high-pressure systems prevail during winter, corresponding to colder and drier conditions.

These observations highlight the interaction of meteorological variables in shaping the seasonal climatic dynamics of Arctic tundra regions. The distinct seasonal trends in SW and LW radiation underscore the impact of the polar night and prolonged summer daylight on the region’s energy budget. Precipitation patterns reflect the strong influence of temperature on phase changes, with snowfall and rainfall serving as key markers of seasonal transitions. Meanwhile, the consistent wind speeds and pressure patterns emphasize the stability of atmospheric circulation, despite the region's extreme climate variability.

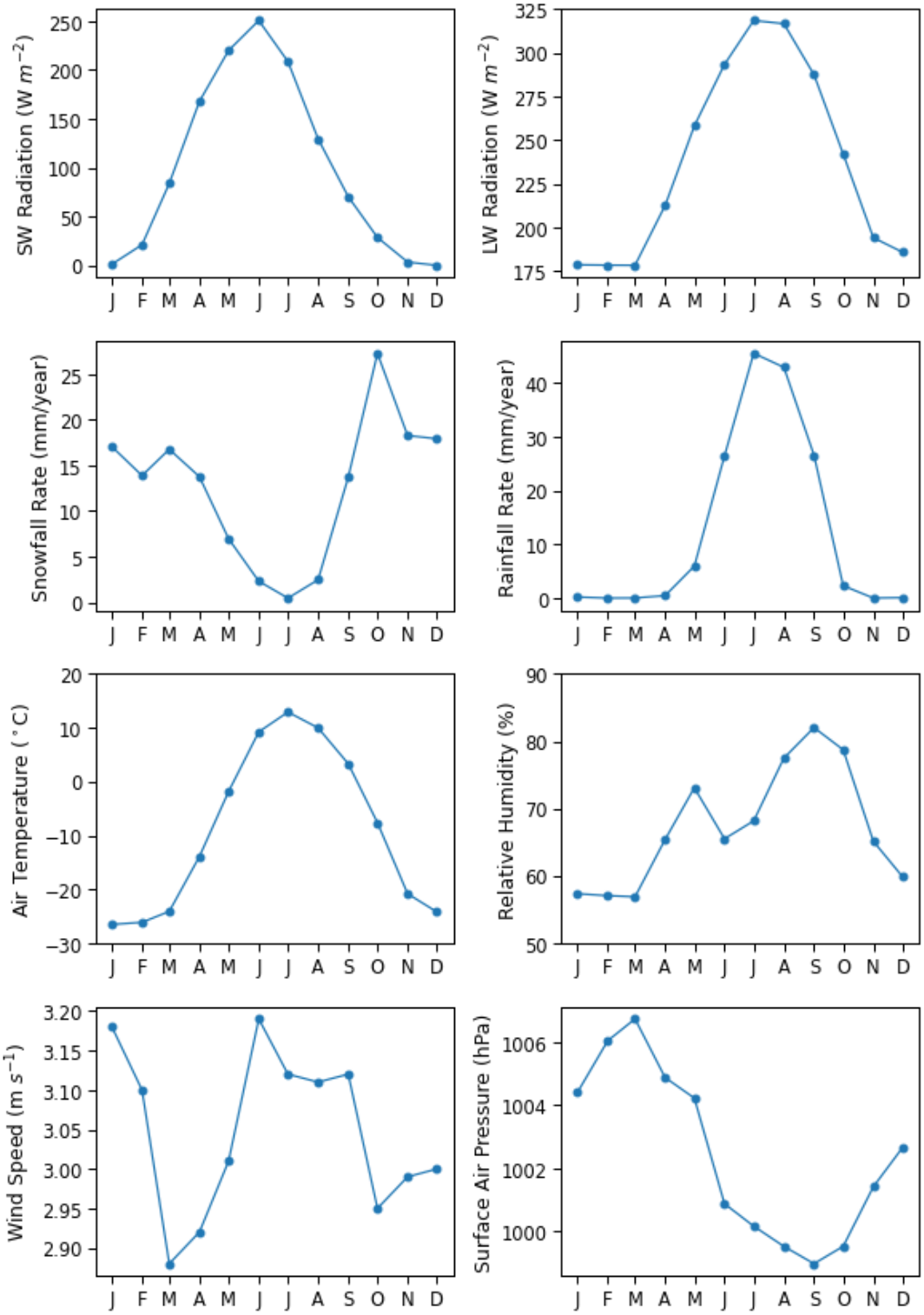

Figure 2.3. Monthly averages (1979-2019) of meteorological variables in Trail Valley Creek, North-West Canada. Data retrieved from (Cucchi et al., 2020)

Figure 2.4 presents trends in eight key meteorological variables for the TVC area in Northwest Canada, using the WFDE5 dataset over the 40 years from 1979 to 2019.

Shortwave (SW) radiation shows a notable decreasing trend, indicating a reduction in the amount of solar radiation reaching the surface. This decline could be attributed to increased cloud cover, atmospheric aerosols, or changes in surface albedo due to snow and ice loss. Meanwhile, longwave (LW) radiation exhibits a strong upward trend, suggesting enhanced atmospheric warming and increased infrared radiation being emitted back to the surface. This is consistent with the greenhouse effect, where rising temperatures and increased water vapour amplify surface warming.

The precipitation data reveal contrasting trends. Snowfall rates have declined significantly over the period, which reflects warming temperatures reducing snowfall, and increasing melt events. In contrast, rainfall rates have increased, indicating a shift in precipitation type from snow to rain as temperatures rise. These patterns align with global observations of Arctic climate change, where warming accelerates transitions in the hydrological cycle. The reliability of these precipitation trends is bolstered by WFDE5's bias adjustment, which improves the accuracy of monthly precipitation totals.

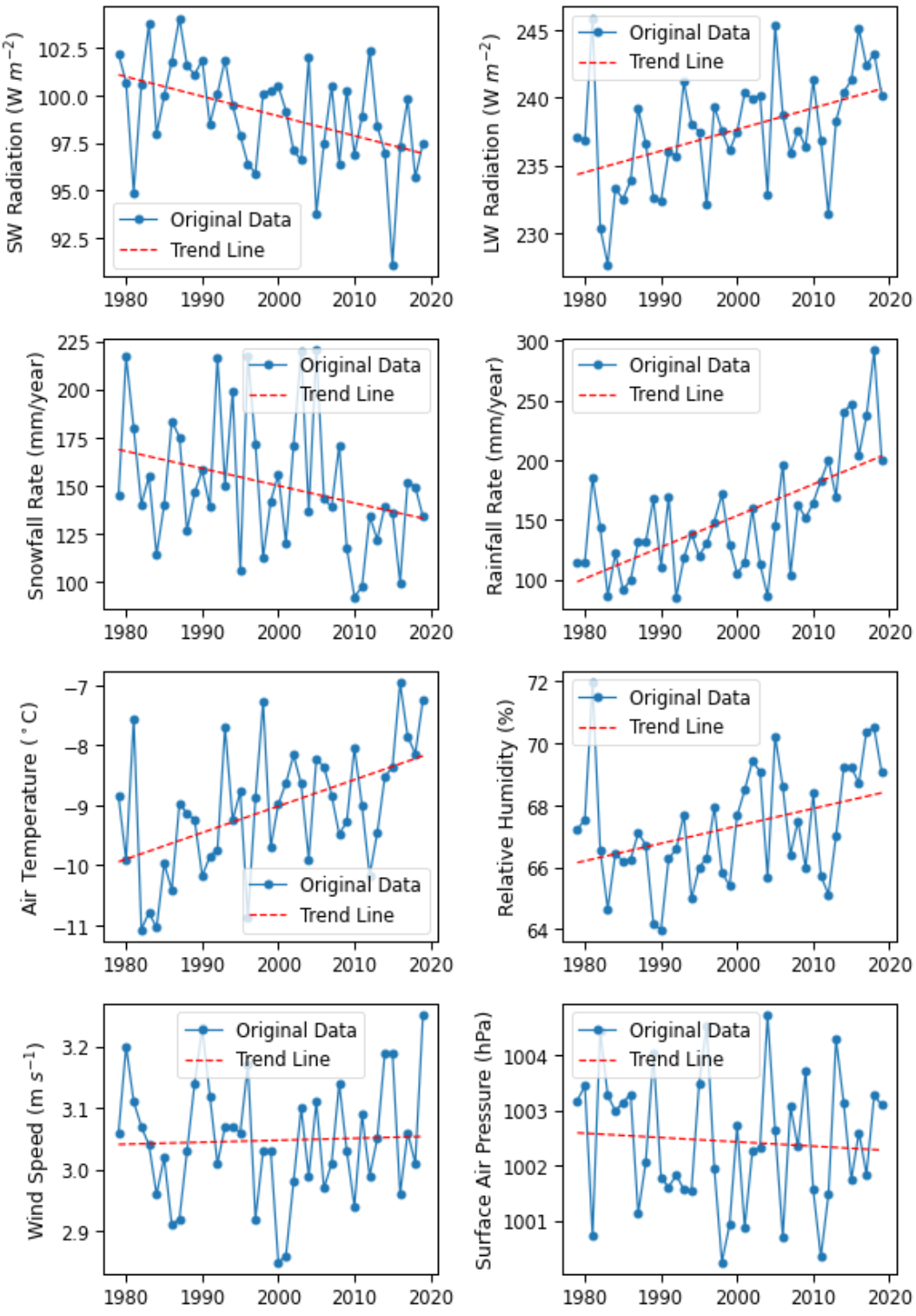

Figure 2.4 Yearly averages (1979-2019) of meteorological variables in Trail Valley Creek, North-West Canada. The red line shows the trend in the data. Data retrieved from (Cucchi et al., 2020).

Air temperature trends further emphasize warming, with a substantial increase over the 40 years. This supports broader evidence of rapid Arctic warming,

where temperatures rise at a rate faster than the global average (e.g. Huang et al., 2017). Relative humidity has also shown a slight upward trend, consistent with warming-enhanced moisture retention in the atmosphere. These trends collectively underscore the intensification of the regional hydrological and energy cycles due to climate change.

Wind speed shows no significant long-term trend, indicating that regional wind dynamics have remained stable during this period. However, localized, or seasonal variations may not be fully captured due to the spatial averaging of WFDE5 data. Surface air pressure shows a slight decrease, which may reflect shifts in atmospheric circulation patterns, potentially tied to larger-scale Arctic climate variability.

In summary, this highlights significant climatic changes in TVC over the past four decades, including warming, altered precipitation patterns, and changes in energy balance.

2.4 Dataset Comparisons

Table 2.2 summarizes the in-situ, assimilated, and modelled datasets discussed earlier in this section. These datasets, ranging from high-resolution in-situ measurements to large-scale reanalysis and modelled data, provide continuous meteorological inputs necessary for snow models and similar simulations throughout the winter period. This section will compare and evaluate the different types of datasets against in-situ measurements, assessing their reliability and suitability for accurate model simulations. Additionally, one of the assimilated or modelled datasets will be selected to gap-fill the in-situ measurements, ensuring a continuous dataset necessary to drive the snow model for a complete winter period.

Table 2.2 Comparison of meteorological forcing datasets available, comparing the spatial resolution and temporal resolution and range.

DATASET	SOURCE	SPATIAL RESOLUTION	TEMPORAL RESOLUTION	TEMPORAL RANGE (UTC)
MIX	Measurements from two weather stations WLU and ECCC at TVC	Point-based	Hourly	2017-10-01 08:00 to 2018-10-01 06:00
ERA5	ECMWF ERA5 Reanalysis Dataset	0.25° (approx. 25 km^2)	Hourly	2017-10-01 08:00 to 2018-10-01 06:00
NWP	Numerical Weather Predictions from Met Office Unified Model	1.5 km^2	Hourly	2017-10-02 00:00 to 2018-04-01 23:00
WFDE5	bias-adjusted meteorological dataset	0.5° (approx. 50 km^2)	Hourly	2017-10-01 08:00 to 2018-10-01 06:00
ERAB	ERA5 variables bias-corrected by quantile mapping to match the statistical distributions of in situ measurement (excluding precipitation)	0.25° (approx. 25 km^2)	Hourly	2017-10-01 08:00 to 2018-10-01 06:00

Figures 2.6-2.9 present a series of scatter plots comparing in-situ observations with estimated datasets for eight meteorological variables in TVC, Canada. Each plot includes key statistical metrics: Pearson correlation coefficient (r), Root Mean Square Error (RMSE), and mean bias error (MBE). Additionally, the number of data points is included, reflecting the incomplete nature of the MIX dataset, which contains 8759 total data points when fully populated. Data points that align closely with the 1:1 line or line of agreement indicate stronger agreement between the in-situ measurements and the estimated dataset, signifying higher accuracy.

2.4.1 Downward Shortwave Radiation

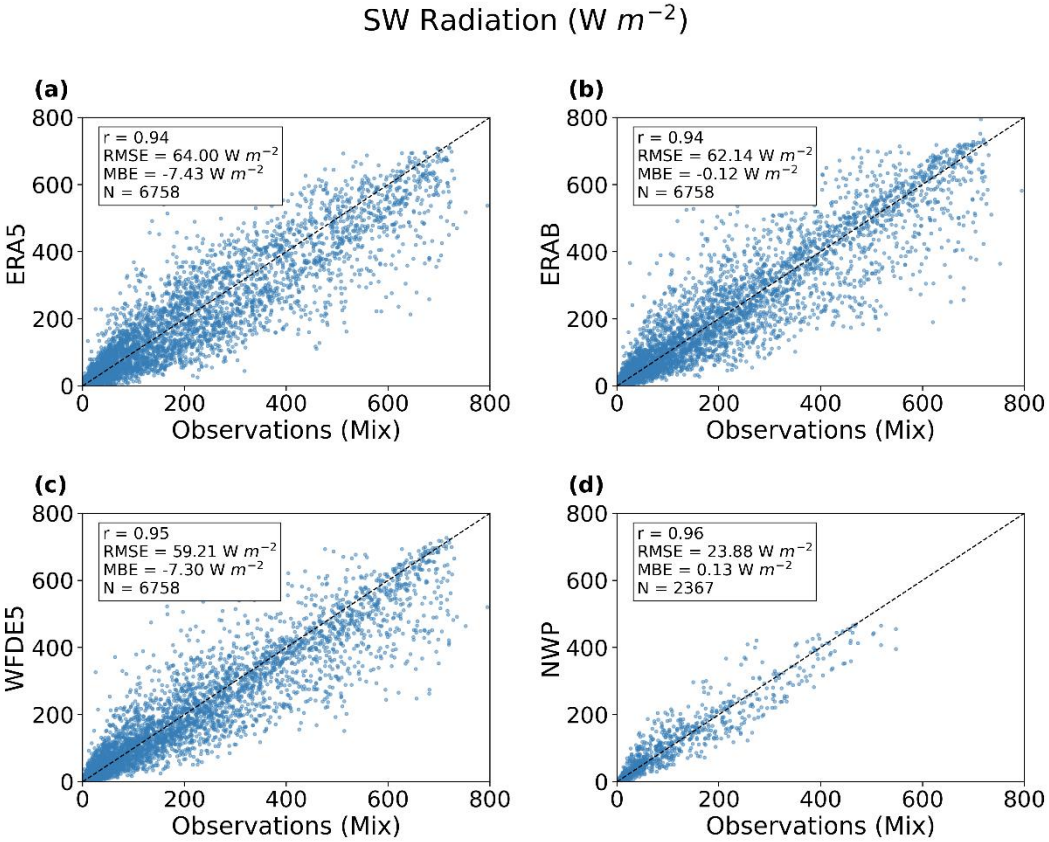

Figure 2.5 Scatter plots comparing in-situ observations of downward shortwave radiation (W m⁻²) with various datasets: (a) ERA, (b) ERAb, (c), WFDE5, and (c) NWP. Each graph displays RMSE, MBE, correlation coefficient, and sample size in the top left. The black line represents the 1:1 correlation.

Figures 2.5a-d show SW radiation. The NWP dataset demonstrates the best performance for SW radiation, with the highest correlation coefficient (r = 0.96), the lowest RMSE (23.88 W m⁻²), and minimal bias (MBE = 0.13 W m⁻²). All

datasets exhibit strong correlations with in-situ observations ($r \geq 0.94$), indicating strong linear relationships. However, the ERA5, ERAb, and WFDE5 datasets show similar RMSE values (59 to 64 W m^{-2}), suggesting variability in their accuracy. Both ERA5 and WFDE5 share a comparable negative mean bias (around -7 W m^{-2}), indicating a tendency to underestimate SW radiation compared to observations, whereas ERAb displays a near-zero bias (MBE = -0.12 W m^{-2}).

Despite NWP's superior performance in terms of correlation and error metrics, its smaller sample size (2367 data points) compared to the other datasets (6758 data points) may limit the robustness of the analysis. Furthermore, the NWP data only spans October 2017 to April 2018, with substantial data gaps during the summer months when SW radiation is expected to be more variable. This seasonal data gap could contribute to the dataset's overall lower variability and improved statistical performance in comparison to the others.

2.4.2 Downward Longwave Radiation

Figures 2.6a-d present the comparison of LW radiation across various datasets. Among them, the bias-corrected ERA5 dataset (ERAb) provides the most accurate representation of LW radiation, closely aligning with the in-situ observations. This is evidenced by its MBE value of nearly zero (MBE = 0.001 W m^{-2}), indicating that the dataset neither underestimates nor overestimates the observations, and its data points are symmetrically distributed around the 1:1 line. Despite this, RMSE of 27.51 W m^{-2} suggests some level of variability in ERAb compared to the observations. Additionally, the moderate-to-high Pearson correlation coefficient ($r = 0.87$) indicates a strong positive relationship between ERAb and the in-situ data.

The ERA5 and WFDE5 datasets also exhibit similar correlation coefficients ($r = 0.87$), highlighting comparable strengths in capturing LW radiation variability. However, the NWP dataset has a weaker correlation ($r = 0.67$), indicating a less robust relationship with the observations. In terms of RMSE, the NWP dataset shows a higher error (41.02 W m^{-2}) compared to ERA5 (31.16 W m^{-2})

and WFDE5 (35.19 W m^{-2}), further reflecting greater variability from the observations.

All three datasets (ERA5, WFDE5, and NWP) exhibit negative MBE, with values of -10.53 W m^{-2}, -14.05 W m^{-2}, and -8.37 W m^{-2} respectively, indicating an underestimation of LW radiation when compared to the in-situ data. The NWP dataset also has fewer data points (N = 3261) due to missing data during the spring and summer months (April 2018 to September 2018), which impacts the robustness of its analysis. In contrast, ERA5, ERAb, and WFDE5 datasets, despite having 14% missing data, still retain a larger sample size (N = 7652), ensuring a more reliable and robust analysis that captures the temporal variability of LW radiation effectively.

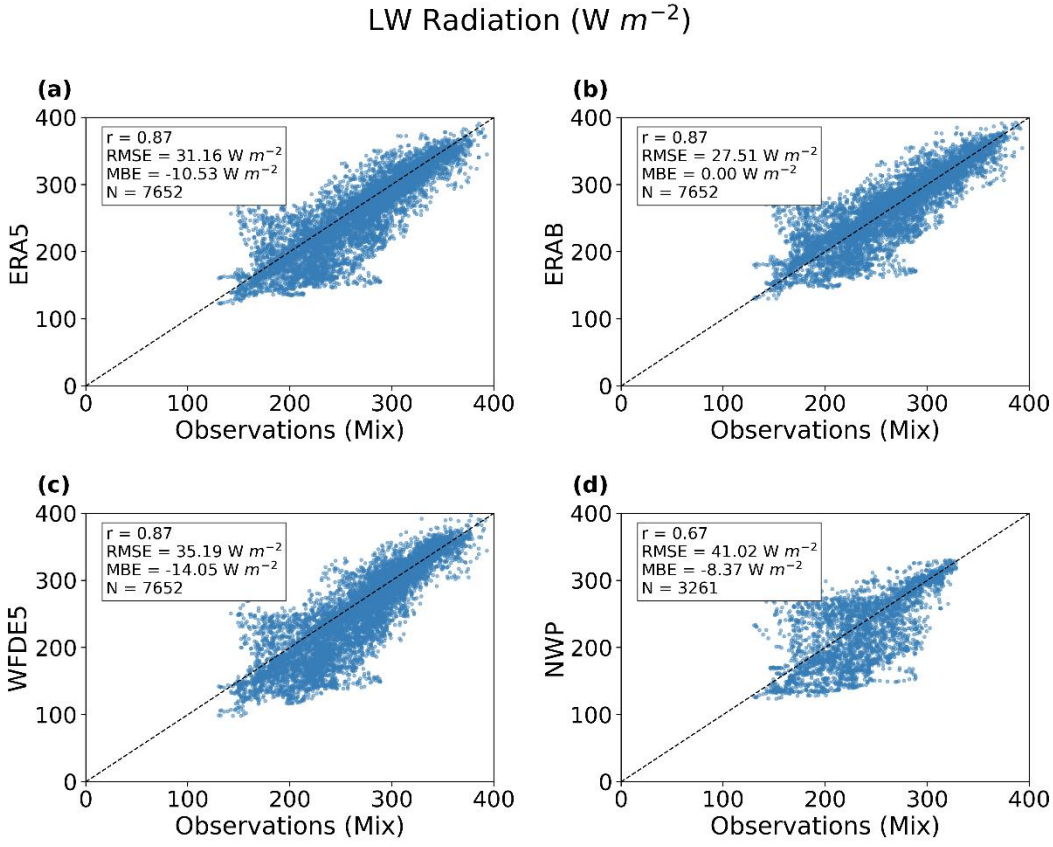

Figure 2.6 Scatter plots comparing in-situ observations of downward longwave radiation (W m^{-2}) with various datasets: (a) ERA, (b) ERAb, (c), WFDE5, and (c) NWP. Each graph displays RMSE, MBE, correlation coefficient, and sample size in the top left. The black line represents the 1:1 correlation.

2.4.3 Air Temperature

Figures 2.7a-d present scatter plots comparing observed Ta with four datasets. Among these, the ERAb dataset provides the most accurate representation of temperature, with a near-perfect correlation coefficient (r = 0.99), minimal variability (RMSE = 2.20 °C), and a negligible warm bias (MBE < 0.01 °C). Similarly, the ERA5 dataset also shows a strong correlation (r = 0.99) and low variability (RMSE = 2.41 °C), although it has a higher warm bias (MBE = 0.7 °C) compared to ERAb. This warm bias in ERA5 has been reported in previous studies, particularly in Arctic regions (Batrak & Müller, 2019; Wang et al., 2019).

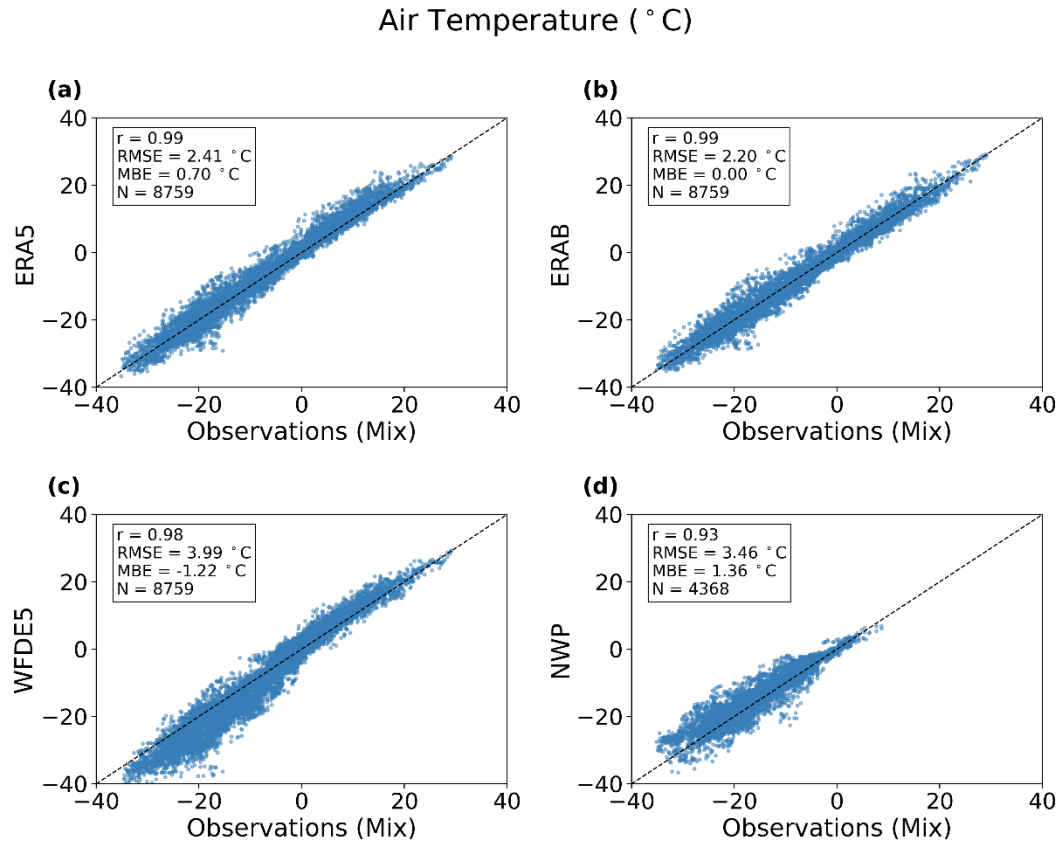

Figure 2.7 Scatter plots comparing in-situ observations of air temperature (°C) with various datasets: (a) ERA, (b) ERAb, (c), WFDE5, and (c) NWP. Each graph displays RMSE, MBE, correlation coefficient, and sample size in the top left. The black line represents the 1:1 correlation.

The WFDE5 dataset also exhibits a strong correlation with observations (r = 0.98); however, it has the highest RMSE (3.99 °C) among the datasets, indicating significant variability compared to observations. Additionally, WFDE5 displays a cool bias (MBE = -1.22 °C), which contrasts with the warm

biases observed in the other datasets and contradicts findings from previous studies (i.e. Abdelhamed et al., 2023).

The NWP dataset has the weakest correlation (r = 0.93) of the datasets but still demonstrates a strong relationship with the observations. The RMSE (3.46 °C) indicates moderate variability, and the pronounced warm bias suggests that the NWP dataset consistently overestimates air temperature relative to observations. This finding is consistent with the warm biases noted in other datasets discussed earlier.

All datasets are complete with no missing data, except for the NWP dataset, which only spans October 2017 to April 2018, as summarized in Table 2.2. This limited temporal coverage likely contributes to the observed differences in performance compared to the other datasets.

2.4.4 Relative Humidity

Figures 2.8a-d display scatterplots comparing observed relative humidity (RH) values with estimations from four datasets (ERA5, ERAb, WFDE5, and NWP). Among these datasets, ERAb demonstrates the most accurate representation of relative humidity, with the lowest RMSE (6.79%) and near-zero mean bias (MBE = 0.03%), indicating a strong agreement with observations and minimal systematic error. The correlation coefficient (r = 0.85) for ERAb suggests a robust positive linear relationship between estimations and observations.

The ERA5 dataset also exhibits robust performance, with a comparable correlation coefficient (r = 0.86) and a relatively low RMSE (7.59%). However, ERA5 shows a moderate negative bias (MBE = -3.93%), suggesting that it slightly underestimates relative humidity compared to in-situ observations.

In contrast, the WFDE5 dataset exhibits the highest RMSE (14.93%) and the largest negative bias (MBE = -10.92%), indicating significant variability and a tendency to underestimate relative humidity. While the correlation coefficient (r = 0.7) remains moderate, it is weaker than those observed for ERA5 and ERAb, highlighting less consistent alignment with the observations.

The NWP dataset has the lowest RMSE (6.69%) among all datasets and displays a small positive bias (MBE = 0.62%), suggesting an overall overestimation of RH compared to the observations. However, its correlation coefficient (r = 0.63) is the weakest among the datasets, reflecting a less consistent relationship with the observations.

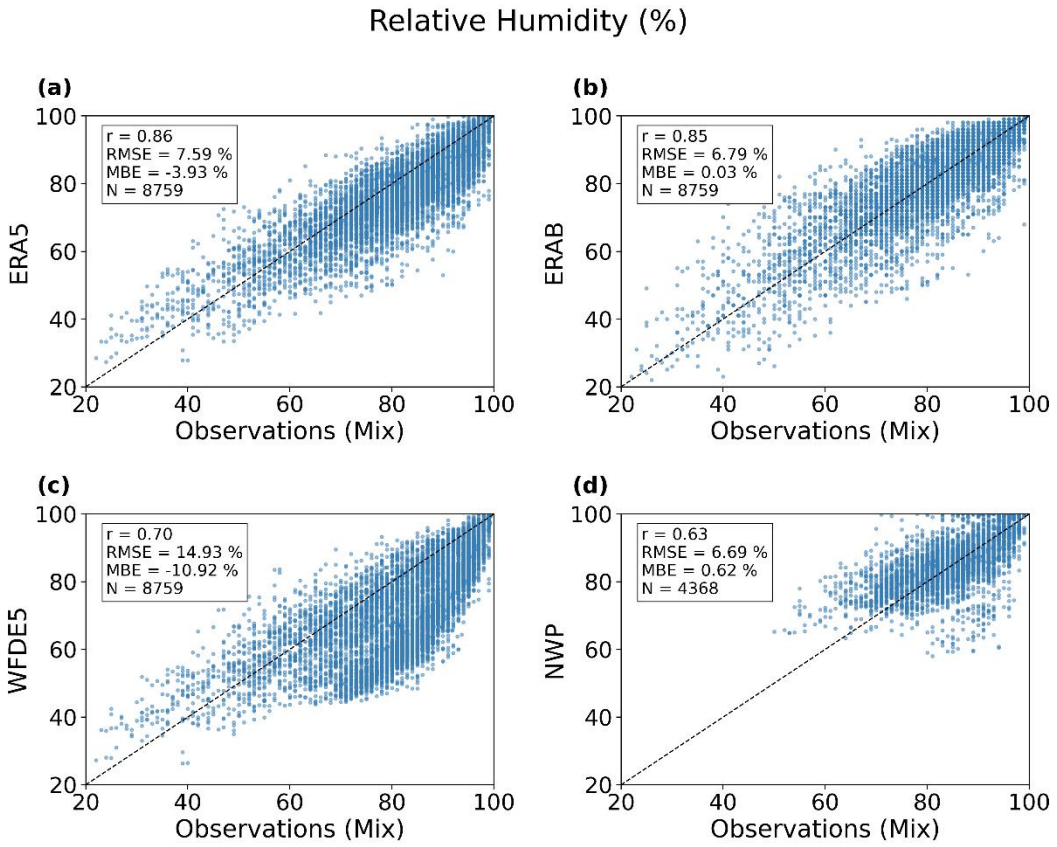

Figure 2.8 Scatter plots comparing in-situ observations of relative humidity (%) with various datasets: (a) ERA, (b) ERAb, (c), WFDE,5 and (c) NWP. Each graph displays RMSE, MBE, correlation coefficient, and sample size in the top left. The black line represents the 1:1 correlation.

2.4.5 Wind Speed

Figures 2.9a-d depict scatterplots comparing observed wind speeds (m s^{-1}) with estimations from four datasets. Among these, ERAb shows the most reliable performance, with the lowest RMSE (2.35 m s^{-1}) and a near-zero mean bias (MBE = -0.07 m s^{-1}), indicating minimal variability and excellent agreement with observations. The correlation coefficient (r = 0.64) for ERAb also reflects a moderate-to-strong positive linear relationship.

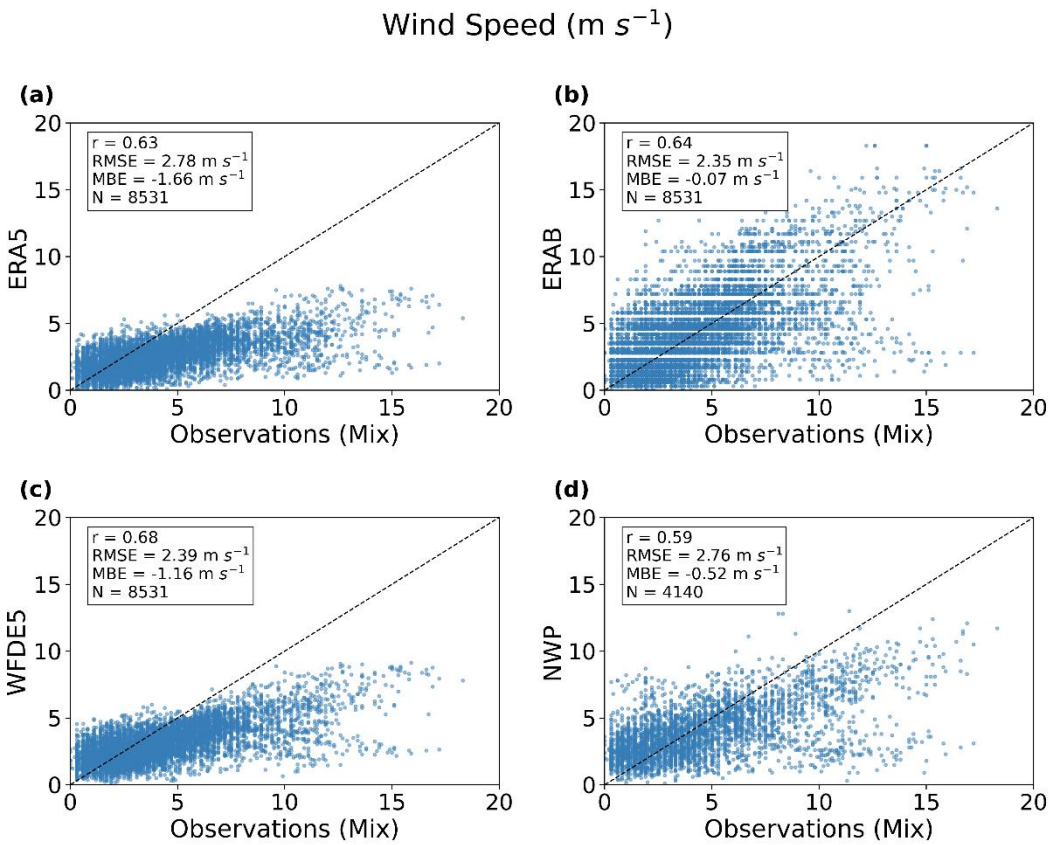

Figure 2.9 Scatter plots comparing in-situ observations of wind speed (m s⁻¹) with various datasets: (a) ERA, (b) ERAb, (c), WFDE5, and (c) NWP. Each graph displays RMSE, MBE, correlation coefficient, and sample size in the top left. The black line represents the 1:1 correlation.

The WFDE5 dataset demonstrates a comparable RMSE (2.39 m s^{-1}) but exhibits a more pronounced negative bias (MBE = -1.16 m s^{-1}), suggesting a consistent underestimation of wind speed compared to observations. Its correlation coefficient (r = 0.68) is slightly stronger than ERAb, indicating better alignment with the variability in the observed data.

The ERA5 dataset shows moderate agreement, with an RMSE of 2.78 m s^{-1} and a negative mean bias (MBE = -1.66 m s^{-1}), indicating a tendency to underestimate wind speed. Its correlation coefficient (r = 0.63) is slightly weaker than that of ERAb and WFDE5, reflecting less consistent alignment with observations.

The NWP dataset has the weakest correlation (r = 0.59) among all datasets, suggesting a less robust relationship with the observations. Although its RMSE

(2.76 m s^{-1}) is comparable to that of ERA5, the dataset exhibits a smaller negative bias (MBE = -0.52 m s^{-1}), which indicates a relatively smaller underestimation of wind speed. However, the smaller sample size (N = 4140) for NWP, compared to the other datasets (N = 8531), likely impacts the robustness of its analysis.

2.4.6 Surface Air Pressure

Figures 2.10a-d present scatterplots comparing observed surface air pressure (hPa) with estimates from the four datasets. Both ERA5 and ERAb exhibit near-perfect correlations (r > 0.99) with observations, demonstrating exceptional agreement. Among these, ERAb stands out with the lowest RMSE (0.74 hPa) and a near-zero mean bias (MBE = 0.04 hPa), indicating it provides the most accurate and consistent representation of surface air pressure.

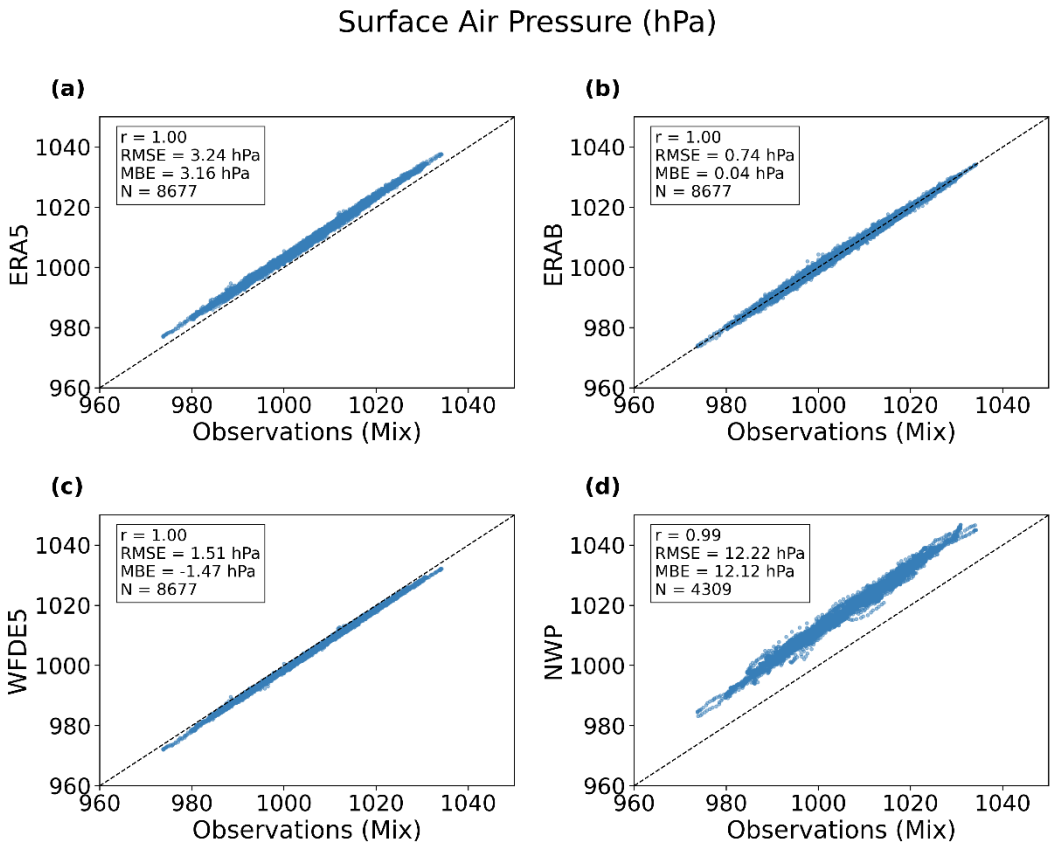

Figure 2.10 Scatter plots comparing in-situ observations of surface air pressure (hPa) with various datasets: (a) ERA, (b) ERAb, (c), WFDE5, and (c) NWP. Each graph displays RMSE, MBE, correlation coefficient, and sample size in the top left. The black line represents the 1:1 correlation.

The WFDE5 dataset also performs well, with a high correlation (r > 0.99) and an RMSE of 1.51 hPa, though it exhibits a slightly low bias (MBE = -1.47 hPa). Despite this bias, its strong linear relationship and relatively low variability make it a reliable dataset for surface air pressure estimations.

The ERA5 dataset demonstrates strong agreement with observations, as evidenced by its near-perfect correlation (r > 0.99). However, it has a higher RMSE (3.24 hPa) and bias (MBE = 3.16 hPa), indicating some overestimation of surface air pressure compared to observations.

In contrast, the NWP dataset has a slightly weaker correlation (r = 0.99) and shows significant variability, as indicated by the highest RMSE (12.22 hPa) among all datasets. Furthermore, it exhibits a pronounced high bias (MBE = 12.12 hPa), highlighting considerable overestimation. The smaller sample size (N = 4140) for NWP relative to the other datasets (N = 8531) likely contributes to its weaker performance.

2.4.7 Precipitation

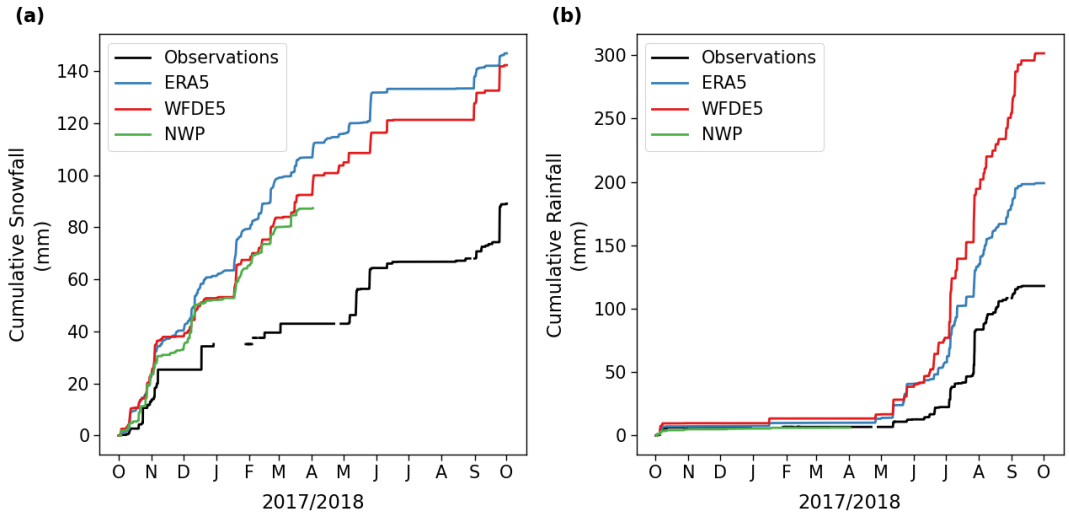

Figure 2.11. Cumulative (a) snowfall and (b) rainfall between October 2017 and September 2018.

Figures 2.11a and 2.11b illustrate cumulative snowfall and rainfall for the period between October 2017 and September 2018, comparing observational data (in-situ measurements, black line) with three datasets: ERA5 (blue line), WFDE5 (red line), and NWP (green line). The NWP dataset only covers

October 2017 to April 2018, while ERAb is excluded due to precipitation not being bias-corrected.

In Figure 2.11a, cumulative snowfall follows a similar trend across datasets and observations from October to mid-November. After this, observations level out with slower but steady accumulation until June 2018, marking the end of the snow season. Model datasets, however, overestimate snowfall significantly after mid-November. ERA5 shows the largest overestimation, followed by WFDE5 and NWP. No snowfall occurred between June and September 2018, a pattern that is consistent across all models, except the NWP dataset which does not have any data beyond April 2018. By October 2018, the modelled datasets showed snow accumulation that was approximately 40-50 mm higher than the observed values. These overestimations, particularly by ERA5, may reflect biases in snowfall parameterization or assumptions about the precipitation phase in models.

In Figure 2.11b, cumulative rainfall exhibits different trends. Rainfall accumulation is minimal during winter months, consistent with the dominance of snowfall, which is well represented in all datasets. Observations show a steady increase starting in May 2018 and peaking in the summer. All model datasets overestimate cumulative rainfall, with WFDE5 showing the largest deviation, followed by ERA5. By October 2018, the modelled datasets had overestimated rain accumulation by approximately 90-190 mm when compared to the observations. The NWP dataset, limited to April 2018, does not capture significant rainfall accumulation. These overestimations in rainfall, particularly by WFDE5, suggest challenges in accurately modelling summer precipitation dynamics. Differences may arise from varying resolutions, land surface schemes, or biases in precipitation generation mechanisms.

Table 2.3 shows statistical metrics relating to the performance of the ERA5, ERAb, WFDE5, and NWP datasets in estimating precipitation compared to observations. The statistical metrics used for this comparison are Pearson correlation coefficient (r), RMSE, and mean absolute error (MAE), Percent Bias (PBIAS) and Nash-Sutcliffe Efficiency (NSE). Each metric has a purpose:

correlation will be used to determine the strength of the relationship between datasets; RMSE and MAE quantify the magnitude of differences between the datasets; PBIAS will determine if the modelled datasets are overestimating or underestimating the observations and NSE will be used to assess how well the model datasets can predict the observations. ERAb has therefore been omitted because precipitation is not bias-corrected and will therefore have the same values as ERA5

For snowfall, all datasets display a weak correlation with observational data, as evidenced by the low correlation coefficients. ERA5 achieves the highest correlation (r = 0.0988), followed by WFDE5 (r = 0.1663), while NWP performs the worst (r = 0.0231). However, all models significantly overestimate snowfall, as reflected in their positive PBIAS values. NWP exhibits the most pronounced bias at 59.31%, while ERA5 and WFDE5 also overestimate snowfall by around 29%. The poor performance is further validated by negative NSE values across all datasets, indicating that the mean of the observational data outperforms the models.

Rainfall modelling shows better performance compared to snowfall, although significant biases remain. WFDE5 achieves the highest correlation (0.4052), followed by NWP (0.3613) and ERA5 (0.3358). Unlike snowfall, NWP performs better in terms of RMSE (0.0392 mm/hour) and MAE (0.0026 mm/hour), while WFDE5 has the largest RMSE (0.2188 mm/hour) and MAE (0.0382 mm/hour). WFDE5 also significantly overestimates rainfall, as seen in its PBIAS of 139.63%. In contrast, NWP slightly underestimates rainfall, with a PBIAS of -14.62%. Notably, NWP is the only model to achieve a positive NSE value (0.1053), indicating better performance relative to the observational mean. These results suggest that while rainfall modelling benefits from better correlation and error metrics compared to snowfall, WFDE5 faces challenges with large overestimations.

These findings suggest that the models struggle to accurately capture precipitation dynamics. As shown in Figure 2.11, the models depict precipitation accumulating at a consistent rate over time, whereas the

observational data reveal a more intermittent pattern, with distinct peaks of precipitation followed by periods of no accumulation. This discrepancy underscores the models' limitations in representing the episodic nature of precipitation events. In addition, localised factors such as topography and vegetation can especially influence snowfall accumulation, which may explain the discrepancies between the observations and model datasets.

Table 2.3 RMSE, MAE, percentage bias, correlation coefficient and Nash-Sutcliffe Efficiency of in-situ observation vs estimate various datasets for snowfall and rainfall

VARIABLE	DATASET	R-VALUE	RMSE (MM/HOUR)	MAE (MM/HOUR)	PBIAS (%)	NSE
SNOWFALL	ERA5	0.099	0.175	0.0247	29.21	-0.043
	WFDE5	0.166	0.174	0.0231	25.52	-0.041
	NWP	0.023	0.246	0.0308	59.32	-0.214
RAINFALL	ERA5	0.336	0.176	0.0279	55.98	-0.090
	WFDE5	0.405	0.219	0.0381	139.63	-0.687
	NWP	0.361	0.039	0.0027	-14.62	0.105

2.5 Chapter Summary

In this chapter, the availability, suitability and accuracy of meteorological datasets for driving physical models, were discussed and evaluated. The main aim was to find a comprehensive meteorological dataset to gap-fill an incomplete in-situ dataset from an AWS at TVC. Alternative datasets including reanalysis, NWP, and bias-adjusted datasets were described and assessed. Using the WFDE5 dataset, the climate of TVC, the study area of this thesis, was analysed over 40 years. This analysis revealed trends such as rising air temperatures, changes in precipitation patterns and changes in the region’s energy balance.

Finally, in-situ meteorological observations were compared to estimations from different sources. The bias-corrected ERA5 reanalysis performed the best with the generally lowest RMSE and strong r-values across all variables. The NWP

dataset performed worst across the variables, due to being an incomplete dataset (that did not run for an entire year). In terms of variables, air temperature and surface air pressure were captured the best with minimal errors and large r-values across the datasets. Most of the modelled datasets were unable to accurately capture precipitation dynamics, showing low r-values and high errors.

As a result of this analysis, the incomplete AWS dataset will be gap-filled using the bias-corrected ERA5 (ERAb) dataset, which will serve as the meteorological forcing data to drive FSM at a point scale. This satisfies the objective of identifying an optimal meteorological dataset for Arctic snow modelling, fulfilling research question 1, objective i (section 1.2.1.1).

Although the NWP dataset showed lower performance at the point scale, its high spatial resolution and domain-wide availability make it suitable for regional-scale simulation, where spatial coverage takes precedence over local accuracy. This dataset will be used to run FSM for multi-point snow simulations across the Arctic, thereby enabling FSM-SMRT coupling at regional scales. This directly addresses research question 3, objective i (section 1.2.3.1).

This chapter demonstrates the importance of accurate and reliable meteorological measurements, particularly for snow, hydrological and climate modelling applications in data-sparse Arctic regions. Modelled datasets, including reanalysis and NWP products, offer reasonable estimates for many variables (e.g. air temperature, humidity, surface air pressure) but require bias correction and quality control to be used effectively.

Conversely, variables like precipitation exhibit strong local variability that is often poorly captured when constrained by coarse model grid resolutions. Even though modelled datasets are only used to gap fill a small portion of in-situ data, their residual inaccuracies may propagate through FSM snow simulations in chapter 3, and influence brightness temperature simulations in chapter 4.

Overall, this chapter highlights the foundational role of accurate meteorological forcing in high-latitude snow emissivity modelling and its implications for satellite data assimilation in operational forecasting systems.

Chapter 3 Snow Datasets and Modelling

3.1 Introduction

Chapter 3 explores the principles and applications of snow models, with a particular emphasis on Arctic tundra snowpack stratigraphy. It covers the physics of FSM, providing a comprehensive analysis of their underlying mechanisms. Additionally, the chapter presents results from FSM simulations conducted at a single point in TVC and on a grid of points covering Alaska and Northwest Canada, offering valuable insights into the model's performance and applicability. These results will be compared with in-situ observations to address research question 1, objectives ii and iii. in section 1.2.1. This chapter will also address research question 3; objective i, outlined in section 1.2.3

3.1.1 Arctic Snowpack Stratigraphy

Snow on the ground has several key properties that significantly impact meteorology, hydrology, and ecology on both global and regional scales. It reflects solar radiation, influencing atmospheric temperatures and climate patterns (Appel et al., 2019; Barrere et al., 2017; Réveillet et al., 2022). Additionally, it acts as a natural insulator, shielding vegetation, soil, and wildlife from extreme temperatures (Berteaux et al., 2017; Domine et al., 2018). Snow also serves as a vital water reservoir, storing moisture that contributes to hydrological cycles upon melting (Barnhart et al., 2016; Pradhanang et al., 2011).

Accurately representing snowpacks in meteorological, hydrological, and ecological models is essential due to their environmental significance. Many snow models, such as CROCUS (Vionnet et al., 2012) have been developed primarily for avalanche forecasting. However, these models struggle to accurately simulate Arctic tundra snowpacks (Domine et al., 2019; Fourteau et al., 2021). Therefore, there is a pressing need for advanced, multi-layered snowpack models capable of capturing the complex physical and thermal dynamics of Arctic tundra snow.

3.1.1.1 Formation and Transformation of a Snowpack

Figure 3.1 illustrates a typical cross-section of a two-layer Arctic snowpack including a depth hoar layer and wind slab layer (Berteaux et al., 2017; Domine et al., 2016).

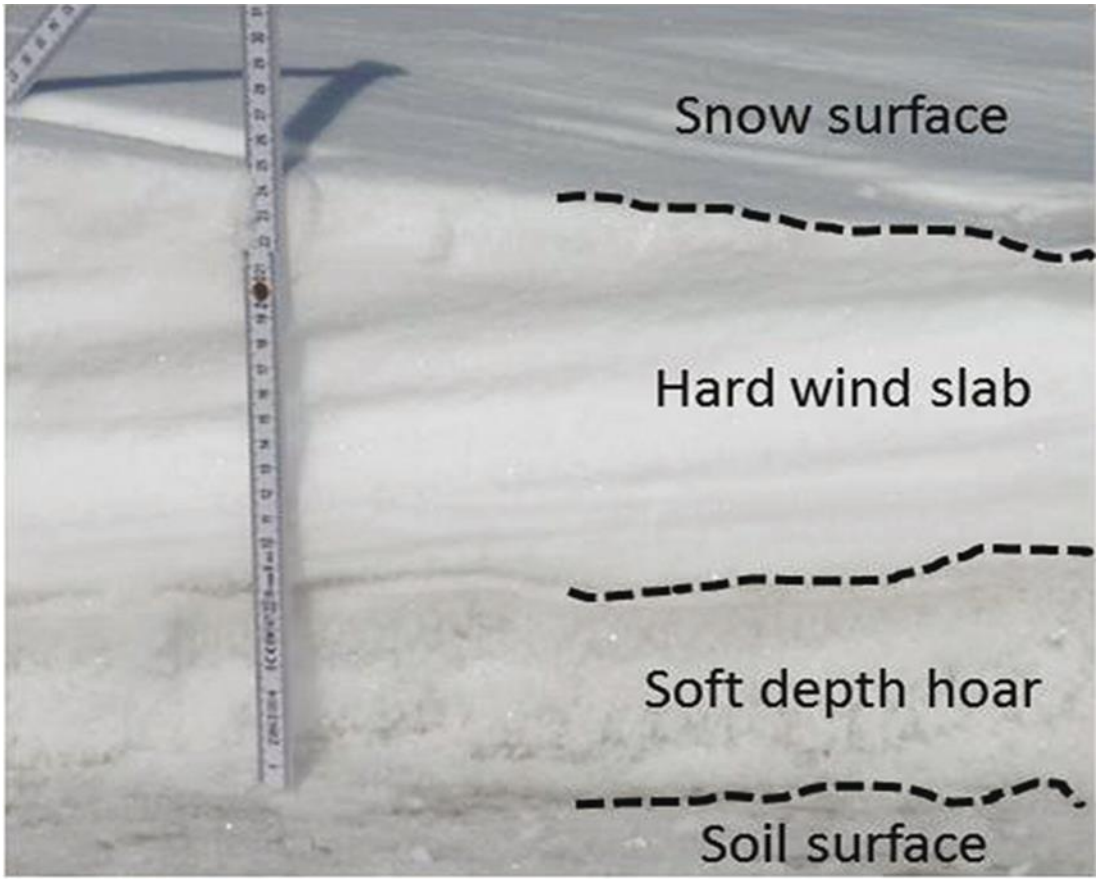

Figure 3.1 Diagram of a typical two-layered snowpack found in the Arctic, including low-density, coarse-grained depth hoar and dense, fine-grained wind slab. Photo: (Berteaux et al., 2017)

In the Arctic, snowpacks form seasonally, beginning in late summer when temperatures drop to 0°C or lower, causing precipitation to shift from rain to snow. The amount of precipitation reaching the ground as snowfall depends on air temperature but is also influenced by atmospheric temperature gradients and the aerodynamic properties of snow crystals (Berteaux et al., 2017). During the early snow season, air temperatures fluctuate above and below 0°C, leading to frequent melting and freezing cycles. However, outside of the summer months (May to September), air temperatures rarely exceed 0°C. As a result, sublimation (where ice transitions directly into water vapour) and

condensation (where water vapour crystallizes into ice) become the dominant mass transfer processes within the Arctic snowpack.

Initially, Arctic snowpacks are shallow (5–10 cm thick), leading to steep temperature gradients of up to 300°C m^{-1}. This occurs because the overlying atmosphere can drop to around −15°C, while the ground beneath remains close to 0°C, insulated by the snow cover. Since water vapour partial pressure is highly temperature-dependent, this extreme gradient drives strong upward water vapour fluxes from the base to the top of the snowpack. Sublimation occurs at the upper parts of snow crystals, with the resulting water vapour condensing onto the lower sections of the crystals above. This continuous vapour transfer — termed "hand-to-hand delivery of water vapour" (Yoshida, 1955) — causes rapid snow grain growth, forming the depth hoar layer. Despite its name, depth hoar develops near the surface early in the snow season. It consists of large, low-density grains, which are structurally weak and too large to be easily eroded or transported by wind.

As the ground cools and the snowpack deepens, temperature gradients weaken, reducing water vapour fluxes and slowing grain growth (Berteaux et al., 2017). This marks the formation of the next layer — wind slab — which develops when intense winds pick up loose, small, rounded snow grains and compact them through sintering. This process creates a denser and more cohesive layer compared to the depth hoar beneath. If recent snowfall occurs and has not yet been redistributed by wind, a fresh snow layer may form on top of the wind slab. This uppermost layer is characterized by soft, low-density snow with small grains.

3.1.2 Heterogeneity of Snow Cover

Arctic tundra environments are characterized by extensive snow cover that exhibits significant spatiotemporal heterogeneity (DeBeer & Pomeroy, 2017). This variability arises primarily from differences in topography and vegetation cover (Derksen et al., 2009). However, in winter, wind plays a dominant role in redistributing snow through erosion, transport, and deposition, further

increasing the complexity of snow cover distribution (Pomeroy et al., 1997). As a result, in-situ measurements and remotely sensed estimates of bulk snow properties—such as snow cover, snow depth and SWE—often fail to fully capture this spatial variability (Bhardwaj et al., 2016; Dong, 2018; Walker et al., 2021). Accurate measurements and estimations of snow properties are essential for a wide range of applications including, flood and drought predictions (Corona et al., 2015; Vionnet et al., 2020), climate monitoring (Brown et al., 2019) and snow melt predictions (Viviroli et al., 2011).

3.2 Snow Datasets

3.2.1 UAS Snow Depth Maps

Walker et al. (2021) employed unmanned aerial systems (UASs) in conjunction with structure-from-motion (SfM) photogrammetry to estimate snow depth in seven areas of interest (AOIs) during the MACSSIMIZE campaign in March 2018 in TVC. Snow depth was derived by calculating the difference between a digital surface model (DSM) generated from SfM photogrammetry and a snow-free LiDAR digital elevation model (DEM) of the same area. The LiDAR DEM had a spatial resolution of 1 m, necessitating the upscaling of the higher-resolution (0.1 m) DSM. Resampling was performed using bilinear interpolation to ensure consistency between datasets (Walker et al., 2021). Comparisons with in-situ measurements demonstrated that the method effectively captured overall snow depth with minimal errors (RMSE = 0.15 m; Walker et al., 2021).

Figure 3.2 presents snow depth maps derived from Walker et al. (2021), capturing the spatial heterogeneity of snow accumulation across different AOIs. Snow depths range from 0 to 4 m, with deeper snow found on leeward slopes of hills, valleys, and shrub patches, while shallower snow is observed in open tundra areas and on frozen lakes, where wind exposure limits accumulation.

In AOI2 (panel a), the snow pits in AO2 are located in an open tundra region where snow is relatively shallow, generally less than 0.5 m. Across the entire AOI2, snow depth is highly variable, reaching a maximum of 4 m, with large snow drifts accumulating along TVC and in shrub patches in the southwest corner. The shallowest snow is found in the northwest corner, where a small frozen lake is exposed to intense winds.

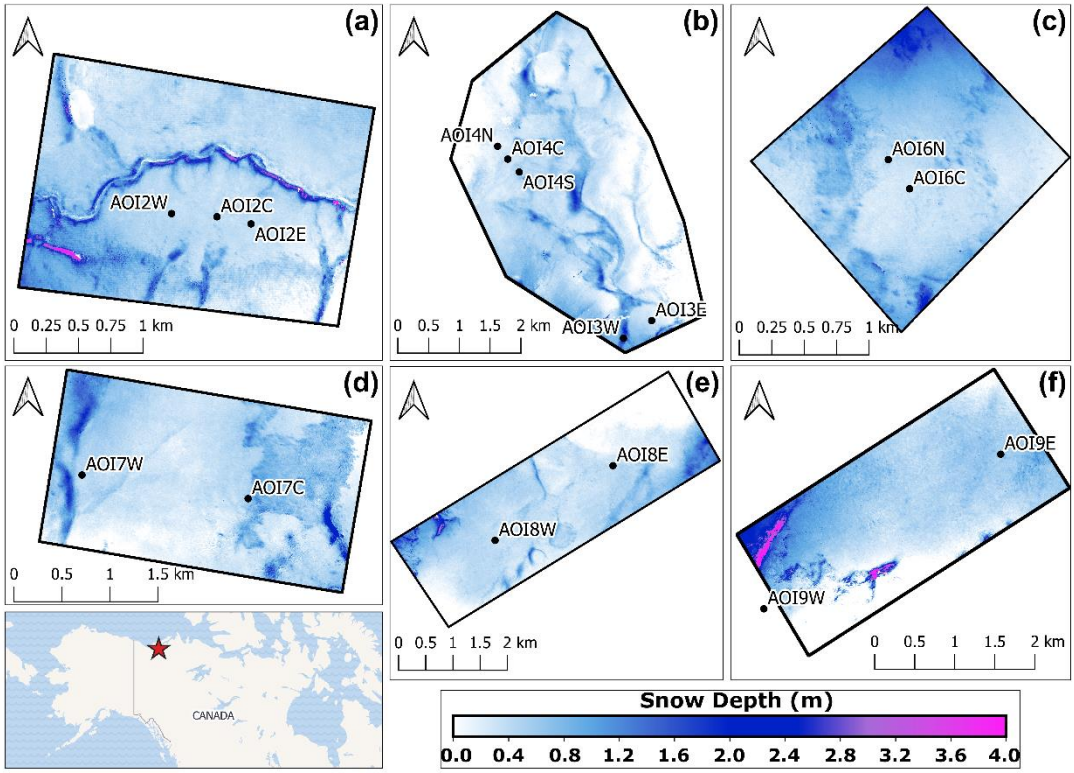

Figure 3.2 Snow depth maps of each Area of Interest (AOI). Snow pits are labelled. Snow depth is measured as the difference between two elevation models, in metres, using unmanned aerial system Structure-from-motion products (Walker et al., 2020) collected between 12 and 20 March 2018. The Inset map shows the location concerning North America.

Panel b includes AOI3 and AOI4, both of which exhibit strong spatial variability. In AOI3, snow depth varies significantly across short distances. AOI3W is situated in a snow drift on a slope where depths exceed 1.5 m, whereas AOI3E, located approximately 0.5 km to the east on flatter terrain, has much shallower snow, with depths of less than 0.5 m. The snow pits in AOI4 are positioned in a more exposed area where snow accumulation is lower, with depths ranging between 0.16 and 0.45 m.

AOI6, shown in panel c, is a relatively uniform snow-covered area, as the region consists of a flat plateau with minimal terrain features to influence snow redistribution. Snow depths at AOI6C and AOI6N are approximately 0.3 m and 0.4 m, respectively, with slight variation across the AOI.

In AOI7 (panel d), snow depth ranges between 0.4 and 1.6 m, with localized snow drifts exceeding 2 m in certain areas. The snow pits AOI7W and AOI7C are located in regions where the snow depth is relatively consistent, around 0.45 m.

AOI8 (panel e) is situated on a high, flat plateau where snow depth varies due to wind redistribution. Leeward slopes accumulate significant snow drifts, while exposed plateau surfaces experience more scouring, resulting in shallower snow cover. Snow depths in this AOI change gradually rather than abruptly, indicating the dominant influence of wind rather than sudden terrain-induced accumulation. Both snow pits, AOI8W and AOI8E, are positioned in shallow snow areas, with depths ranging from 0.28 to 0.35 m.

AOI9 (panel f) exhibits significant snow depth variability, with large regions of deep snow accumulation exceeding 3.2 m. These patterns suggest localized drifting and wind-influenced deposition in response to terrain features. AOI9E, the only snow pit within the mapped area, is situated in a relatively shallow region compared to the rest of AOI9 but still records one of the highest snow depths among the pits, at approximately 0.58 m.

Overall, the snow depth maps effectively illustrate the influence of terrain, vegetation, and wind redistribution on snow accumulation. The deepest snow is found in valleys, leeward slopes, and areas with dense shrub cover, where wind-driven deposition enhances accumulation. In contrast, the shallowest snow is observed in open tundra and on frozen lakes, where intense winds remove snow.

3.2.1 Ultrasonic Snow Depth Measurements

Two ultrasonic snow depth sensors (see Figure 3.3) measure snow depth at TVC. The device is attached to a mast at a known height above the snowpack. An acoustic pulse is sent from a sensor and the time taken for the pulse to reflect off the snow surface and back to the sensor is measured, and snow depth is calculated (Kinar & Pomeroy, 2015). The sensor consists of two key components: a transducer and a thermocouple. The transducer is responsible for converting sound into electrical energy and vice versa, enabling the device to send and receive the acoustic pulses. The thermocouple measures the air temperature around the device, which is crucial for determining the speed of sound in the air. Since the speed of sound varies with temperature, accurate air temperature measurements are necessary to ensure precise snow depth calculations (Kinar & Pomeroy, 2015).

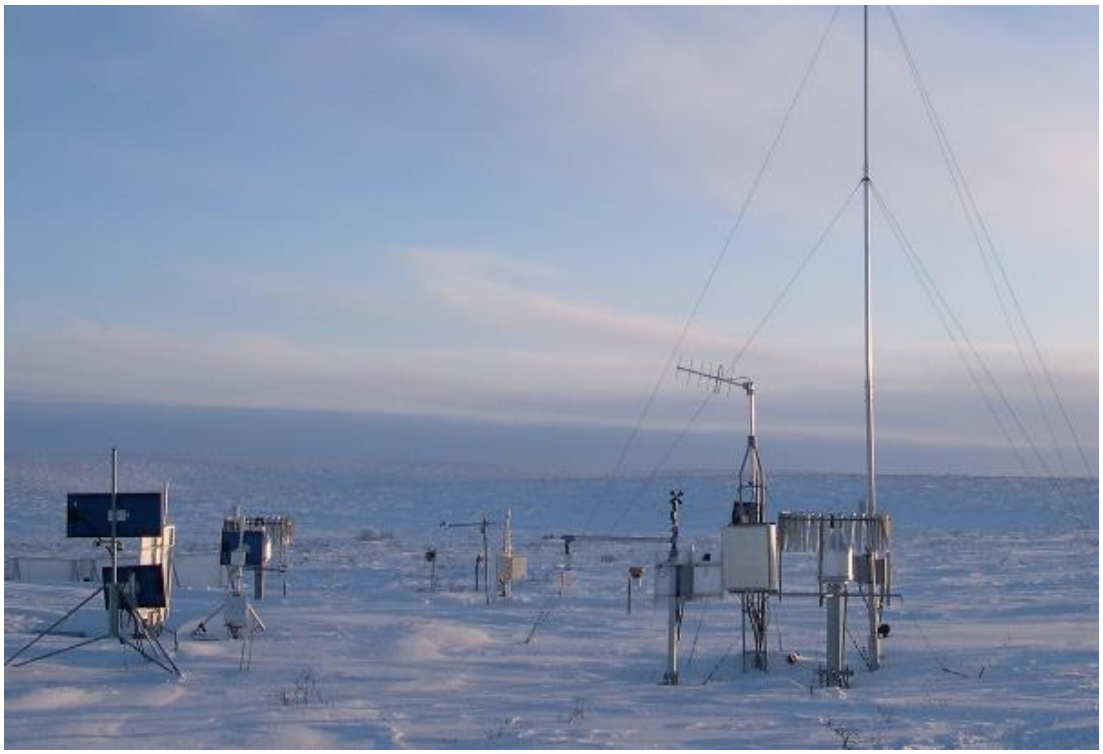

Figure 3.3. Automatic weather stations in Trail Valley Creek (Photo: Richard Essery)

Ryan et al. (2008) used ultrasonic snow depth sensors to measure snow depth at 17 sites in the US and found that the sensors represented the snow depth within 2 cm, although uncertainty in average snow depth from a point measurement will likely be higher than this. However, unreliable

measurements can occur if the sensor is not perpendicular to the snow surface if the transducer is damaged or obstructed, or due to local environmental factors (i.e., intense winds, low density snow, vegetation). For example, low density snow can allow the acoustic wave to penetrate below the snow surface and strong winds can distort the sound of the acoustic pulse (Anderson & Wirt, 2008). Transducers can be damaged or obstructed if dirt or insects get behind the screen that protects the transducer (Anderson & Wirt, 2008). Bergman (1989) found that it is necessary to shield the thermocouple from solar radiation to avoid the air temperature measurement affecting the snow depth measurement. Snow depth is continuously monitored by two in-situ sensors maintained by WLU and ECCC, respectively, with measurements recorded at hourly intervals. However, as is common in Arctic environments, these datasets may exhibit gaps due to the challenges inherent in data collection under extreme conditions.

3.2.2 GlobSnow v3.0 SWE dataset

The GlobSnow v3.0 SWE dataset is part of the European Space Agency (ESA) Snow Climate Change Initiative (CCI) and uses passive microwave satellite SWE data assimilated with ground-based synoptic weather station snow depth observations (Luojus et al., 2021). The dataset contains daily, monthly, and monthly-bias corrected SWE estimates at 25 x 25 km spatial resolution and covers the Northern Hemisphere (above 40°N). Mountain areas are excluded due to known issues with retrieving snow products using this methodology. Shallow snowpacks (< 0.05 m) are not as reliably retrieved and in deeper snowpacks (> 1 m) the algorithm tends to underestimate SWE. The dataset has been comprehensively evaluated against ground truth SWE data in Canada (Luojus et al., 2021) with an MBE of -37.7 mm, an RMSE of 84.6 mm and a correlation of 0.47. These errors were reduced when SWE was below 150 mm.

3.2.3 Canadian Historical SWE Dataset

The Canadian historical SWE dataset (CanSWE) is a comprehensive dataset of SWE and snow depth observations across Canada. The dataset has

extensive temporal coverage (1928-2020) compiled from manual and automated sources, including provincial and federal monitoring networks over 1000 snow courses and a total of 2607 sites (Vionnet et al., 2021). The dataset is useful for validating snow products from other sources such as models or remote sensing. However, much of the data points are in southern Canada, with fewer in northern more remote regions. This impacts its usability in Arctic climate studies.

3.2.4 Snow Pits

Snow pits are very useful for observing the stratigraphy and characteristics of snow layers in a snowpack (Fierz et al., 2009) Snow pits are dug vertically down to the ground and a ‘wall’ is created so measurements can be taken at each layer of the snowpack. These measurements include density, temperature, and grain size and shape. Using a ruler, snow depth is measured from the bottom of the snowpack upwards and layer thickness is marked by the distance from the ground. Layers are usually identified by visual interpretation (Fierz et al., 2009). Density is measured using a cutter that samples each layer of a snowpack. The weight and volume of the cutter are known so the sample is weighed using digital scales and density can be calculated. The accuracy of the density measurement is dependent on the skill and experience of the user (Kinar & Pomeroy, 2015). A thermometer is used to measure the temperature at each layer and produce a temperature of the snowpack. Errors may occur if the thermometer is taken out of the snowpack before the thermometer has settled to the ambient temperature or if the thermometer is taken out of the snowpack to record the temperature (Kinar & Pomeroy, 2015). Grain size and shape are measured using a snow crystal card and magnifying glass. A small sample is taken from each layer in the snow pit and placed on the snow crystal card, which has several grids of assorted sizes. The user must determine which size the sample best fits. The magnifying glass is used to identify the grain shape, based on common snow classification schemes (Fierz et al., 2009). This method relies on an experienced observer but can also be subjective, making it prone to errors (Kinar & Pomeroy, 2015).

Another way to analyse snow structure is by measuring the SSA of snow. SSA and equivalent grain size can be obtained by measuring the optical properties of snow. The DUFISSS (DUal Frequency Integrating Sphere for Snow SSA measurement) is an instrument that measures snow reflectance at 1310 (optimal for SSA < 60 m^2 kg^{-1}) and 1550 nm (optimal for SSA 60 > m^2 kg^{-1}) (Gallet et al., 2009). A snow sample is placed in a black holder attached to the sensor and illuminated with a beam from a laser diode (Gallet et al., 2009). Two sources of error from the instrument will result in underestimated reflectance values. First, low density (typically fresh snow around 30 to 100 kg m^{-3}) snow samples will allow light to penetrate through the snow to the bottom of the sample holder. Also, the light that is reflected by snow grains near the top of the sample is more likely to escape (Gallet et al., 2009)

Snow pits and the instruments used to measure the snow properties that have been discussed thus far are mostly invasive, and therefore all other less invasive measurements should be taken before the snow pit is dug (Kinar & Pomeroy, 2015). Likewise, measurements in a snow pit need to be taken quickly to ensure the sun does not melt the snow (Kinar & Pomeroy, 2015).

Ground data collected during the MACSSIMIZE campaign has been used to compare with simulated snow profiles from FSM. There are twenty-two vertical profiles of snow properties at 8 different AOIs (see figure 1.2). Snow density, temperature and Specific Surface Area (SSA) were measured at 3 cm vertical intervals. A 100 cm^3 gravimetric cutter was used to measure density and SSA was derived from infrared reflectance of snow samples at 1310 nm (Gallet et al., 2009) measured using an A2 Photonic Sensors IceCube. SSA is converted to optical diameter

$$D_O = \frac{6}{\rho_{ice} SSA}, \tag{3.1}$$

where ρ_{ice} is the density of pure ice (917 kg m^{-3} at 0°C; Montpetit et al., 2012).

3.3 FSM

Although FSM and its parametrizations are simple and not entirely new, the model benefits from having a faster run time than previous models (e.g. Essery et al., 2013). The model code is freely available to download, allowing users to modify and extend the code for specific needs (Westermann et al., 2016). The model has been evaluated over winter at an alpine site in France by Essery (2015) and has been used in a study by Alonso-González et al. (2018) to simulate snow depth and SWE.

3.3.1 Snow Mass and Energy Balance

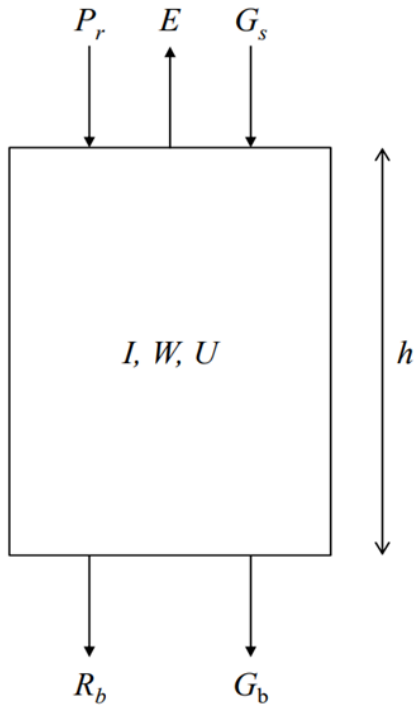

Figure 3.4 A conceptual diagram of FSM for a snow column with height h, ice mass I, liquid water mass W and internal energy U. Precipitation rate P_r, vapour flux E, run off at the base of the snowpack R_b and heat fluxes at the surface Gs and base G_b are all indicated by arrows (Essery, 2015).

FSM is a multi-physics mass and energy balance model of the accumulation and melt of snow (Essery, 2015). The model has five process parametrizations that can be switched on or off using binary digits, giving thirty-two configurations. The five parameterisations are snow albedo, thermal conductivity, snow density, stability adjustment of the turbulent exchange coefficient and liquid water content. Binary digits are used, hence a zero

indicates that the parameterization is switched off and a one indicates it is switched on. FSM assumes a uniform surface layer, and thus only simulates at one point in the horizontal. However, FSM can model vertical snow layers and the soil layers below a snowpack. A system diagram (Figure 3.4) illustrates a conceptual model of a column of snow with a surface area of 1 m^2 and height *h* (Essery, 2015). The system is described by the state variables: ice mass (I); liquid water mass (W); density (ρ) and internal energy (U). Density is a function of internal mass, and the snow column height is calculated by $\rho = h^{-1}(I + W)$. Mass increases as rain or snow falls, indicated by precipitation rate (P_r), and is lost to the atmosphere by the vapour flux (E) and as runoff (R_b) at the base of the snow column. Internal changes in ice and snow mass in the snow column are constrained by the conservation equation

$$\frac{dI}{dt} + \frac{dW}{dt} = P_r - E - R_b. \tag{3.2}$$

The condition $I, W \geq 0$ further constrains the model. Heat fluxes at the surface (G_s) and base of the snowpack (G_b) control the internal energy (U), given by the conservation equation

$$\frac{dU}{dt} = G_s - G_b. \tag{3.3}$$

A subsystem diagram (Figure 3.5) illustrates the internal structure of FSM for a three-layer snowpack, with each internal state variable (W, I and U) described separately and fluxes indicated by arrows. Numerical subscripts indicate layers in the snowpack, one being at the top of the snowpack. Rainfall (R_f) and snowfall (S_f) are now considered as separate inputs to liquid water and ice masses. At the surface, liquid mass fluxes into the snow column are rainfall and surface melt (M), whilst at the base of the snow column, mass is lost due to runoff. Internally, liquid water mass moves between layers due to drainage (R_i) down the snow column and liquid mass is lost to ice mass due to freezing (F_i) in each layer.

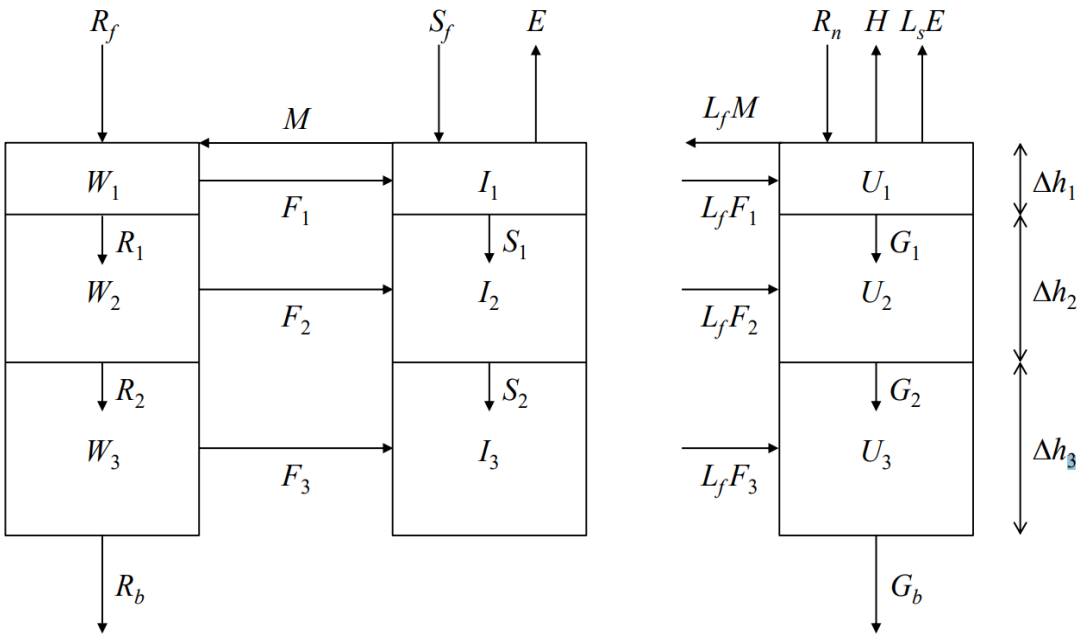

Figure 3.5 A subsystem diagram for a three-layer snowpack relating to conservation equations 3.3, 3.4, 3.7 for ice mass, liquid water mass and internal energy. The fluxes of freezing F, heat conduction G, melting M, drainage of water R and redistribution of ice between model layers are shown and arrows represent the direction of flux. Subscripts indicate layer number i with 1 being at the top of the snowpack. ∆h the thickness of the layer (Essery, 2015).

The snowfall flux increases the ice mass of a snow column at the surface and ice mass is lost due to melting and sublimation. The mass conservation equations for ice are

$$\frac{dI_1}{dt} = S_f - E - M + F_1 - S_1, \frac{dI_2}{dt} = S_1 + F_2 - S_2, \frac{dI_3}{dt} = S_2 + F_3 \quad (3.4)$$

and for water are

$$\frac{dW_1}{dt} = R_f + M - F_1 - R_1, \frac{dW_2}{dt} = R_1 - F_2 - R_2, \frac{dW_3}{dt} = R_2 - F_3 - R_b \quad (3.5)$$

Internal energy (U) is dependent on heat fluxes at the base and surface of the snow column as illustrated in Figure 3.4 and equation 3.3. At the surface, heat

$$G_s = R_n - H - L_s - L_f M \quad (3.6)$$

is added to the snow column by net radiation absorbed by the surface, where L_f and L_s are the latent heats of fusion and sublimation of water, assumed to be constants (0.334×106 J kg^{-1} and 2.835×106 J kg^{-1}).

A surface energy balance equation expresses the net radiation as

$$R_n = (1-\alpha)SW + LW - \sigma T_s^4, \quad (3.7)$$

where α is the albedo of the surface and T_s is temperature (in Kelvin) at the surface. SW and LW are the incoming shortwave and longwave radiation fluxes. The thermal emissivity of snow is assumed to be equal to 1 and the penetration of shortwave radiation through snow is ignored. Energy at the surface is exchanged with the atmosphere by turbulent sensible heat flux (H) and turbulent latent heat flux ($L_s E$). Latent heat is lost at the surface due to melting ($L_f M$). Latent heat is released within the layers due to freezing and heat is conducted between each layer and lost at the base of the snowpack. The energy conservation equations for each model layer are

$$\frac{dU_1}{dt} = G_s - G_1 + L_f F_1, \frac{dU_2}{dt} = G_1 - G_2 + L_f F_2, \frac{dU_3}{dt} = G_2 - G_b + L_f F_3 \quad (3.8)$$

Internal energy and temperature of layer i are related by

$$U_i = C_i T_i \quad (3.9)$$

for

$$C_i = c_{ice} I_i + c_{wat} W_i \quad (3.10)$$

where $c_{ice} = 2100$ JK^{-1} kg^{-1} and $c_{wat} = 4180$ JK^{-1} kg^{-1} are the specific heat capacities of ice and water, respectively.

FSM is run by inputting meteorological driving data and specifying which parametrizations to switch on or off as required. The model has a set of non-linear equations that include the conservation equations (equations 3.4, 3.5, 3.8) and parameterisations. As these equations cannot be solved analytically, they are linearized and then the state variables are updated sequentially at the next time step. Snow albedo is the first variable to be updated. If the thermal conductivity and atmospheric stability factor parameters are switched on, then they will also be updated at this stage. Subsequently, the surface temperature

for the next time step is obtained by solving the surface energy balance equation (equation 3.7), assuming that there is no melt. If the surface temperature at this increment is above 0 °C then it is recalculated assuming that the snow melts. If the surface temperature is now below 0°C the snow only partially melts. The temperature of each snow layer is then updated. Next, if melting and sublimation occur at the surface layer, ice is removed. Liquid increases at the surface due to melting and rain, but if liquid water exceeds W_{max} (the liquid water capacity) in a layer then it drains to the next layer or is lost as runoff at the base of the snowpack. New snowfall has the same temperature as the surface layer and a fixed density depending on the parametrization (100 kg m^{-3} fresh snowfall density if density parameter is on and if switched off a fixed density of 300 kg m^{-3}). The number and thickness of the layers depend on snow depth (see Figure 3.5). In a snowpack that is less than 0.2 m in depth one layer is used, for a snowpack between 0.2 and 0.5 m in depth two layers are used, and if a snowpack exceeds 0.5 m three layers are used. As a default, FSM uses rigid model layers that move with the snow surface, and the lowest layer expands and contracts to accommodate changes in snow depth. The number of layers and thickness of layers is selected within the model parametrisations. FSM also has a deforming layer option that adds a layer to the snowpack when snow falls and removes a layer from the snowpack when it melts. This results in multiple snow layers that preserve discontinuities. With the deforming layers model selected, FSM can also preserve wind slab layers within a snowpack. When this option is selected, the density of freshly fallen snow will depend on air temperature and wind speed. At the right conditions – air temperatures above -25 °C (Li & Pomeroy, 1997) and roughly 5 m/s winds (de Leeuw et al., 2023) – this will result in FSM simulating a high density wind slab within the snowpack.

3.3.2 Snow Grain Size

Snow grain size is key to the mass and energy balance equations (equations 3.2 3.3, 3.4, 3.5, 3.7 and 3.8) that form the basis of FSM (Jordan, 1991). Grain size also affects various snow properties including albedo, scattering, thermal conductivity and permittivity (Lehning et al., 2002). Snow grain growth in a

snowpack is complex and widely debated (Jordan, 1991), but previous studies have shown that the use of SSA to represent grain size reduces model errors (e.g. Grenfell & Warren, 1999). SSA is defined as the surface area of the ice-air interface per unit mass (Hagenmuller et al., 2016). It is another way to characterise snow structure, but also essential for modelling the physical properties of snow (Hagenmuller et al., 2016). Snow metamorphism transforms the structure of fresh snow, changing the snow grain size and shape over short periods. It is a key process when modelling grain size. Snow metamorphism will vary in speed depending on the ambient conditions, particularly temperature.

For dry snow, vapour diffusion causes vapour to condense at the bottom of a grain and sublimate from the top of a grain if temperature decreases with height in the snow (Oleson et al., 2010; Yoshida, 1963). Higher vapour pressure for small particles causes them to sublimate in favour of larger particles (Jordan, 1991). The addition of small quantities of water in a snowpack can significantly increase grain growth (Colbeck & Anderson, 1982). This is because liquid water freezes and connects smaller grains, creating larger grains. At present, grain growth modelling in wet snow is limited to an empirical relationship for the volume growth of grains as a function of the mass fraction of liquid water presented by Brun (1992).

FSM has been modified to incorporate two distinct snow grain growth models. The first is the grain growth model used in JULES and its predecessor, the Met Office Surface Exchange Scheme (MOSES). JULES is a land surface model that incorporates a multi-layer snow scheme that represents snow accumulation, compaction, melt and grain growth. It is coupled with a NWP model and climate models at the UK Met Office, as described in Section 2.2.4.1.

The second grain growth model is from the Snow Thermal Model (SNTHERM; Jordan, 1991), a high-resolution snow physics model designed for detailed snowpack simulations. The differences between these two approaches will be discussed in the next sections.

3.3.2.1 JULES Grain Growth Model

The snow grain growth model used in JULES is based on thermodynamic principles governing snow metamorphism, where grain size changes dynamically due to temperature, humidity, and pressure fluctuations (Best et al., 2011). This prognostic approach contrasts with models that rely on a fixed empirical relationship for grain growth. Grain size increases over time primarily due to two key processes: sintering and sublimation deposition, as described in Section 3.1.1.1. Grain growth is temperature-dependent, with warmer snow layers accelerating grain growth due to enhanced water vapour transport and ice recrystallization.

In JULES, the increment in grain radius δr over a given timestep is determined using the grain area growth rate expressed as:

$$\delta r = g_r r^{-1} \delta t \tag{3.11}$$

where g_r varies depending on temperature conditions:

$$g_r = \begin{cases} 2 \times 10^{-13}\, m^2 s^{-1} & T_{sn} = T_m \\ 2 \times 10^{-14}\, m^2\, s^{-1} & T_{sn} < T_{m,}\, r < 1.5 \times 10^{-4} \\ 7.3 \times 10^{-8} \exp(-4600/T_{sn}) & T_{sn} < T_{m,}\, r \geq 1.5 \times 10^{-4} m \end{cases} \tag{3.12}$$

3.3.2.2 SNTHERM Grain Growth Model

Snow grain growth in SNTHERM is primarily driven by water vapour transport through the snowpack, which depends on the temperature gradient (Sandells et al., 2017). The temperature gradient in a snow layer is calculated as the difference between the top and bottom layer temperatures, divided by the layer thickness.

The temperature at the top of a snow layer, T_s defines the surface layer, while for deeper layers, the temperature is determined as:

$$T_{sn,n-1/2} = \frac{D_{sn,n-1}T_{sn,n} + D_{sn}T_{sn,n-1}}{D_{sn,n} + D_{sn,n-1}} \tag{3.13}$$

for $n > 1$, and the temperature at the base of the snowpack is:

$$T_{sn,n+1/2} = \frac{D_{sn,n-1}T_{sn,n} + \Delta z_{sl,1}T_{sl,1}}{D_{sn,n} + \Delta z_{sl,1}} \tag{3.14}$$

for $n = N_{snow}$.

SNTHERM represents grain growth through three key metamorphic processes (Corona et al., 2015):

1. Destructive metamorphism – Occurs at warmer temperatures, where mechanical compaction and overburden pressure cause grains to break down into smaller sizes. This process is governed by snow viscosity.
2. Constructive metamorphism – Occurs at colder temperatures, where sublimation and deposition cause ice crystals to grow, leading to an increase in grain size.
3. Melt metamorphism – Alters grain size due to the presence of liquid water, which facilitates grain bonding and coarsening.

The vertical vapour flux in a snow layer, which governs mass transfer during metamorphism, is given by:

$$q_v = 9.2 \times 10^{-5}\left(\frac{T_{sn,n}}{T_m}\right)^6 \frac{\partial \rho_{sat}}{\partial T}\left(\frac{T_{sn,n-1} - T_{sn,n+1/2}}{D_{sn,n}}\right) \tag{3.15}$$

where the derivative of saturation vapour pressure with respect to temperature is:

$$\frac{\partial \rho_{sat}}{\partial T} = \frac{e_0}{R_{wat}T^2}\left(\frac{L_s}{R_{wat}T} - 1\right) exp\left[\frac{L_s}{R_{wat}}\left(\frac{1}{T_m} - \frac{1}{T}\right)\right] \tag{3.16}$$

This formulation highlights SNTHERM's ability to explicitly model water vapour transport, a key driver of grain growth under temperature gradient metamorphism.

SNTHERM calculates the grain area growth rate as:

$$g_r = \begin{cases} 1.25 \times 10^{-7} min(|q_v|, 10^{-6}) & \theta_w < 10^{-4} \\ 10^{-12} min(\theta_w + 0.05, 0.14) & \theta_w \geq 10^{-4} \end{cases} \quad (3.17)$$

where θ_w represents the volumetric liquid water content in the snow, defined as:

$$\theta_w = \frac{W}{\rho_{wat} D_{sn}} \quad (3.18)$$

As in JULES, snow albedo is a function of grain size, meaning larger grains reduce reflectivity, leading to higher solar absorption and increased melting. However, SNTHERM provides a more detailed representation of snow physics, also calculating shortwave and longwave radiation, sensible and latent heat fluxes, and ground heat flux.

SNTHERM has been tested against observed snow grain size measurements. Sandells et al. (2017) found that SNTHERM overestimates grain size, while Corona et al. (2015) reported that SNTHERM underestimates grain size and fails to capture observed grain size variability. These discrepancies suggest that SNTHERM's parameterizations introduce uncertainties, with performance varying based on environmental conditions and input datasets.

3.4 FSM Simulations

In this section, FSM is driven by AWS data that has been gap-filled with bias-corrected ERA5 reanalysis data (see chapter 2). The outputs include bulk snow properties such as snow water equivalent (SWE) and snow depth as well as snow layer properties including layer thickness, temperature, snow grain radius, snow density and liquid water content, and soil temperature.

3.4.1 Snow Profiles

Figures 3.7-3.9 compare observed snow grain size, snow density, and snow temperature profiles from snow pit measurements with FSM simulated profiles run with different model configurations at 10 selected sites. The AOIs selected represent a variety of terrains (see figure 1.2) but are also the sites used for SMRT simulation comparisons in chapter 4. The other AOI profiles with FSM simulations are in Appendix A. Due to the heterogeneous snow cover in the region, as shown in figure 3.3, observed snow pit depth differs between the sites, whereas simulated snow pit depths would remain constant because FSM is run with meteorological inputs at a single point. To overcome this, the snowfall rate is scaled before FSM is run to achieve similar snow depths to the observations. AOI3W is on a different height scale from the other snow pits as it was significantly deeper than the other snow pits.

3.4.1.1 Snow Grain Size

Figure 3.6a-j compares simulated snow grain size from the JULES and SNTHERM grain growth models with snow pit measurements of snow grain size. The observed snow grain size profiles exhibit significant spatial variations which are unable to be captured by FSM. In general, the JULES model underestimates snow grain size at every site and never goes above 0.2 mm. Overall, JULES is a reasonable representation of snow grain size and can capture the smaller grains near the top of the snowpack but is unable to reproduce the larger-grained depth hoar near the base of the snowpack. The exception is AOI3W (panel e) where JULES mostly overestimates grain size (> 0.2 mm) but is like the observations at the base of the snowpack.

In contrast, the SNTHERM model overestimates snow grain size consistently across all AOIs. SNTHERM can simulate the general structure of Arctic snowpack, with coarser grains at the base and smaller grains at the top. Sandells et al. (2017) noted that SNTHERM grain sizes were too large and JULES grain sizes were too small in their study coupling snowpack models with microwave emission models.

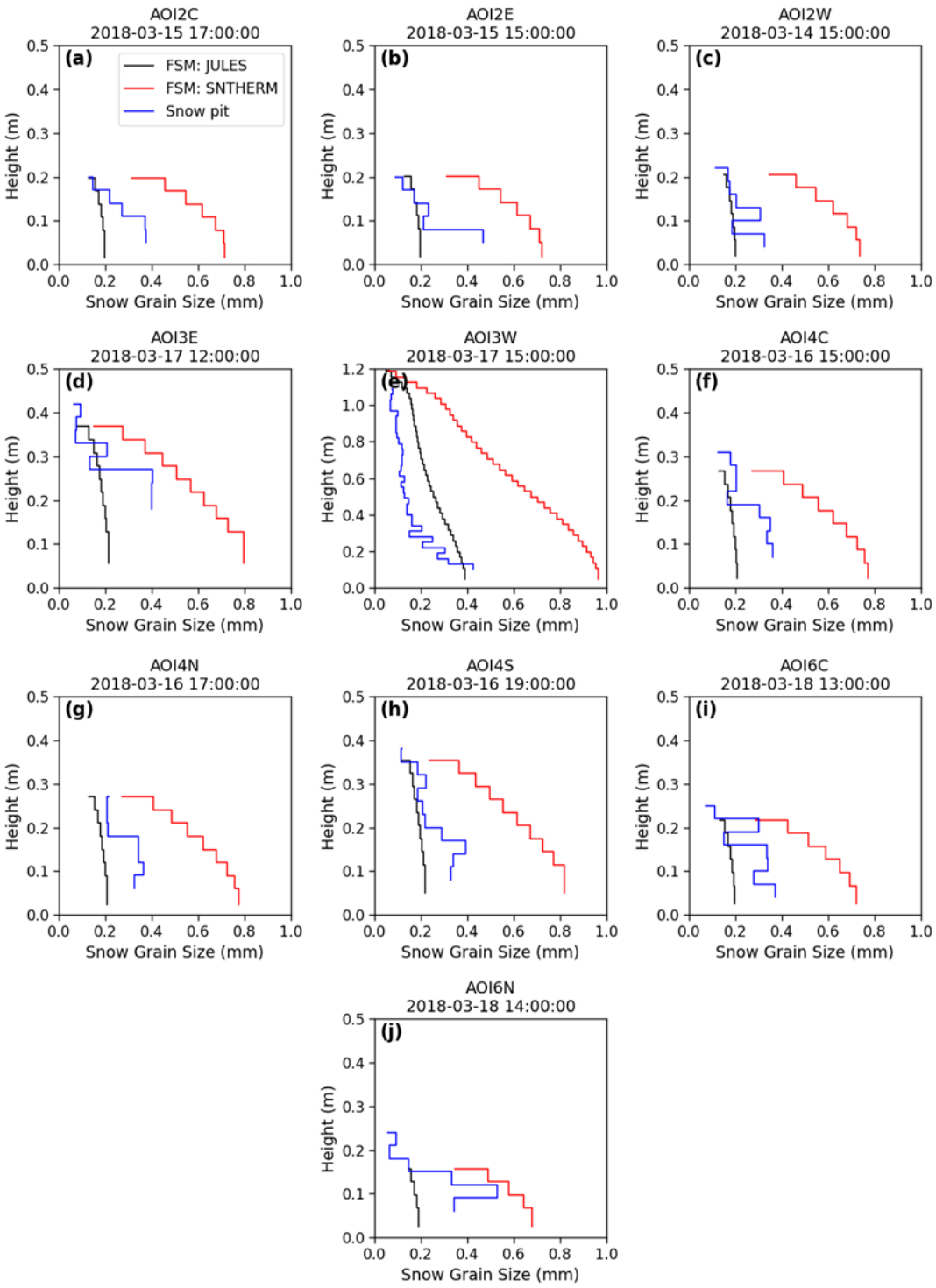

Figure 3.6 Vertical profiles of snow grain size comparing in-situ observations (blue line) with two FSM parametrisations: the JULES snow grain model (black line) and SNTHERM snow grain model (red line). Each panel (a-j) corresponds to a different Area of Interest (AOI) in TVC, with time and date indicating when the snow pit measurements were taken.

JULES models grain growth using simple empirical methods based on destructive metamorphism and underestimation of vapour transport, this leads

to slower grain growth and results in JULES underestimating grain size. SNTHERM models grain growth is driven by vapour fluxes which is influenced by temperature gradients.

This leads to constructive metamorphism and excessive sublimation and deposition, resulting in large grain sizes compared to the measurements.

The difference between the models is expected due to the purpose of the models. JULES is a large-scale land surface model and grain size is used to simulate surface albedo; therefore, grain size is not so important at the base of the snowpack (Sandells et al., 2017).

Conversely, SNTHERM was developed to accurately represent grain size and simulate water flow as well as albedo (Jordan, 1991). Despite this, JULES performs better than SNTHERM, but the best size grain growth model probably lies between the two, with a combination of SNTHERM vapour transport physics and JULES conservative approach suggesting snow grain growth model development is still required.

3.4.1.2 Snow Density

Figure 3.7a-j compares observed snow density profiles with simulated snow density from two density models; the rigid layer model and the deforming layer with wind packing which are described in section 3.3.1.

The modelled density profiles with the rigid layers option (black lines) are similar across the region, but the observed snow density profiles are much more variable. In general, for all sites, the observed density follows typical Arctic tundra snowpack properties with low densities (around 100 kg m^{-3}) at the top of a snowpack, indicative of fresh snow, and increases in the middle of the snowpack to about 400 kg m^{-3}, indicative of wind slab (Berteaux et al., 2017). Although the modelled snow density is low at the top of the snowpack, around 200 kg m^{-3}, this is higher than the observed snow density. The increase to 300 kg m^{-3} in the middle of the snowpack is slight in comparison to the observed snow density.

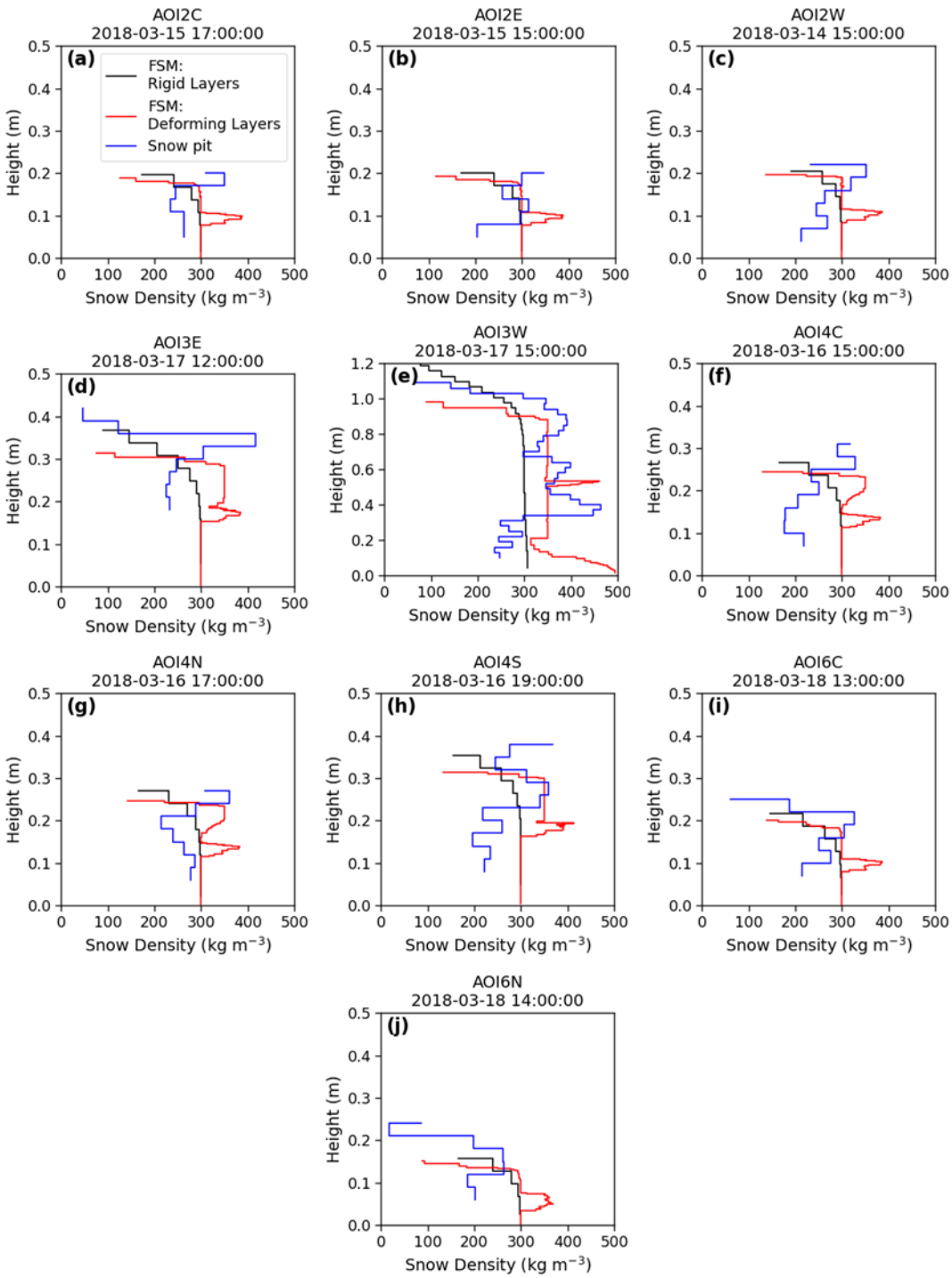

Figure 3.7 Vertical profiles of snow density comparing in-situ observations (blue line) with two FSM parameterizations: the rigid layers model (black line) and the deforming layers model (red line). Each panel (a–j) corresponds to a different Area of Interest (AOI) in TVC, with the date and time indicating when the snow pit measurements were taken.

The observed snow density then decreases towards 200 kg m^{-3} at the base of the snowpack due to metamorphic processes that produce depth hoar. In contrast, the modelled snowpack is too dense at the base (300 kg m^{-3}). Depth

hoar is a common feature of Arctic snowpacks due to high vertical temperature gradients which causes upward water vapour transfer. FSM, like similar models (i.e., SNOWPACK and Crocus) do not simulate this process (Domine et al., 2019; Royer et al., 2021).

The deforming layer profiles with the wind packing option (red lines) show a clear increase in snow density around the middle of the snowpack, indicating a wind slab in the snowpack. This is like observed snow density profiles, which have density values of approximately 350 kg m^{-3}. However, FSM tends to overestimate the density of the wind slab layer (approximately 400 kg m^{-3}) and underestimates the height of the wind slab layer at every site, except AOI3E.

Wind slab formation in Arctic snowpacks is often highly localized due to terrain factors such as topography and vegetation (Essery & Pomeroy, 2004). This suggests wind compaction parameterizations are too simplified and unable to simulate micro-scale processes (Liston et al., 2007; Vionnet et al., 2012).

3.4.1.3 Snow Temperature

Figure 3.8a-j compares observed snow temperature profiles with simulated snow temperature. FSM simulated profiles used the rigid layer model and the deforming layer with wind packing options to assess temperature gradient effects.

The observed snow temperatures (blue lines) are more variable than both models, but the models can capture the temperature gradients. As expected, the majority of sites have negative temperature gradients (warmer at the base, cooler at the top) due to the insulating properties of snow (Berteaux et al., 2017). All sites at AOI2 contradict this and exhibit positive temperature gradients, suggesting local influences from synoptic weather conditions or variable terrain.

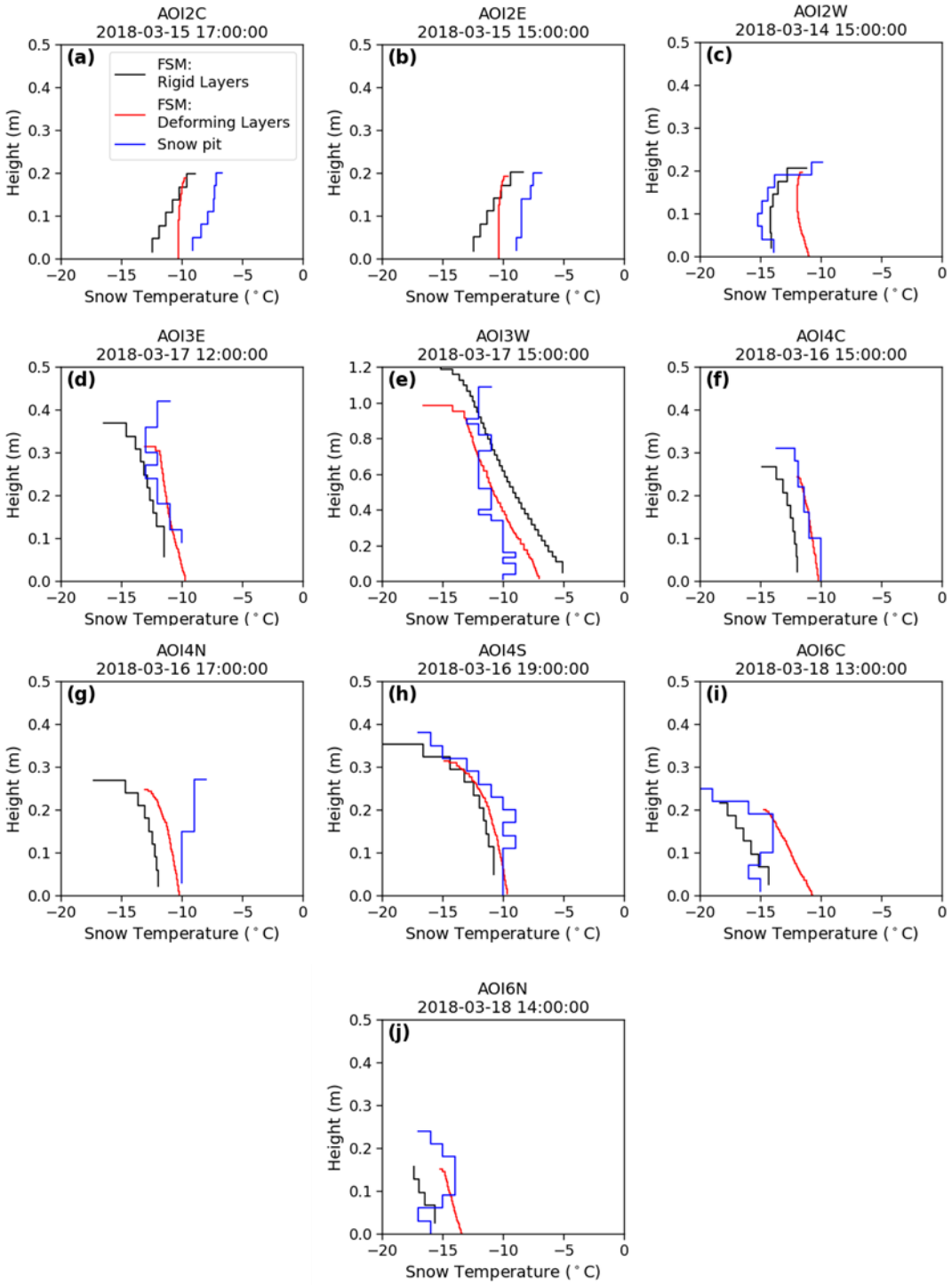

Figure 3.8 Vertical profiles of snow temperature comparing in-situ observations (blue line) with two FSM parameterizations: the rigid layers model (black line) and the deforming layers model (red line). Each panel (a–j) corresponds to a different Area of Interest (AOI) in TVC, with the date and time indicating when the snow pit measurements were taken.

The observed profiles indicate that the deforming layer model (red line) more accurately captures the sharper temperature gradients and warmer

temperatures at the depth compared to the rigid layer model (black line). This can be attributed to the wind packing option in the deforming layer model, which increases density and impacts thermal conductivity, resulting in warmer temperatures at the base (Domine et al., 2019; Vionnet et al., 2012). To support this, the deforming layer model often overestimates the basal temperature compared to the observed temperatures, suggesting the overly dense wind slab layer is causing the warmer base.

3.5 Regional Snow Modelling

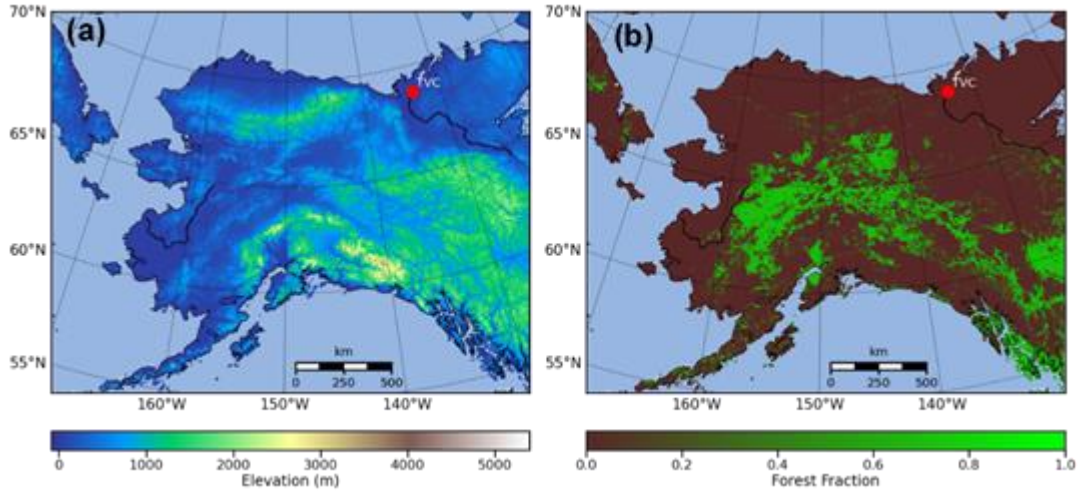

Figure 3.9 Maps showing the domain of FSM simulations, at multiple points across Northwest Canada and Alaska. a) Elevation map. b) Forest fraction map. A red circle marks TVC.

The results presented so far have involved running FSM at a single point. This section presents results where FSM has been run with an NWP dataset (Met Office, 2016) that spans northwest Canada and Alaska. NWP was run by the Met Office UM for the MACSSIMIZE campaign between 2 October 2017 and 1 April 2018 at 1.5 km resolution and hourly time steps for the first 48 hours at surface level. The second 24-hour forecast runs at 0000 hrs were used where available. FSM was run with the JULES grain growth model and rigid layers model. FSM has been run with a maximum of 3 layers, which reflects a typical Arctic tundra snowpack and follows previous studies (e.g. Sandells et al., 2024). The extent of the forecast runs is shown in the elevation and forest cover maps in Figure 3.9. TVC is shown by a red circle. Elevation and forest fraction data were retrieved from ancillary data from NWP model runs. The

elevation map shows that the mountains are situated in the south and southeast, as well as some in the Northwest. The forests are in the centre between the higher elevations and do not encroach into the north.

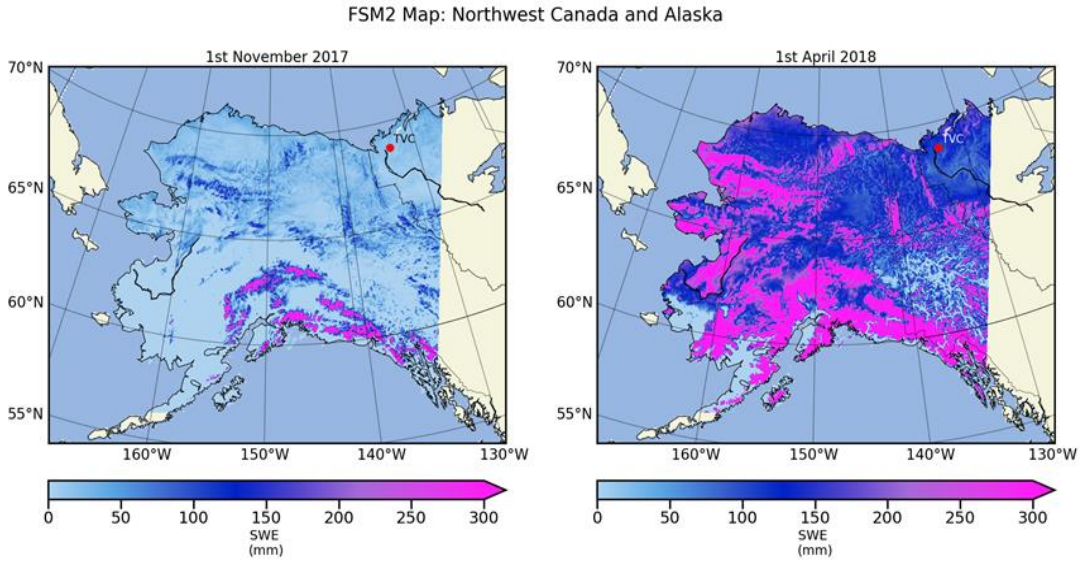

Figure 3.10 Snow Water Equivalent (SWE) simulations from FSM across Northwest Canada and Alaska for the beginning of the snow season (left; 1st November 2017) and end of the snow season (right; 1st April 2018).

Figures 3.10 and 3.11 show simulated SWE and snow depth maps, comparing the beginning of the snow season on 1 November 2017 to its conclusion on 1 April 2018. The snow builds up over the mountains in the south and northwest, where snow depth exceeds 2 m and SWE exceeds 300 mm, even at the start of the winter in November 2017. By April 2018 SWE and snow depth exceed 300 mm and 2 m respectively in the mountainous region in the Northwest. For the rest of the region, SWE and snow depth are around 150 mm and 1 m respectively, except around the coastal region in the southwest. At TVC on 1st April, SWE is approximately 100 mm and snow depth is less than 0.5 m. This agrees with the SWE and snow depth simulated by FSM driven by weather station data.

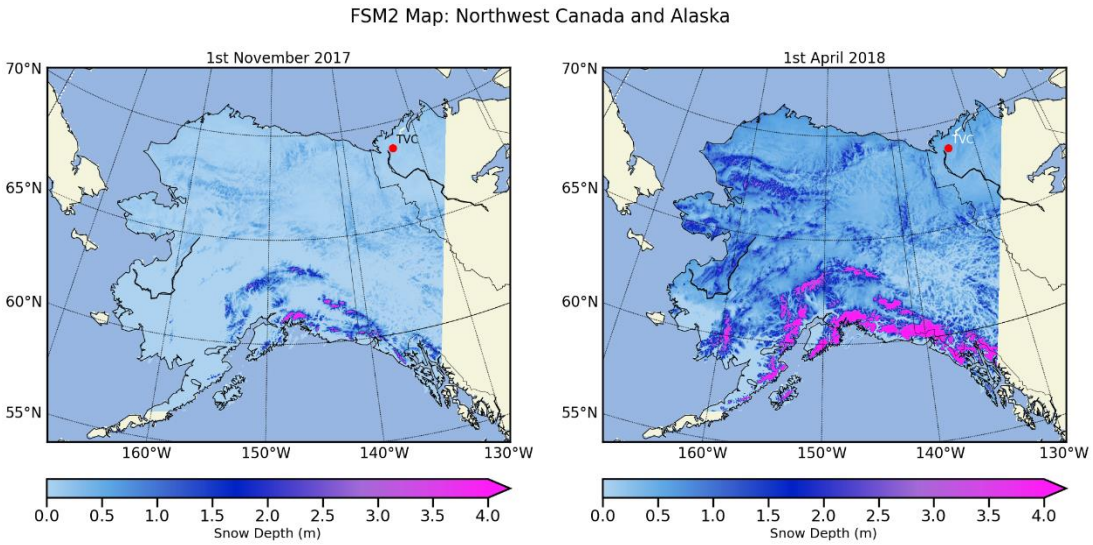

Figure 3.11 Snow Depth simulations from FSM across Northwest Canada and Alaska for the beginning of the snow season (left; 1st November 2017) and end of the snow season (right; 1st April 2018).

3.5.1 FSM SWE Simulations

3.5.1.1 GlobSnow

The map in figure 3.12 shows the distribution of the GlobSnow 3.0 SWE dataset across the studied region on 1 April 2018. GlobSnow uses passive microwave satellite data to estimate SWE and further details on the dataset are provided in section 3.2.3. Compared to FSM simulations, the GlobSnow dataset has much lower SWE across the region. There are patches of missing data across the region which corresponds to mountainous regions. This is a known issue with the dataset as the method cannot estimate SWE at higher elevations (approximately > 200m; Luojus et al., 2021).

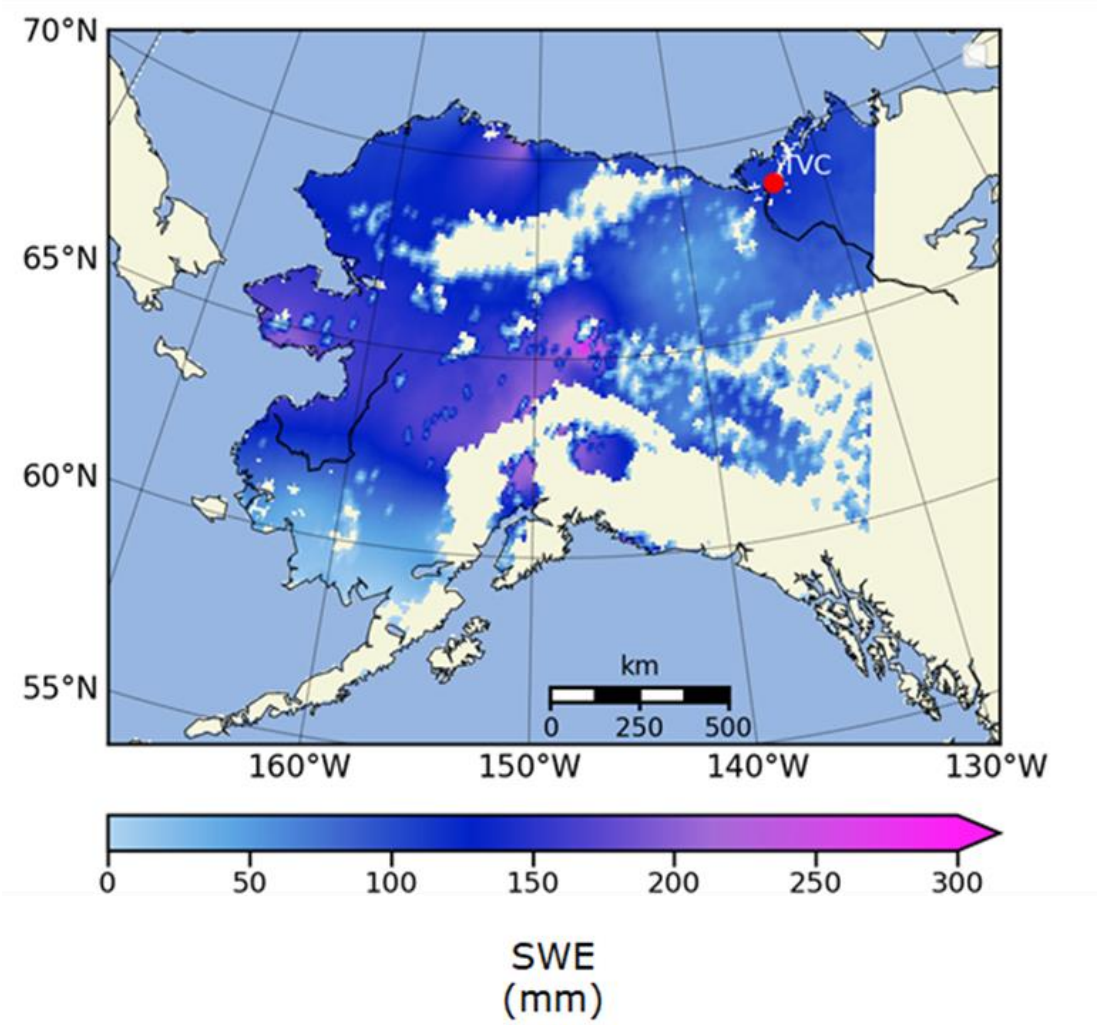

Figure 3.12 Map showing the snow water equivalent (mm) product from the GlobSnow dataset on 1 April 2018.

The scatter density plot in figure 3.13 shows that FSM overestimates SWE (MBE = 42.46 mm) compared to GlobSnow. There is almost no linear relationship between FSM SWE and GlobSnow SWE with a correlation of 0.07. The RMSE is 111.34 mm and MAE is 83.69 mm. GlobSnow has been validated against in-situ observations, showing good agreement with observed SWE (Luojus et al., 2021). However, there may be other factors relating to GlobSnow that are contributing to FSMs inferior performance.

Firstly, the analysis is for a single day on 1st April 2018 and Luojus et al. (2021) stated that GlobSnow exhibited the largest RMSE in April and May. This is due to the transition from the snow season to the melt season which limits GlobSnow ability to estimate SWE because the microwave signal is absorbed

rather than scattered (Luojus et al., 2021). In addition, Luojus et al. (2021) found that GlobSnow SWE was more difficult to predict in Canada compared to other regions, suggesting that estimating SWE in this region can be hard due to its deeper snowpacks and higher elevations.

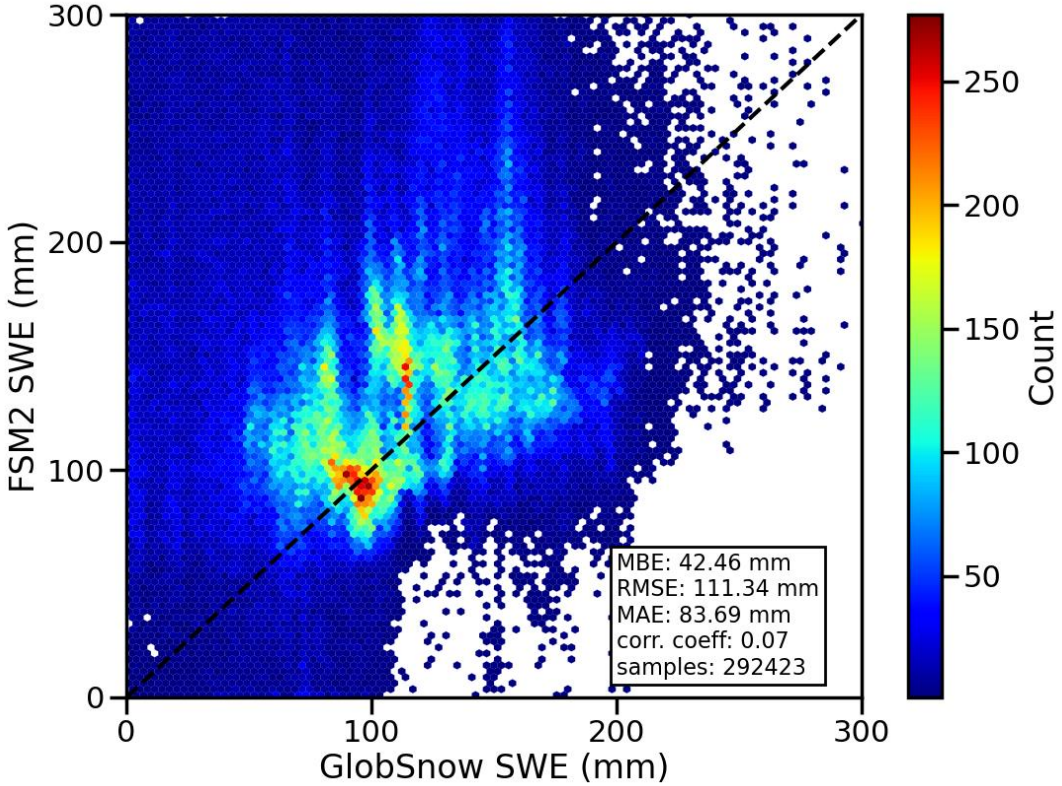

Figure 3.13 Scatter density plot comparing FSM simulated SWE data with GlobSnow data on 1st April 2018. With statistical metrics, mean bias error, root mean square error, mean absolute error, correlation coefficient, and number of samples.

Lastly, table 3.1 shows for shallower snowpacks (< 150 mm) FSM-GlobSnow comparisons have an RMSE of 68.16 mm and an improved correlation of 0.23. This improved accuracy demonstrates the inaccuracies of satellite-based SWE retrievals when estimating deep snow conditions, which has been previously noted (Mortimer et al., 2020; Takala et al., 2011). This suggests that FSM SWE needs further validation over spatial scales.

Table 3.1 MBE, RMSE, MAE, correlation coefficient and the number of samples for FSM modelled SWE below 150 mm against GlobSnow SWE data.

MBE (mm)	RMSE (mm)	MAE (mm)	CORRELATION (r)	NUMBER OF SAMPLES
18.40	68.16	51.23	0.23	141456

3.5.1.2 CanSWE

To further validate FSM SWE, it has been compared with the CanSWE dataset, a collection of in-situ measurements of snow products across Canada (see section 3.2.3). Figure 3.14a shows the spatial distribution of CanSWE points that are available for comparison with FSM SWE. There are very few points in the north of Canada near TVC, highlighting the in-situ datasets bias toward the less remote regions.

The scatter graph in figure 3.14b shows that FSM performs well when compared with observations. FSM underestimates SWE with an MBE of -33.92 mm. A RMSE of 56.69 mm indicates little variability in the data and a r-value of 0.62 suggest moderate linear relationship. These statistics are comparable to the GlobSnow SWE dataset for the same region, which was compared to in-situ data. Similarly, the GlobSnow dataset underestimated SWE, but the RMSE was higher (84.56 mm), and correlation was lower (0.47) (Luojus et al., 2021). Although, FSM SWE was compared to eighty-seven data points whereas, GlobSnow SWE was compared to 67646, making it a more robust test. Nevertheless, this shows FSM can simulate SWE on a spatial scale.

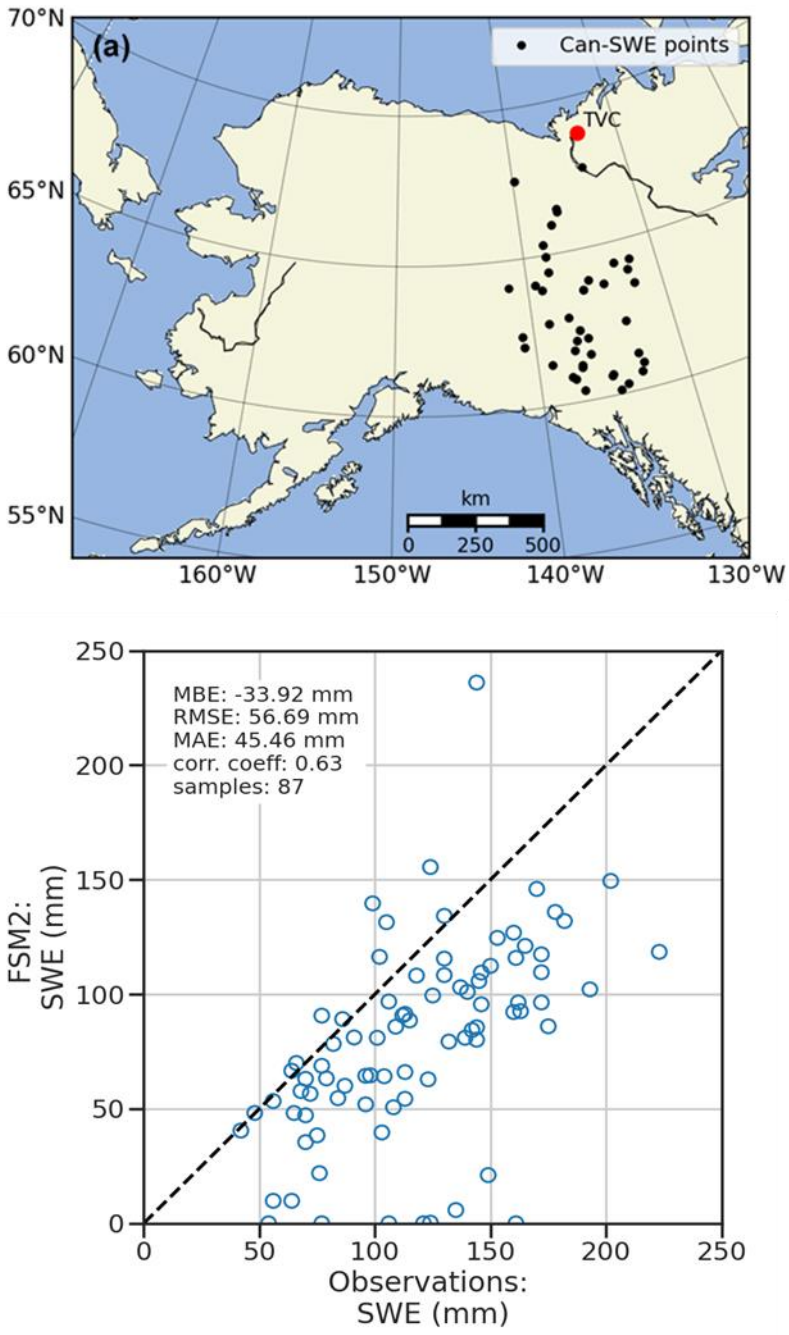

Figure 3.14 (a) a map showing the distribution of the CanSWE data points. (b) FSM simulated snow water equivalent compared with observed snow water equivalent (mm) products. Observations from the Canadian historical dataset were collected between 31 January and 1 April.

3.6 Chapter Summary

This chapter has explored Arctic tundra snowpacks and how well snow models can simulate their distinct characteristics. The process that governs the formation of typical Arctic tundra snowpacks was described. The difficulty in measuring and modelling snow products and properties, due to its spatial heterogeneity, was discussed.

The snow model, FSM, was described; this included the different parameterizations including two snow growth models (JULES and SNTHERM) and a wind packing option. FSM simulations of snow layer properties were compared with in-situ measurements from ten snow pits collected in a previous field campaign.

Overall, FSM failed to capture most of the characteristics of a typical Arctic tundra snowpack. While the inclusion of wind packing helped simulate denser slab layers observed in the snow pit data, FSM was unable to reproduce the low-density basal depth hoar layer due to missing vapour flux processes. Between the two grain growth models tested, the JULES model outperformed SNTHERM by simulating more realistic grain sizes across all sites. SNTHERM consistently overestimated grain size, which has significant implications for microwave emissivity modelling in subsequent chapters.

These results answer research question 1 and objectives ii and iii (section 1.2.1.1) by demonstrating that while FSM can approximate certain snowpack features, it still requires further physical refinement – particularly for Arctic tundra sites where microstructural detail is critical.

FSM was also used to simulate snow depth and SWE at multiple points across the region, providing a basis for scaling up to gridded emissivity modelling in chapter 4 and contributing directly to research question 3 (section 1.2.3).

FSM-simulated SWE was compared with an extensive SWE dataset retrieved from passive microwave satellites, GlobSnow. FSM performed poorly with high errors (RMSE = 111.34 mm) and low correlations (r-value = 0.07). However,

after further analysis, it was concluded that FSM performance may be due to limitations in GlobSnow's retrieval algorithm, particularly over shallow snowpacks. Conversely, comparison with the in-situ CanSWE dataset showed significantly lower errors (RSME 56.69 mm, r = 0.63) suggesting FSM is better suited for regions with lower SWE and may be reliable at finer spatial scales. This partially fulfils research question 3, objectives i (Section 1.2.3.1), ii and iii by establishing FSM's potential and limitations when scaled regionally.

Crucially, the findings in this chapter reveal that errors in FSM's snow microstructure outputs – especially grain size – may propagate into brightness temperature simulations. This affects the reliability of emissivity predictions in chapter 4 and has implications for operational assimilation of radiance data in NWP models. As such, improvements to FSM such as adding vapour transport and wind redistribution are not just academic but operationally significant.

Beyond this thesis, the results highlight a broader challenge in snow modelling: many existing snow models and their parameterisations were originally developed for alpine or avalanche forecasting contexts where snowpacks are typically deeper, wetter and more variable than those found in the Arctic tundra regions. This chapter demonstrates that these assumptions often break down in the Arctic where snow is shallower, colder, and more homogenous in vertical structure but highly affected by wind redistribution. The work highlights the need for snow models that are explicitly calibrated and physically appropriate for Arctic tundra environment – not only to support radiance assimilation but also for wider application in cryospheric monitoring, hydrology, permafrost modelling, and climate change assessments.

Chapter 4 Snow radiative transfer modelling

4.1 Introduction

To address research questions 2 and 3 (sections 1.2.2 and 1.2.3), this chapter focuses on snow radiative transfer modelling, with a particular emphasis on the SMRT model (Picard et al., 2018).

The chapter begins with an overview of microwave theory. This is followed by a discussion on microwave emissions and how they interact with snow and the atmosphere. The SMRT model will be described including its structure, key components, and configurations used in this study. Sensitivity analysis is performed to assess the influence of different snow parameters on T_B, followed by point-scale and regional-scale SMRT simulations that validate the model against observations. Finally, the effectiveness of SMRT in simulating T_Bs for various snow conditions will be demonstrated, highlighting its potential for improving snow data assimilation in weather and climate models.

4.2 Microwave Theory

Electromagnetic (EM) radiation is emitted by all matter. A blackbody is defined as an object that absorbs all incident radiation and emits it as thermal energy (Ulaby et al., 1981). The spectral brightness of a blackbody depends on frequency (ν) and physical temperature (T) as stated by Planck's Law (Ulaby et al., 1981)

$$B_\nu = \frac{2h\nu^3}{c^2}\left(\frac{1}{e^{\frac{h\nu}{kT}}-1}\right), \tag{4.1}$$

where $c = 3\times10^8$ m s^{-1} is the speed of light in a vacuum, $h = 6.634\text{x}10^{-34}$ J is Planck's constant and $k = 1.38\text{x}10^{-23}$ J K^{-1} is Boltzmann's constant. In the microwave range, this can be simplified using the Rayleigh-Jeans approximation for $h\nu \ll kT$, which gives (Ulaby et al., 1981)

$$B_\nu = \frac{2kT}{\lambda^2}, \tag{4.2}$$

where $\lambda = c/\upsilon$ is wavelength. Equations 4.1 and 4.2 hold for blackbodies, but natural materials, or grey bodies, are not perfect emitters and radiators. The brightness of a grey body is a function of direction. Equation 4.2 can be used to derive the T_B of a grey body (Ulaby et al., 1981)

$$T_B = \frac{\lambda^2}{2k} B_\upsilon. \tag{4.3}$$

The T_B is the physical temperature of an equivalent blackbody that emits the same amount of energy. T_B can also be defined by the emissivity (i.e., effectiveness in emitting energy as thermal radiation) of a material (Ulaby et al., 1981). T_B is dependent on frequency, wave polarisation and EM properties, namely permittivity (Kontu, 2018). Permittivity is the measure of the electrical storage ability of a material when exposed to an electric field. The permittivity of free space or a vacuum (8.85418782 x 10^{-12} F m^{-1}) is often used to express the permittivity of other materials. This is called relative permittivity (ε_r), which is complex and expressed as

$$\varepsilon_r = \varepsilon' - i\varepsilon'' \tag{4.4}$$

where the real part ε' describes the material's resistance to electrical fields and the complex part ε'' is related to the material's dielectric losses (Mätzler, 2008).

Wave polarisation describes the orientation of the oscillation of the electric field. Radiation is unpolarised if it is emitted with random polarizations. This is true for radiation from the sun, but when the sun's radiation is scattered in the atmosphere or reflects off a surface (i.e., snow) it becomes polarised. For this reason, most microwave emissions are polarised and radiometers must measure both horizontal and vertical radiation components (Mätzler, 2008).

Emission and extinction are two processes that define how radiation interacts with a material (e.g., a snowpack) and will affect measured T_B. Emission is the addition of energy from a material and extinction results in loss of energy in a material. Losses can occur due to absorption, the conversion of energy to

another form (i.e., heat or scattering), where energy is redirected from the original direction of propagation (Ulaby et al., 1981).

4.3 Microwave Emissions and Snow

Dielectric properties of snow have been shown to affect the amount of absorption or scattering (Mätzler, 1998). A snowpack essentially contains air and water in different states, but the electric dipole structure of water (H_2O) is the important part in this case. Although H_2O is electrically neutral, the positive and negative charges are asymmetrical. When an electrical field is applied, molecular reorientation occurs; this is called dielectric polarisation (different from wave polarisation; Baker-Jarvis, 2000). Therefore, H_2O in multiple phases can be described as a dielectric (King, 2014).

A snowpack generally consists of air, ice, and liquid water with hugely different dielectric losses in varying quantities. The composition of a snowpack will, therefore, determine its relative permittivity and how EM waves interact with it. At microwave frequencies, air is considered to have the same permittivity as free space and therefore is not a significant source of absorption or scattering (King, 2014). The relative permittivity of freshwater ice and liquid water are both largely dependent on frequency and temperature, but water has a higher dielectric constant. Therefore, the presence of water in a snowpack will significantly change its relative permittivity (Kontu, 2018). Figure 4.1 shows the interaction between a snowpack and microwave radiation. In a snowpack, natural microwave radiation is emitted from the surface of the snow, within the snow, and from the substrate beneath the snow (e.g., soil, sea ice, lake ice, etc.). Therefore, emission, absorption, and scattering need to be taken into account when measuring T_B over snow surfaces (Matzler et al., 2000). As the amount of snow (SWE) in a snowpack increases, T_B will generally decrease because scattering becomes more dominant (Mätzler, 1987). However, there is a threshold at which emission from snow masks out the scattered radiation. At 36.5 GHz, this threshold has been reported at ≈150 mm SWE (Derksen & Brown, 2012; Santi et al., 2017). This depends on frequency, as lower frequencies will penetrate deeper into the snowpack, and thus the limit will be

higher. Radiation is scattered by snow grains and the extent of scattering depends on their size and geometry (Kontu, 2018). Generally, at lower frequencies (below 20 GHz) absorption is more dominant than scattering (Ulaby et al., 1986). Comparisons between 18.7 and 36.5 GHz are often made as these represent the absorption and scattering regions (Kontu, 2018). Snow properties such as grain size and density also affect the absorption and scattering in a snowpack (Santi et al., 2017).

4.4 Microwave Emissions and the Atmosphere

Kirchhoff's Law states that at any frequency in the microwave region where the atmosphere absorbs radiation, it will also emit thermal radiation. Thus, any radiance leaving the top of the atmosphere will change with the distribution of emitting gases and the distribution of temperature throughout the atmosphere. Therefore, radiance can be measured to obtain atmospheric profiles of temperature and gases (Houghton et al., 1986). The radiative transfer equation "describes the flow of radiant energy to be measured by a radiometer" (Janssen, 1994). Broadly the radiative transfer equation states that the change in intensity of the beam over space is equal to the product of the amount of radiation scattered into the beam from all directions and the emission from the material, minus losses (from absorption and scattering). At microwave frequencies within the oxygen absorption band (50-60 GHz), atmospheric temperature profiles can be obtained (Weng et al., 2003). Additionally, the atmospheric temperature can be measured at frequencies where the atmosphere is transmissive, although more sensitive to surface emissivities. At frequencies near the water vapour absorption line (≈ 183 GHz) atmospheric humidity profiles can also be obtained.

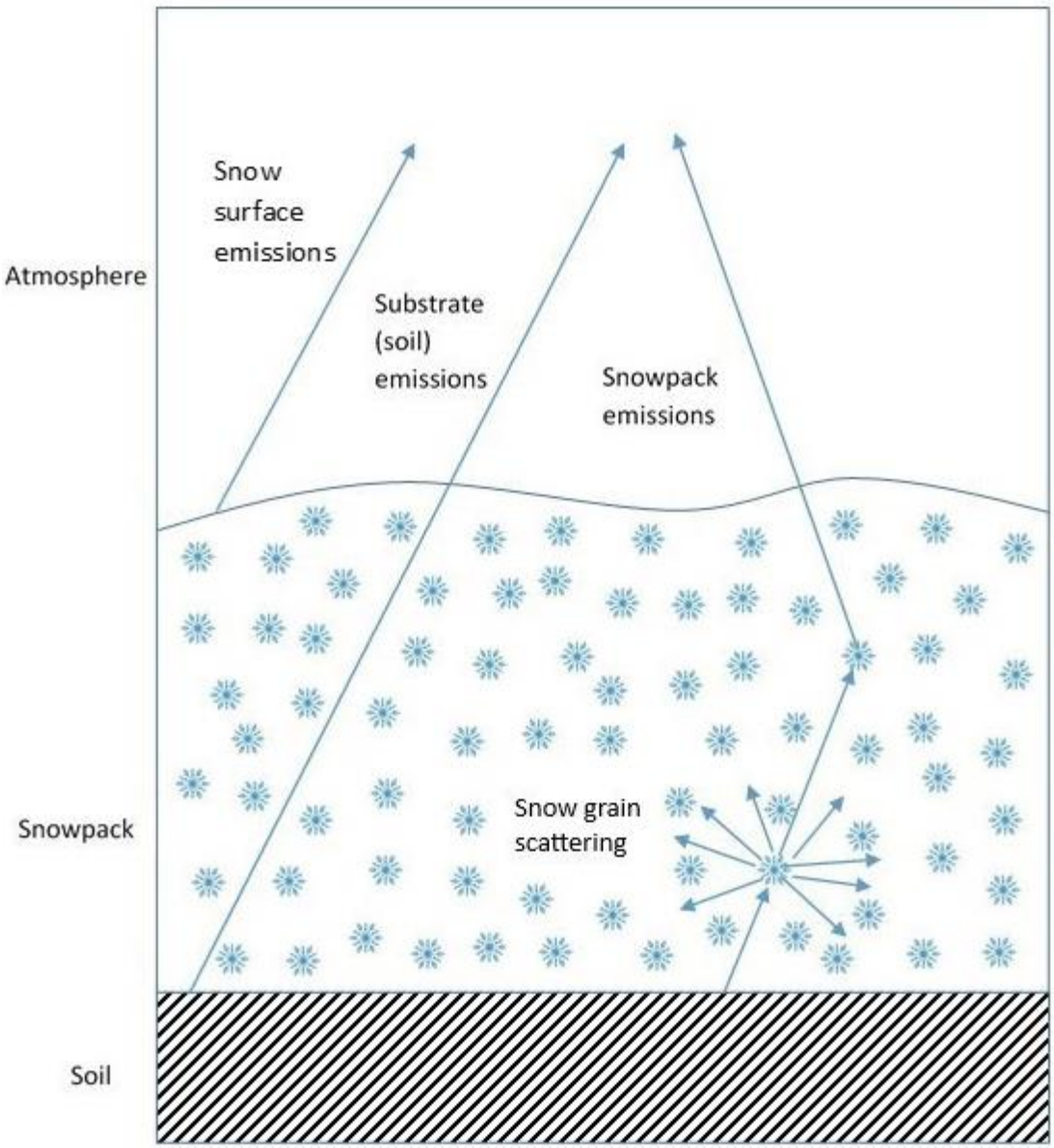

Figure 4.1 Diagram illustrating how microwave radiation interacts with a snowpack. Microwave radiation is emitted from the surface of the snowpack, from within the snowpack and from the beneath the snowpack. Scattering occurs from inhomogeneities in a medium, in this case snow grains. Reproduced from (Liu et al., 2006).

4.5 The Snow Microwave Radiative Transfer Model

The SMRT model is a thermal emission and backscatter model designed to simulate microwave interactions with snow, sea ice, and frozen lakes. By integrating various representations of snow microstructure, SMRT enables improved characterization of snow properties, making it particularly valuable for remote sensing applications and the assimilation of microwave observations into NWP models. This thesis focuses on passive microwave

remote sensing; therefore, all subsequent SMRT simulations will be conducted for passive sensors.

One of the key strengths of SMRT is its modular structure, which allows users to select from different electromagnetic theories for computing scattering. These include Dense Media Radiative Transfer (DMRT), the Improved Born Approximation (IBA), and independent Rayleigh scatterers, each offering varying levels of complexity and applicability to different snow conditions. Similarly, SMRT incorporates multiple microstructure formulations, such as exponential, sticky hard spheres, and independent spheres, to represent snow grain properties. SMRT uses autocorrelation functions (ACF) to characterize the spatial arrangement of snow grains and how they impact scattering and absorption.

For radiative transfer calculations, SMRT primarily employs the discrete ordinate and eigenvalue (DORT) method. However, it also supports alternative models, including MEMLS, HUT, and DMRT-QMS, allowing for flexibility in simulating microwave emissions. The model can represent multi-layered snowpacks, with required input parameters including snow thickness, density, grain size, temperature, and liquid water content. These snowpack properties can be derived from FSM simulations.

SMRT produces T_B outputs across a range of frequencies and incidence angles, as specified by the user. At higher frequencies, atmospheric constituents such as water vapour and oxygen absorb and emit microwave radiation, which can reduce the accuracy of T_B simulations. To address this, SMRT includes an optional built-in atmospheric component or can be coupled with the Atmospheric Radiative Transfer Simulator (ARTS) for a more precise representation of atmospheric effects.

The underlying substrate beneath the snowpack also plays a crucial role in microwave interactions. SMRT offers several substrate options, including a generic reflector, a flat surface, and the Wegmüller soil model (Wegmuller & Matzler, 1999), each influencing microwave emission differently. By

incorporating these features, SMRT provides a versatile and comprehensive framework for simulating microwave interactions with snow, supporting advancements in both remote sensing applications and NWP.

4.5.1 The Radiative Transfer Equation

At the core of SMRT is the radiative transfer equation and SMRT uses the DORT method, which is widely used for multi-layered media (Picard et al., 2018). The general form of the radiative transfer equation in a plane-parallel medium is:

$$\mu \frac{\partial \boldsymbol{I}(\mu,\phi,z)}{\partial z} = -\kappa_e\,(\mu,\phi,z)\,\boldsymbol{I}\,(\mu,\phi,z) + \frac{1}{4\pi}\iint \boldsymbol{P}(\mu,\phi;\mu',\phi',z) I(\mu',\phi',z)\,d\Omega' + \kappa_a(\mu,\phi,z)\alpha T(z)\mathbf{1} \tag{4.5}$$

where the reduced specific intensity **I** = (I$_V$, I$_H$, U, V) and is defined as **I** = **I′**/n². Here, **I′** denotes the specific intensity and *n* is the refractive index at a given location (Mobley, 1994). The phase function, $\boldsymbol{P}(\mu,\phi,\mu',\phi',z)$, is 4x4 matrix and describes the scattering properties of a medium. κ_a and κ_e are the absorption and extinction coefficients and extinction is given by $\kappa_e = \kappa_s + \kappa_a$, where κ_s is the scattering coefficient. The vector $\mathbf{1}$ = (1,1,1,1). The directional variables are expressed in terms of the cosine of the zenith angle $\boldsymbol{\mu}$ and the azimuthal angle ϕ, while the associated solid angle is Ω**.** The vertical coordinate z follows the Earth science convention, where $\boldsymbol{\mu} < \mathbf{0}$ corresponds to incident and downwelling radiation, while $\boldsymbol{\mu} > \mathbf{0}$ represents upwelling radiation. This formulation ensures the equation remains valid for both active and passive microwave remote sensing applications.

In passive mode, the $T_{\mathrm{B,\,p}}$ (where p is the polarisation and either horizontal *H* or vertical *V*) is proportional to the reduced specific intensity I_p according to the Rayleigh–Jeans approximation:

$$I_p = \alpha T_{B,p} \tag{4.6}$$

where $\alpha = 2v^2k/c_0^2$, with *k* being the Boltzman constant, c_0 the speed of light in a vacuum and *v* the wave frequency. However, in practical applications for passive mode, leveraging the linearity of the radiative transfer equation, I_p can be directly replaced by the T_B, and α is set to 1. This simplification is implemented within the SMRT model to streamline T_B computations.

4.5.2 Electromagnetic Model

The primary electromagnetic model used in SMRT to describe the interaction of microwaves with snow is the IBA. The IBA model is used to compute the scattering properties of snow by treating it as a two-phase medium, where ice inclusions are embedded in an air matrix. How incident microwaves are scattered within the snow medium is defined by the phase function

$$p(\theta,\phi)_{1-2\,frame} = f_2(1-f_2)(\epsilon_2-\epsilon_1)^2Y^2(\epsilon_1,\epsilon_2) \\ k_0^4M(|k_d|)\sin^2\mathcal{X} \tag{4.7}$$

where angles (θ,ϕ) define the scattering direction with the incident direction aligned along the polar axis. These angles influence how microwaves are redirected after interacting with snow grains, affecting the observed T_B.

The free-space wave number is given by $k_0 = 2\pi v/c$, where *v* is the wave frequency and c is the speed of light. Since the wave number appears as k_0^4 in the phase function equation, this emphasizes that scattering strength increases with frequency, meaning higher-frequency microwaves scatter more than lower-frequency ones.

The volume fraction of phase 2 (ice), denoted as f_2, is linked to the density ρ of the snow medium via $f_2 = \rho/\rho_2$, where ρ_2 is the density of pure ice. This parameter determines the concentration of scatterers in the medium, directly

influencing the scattering intensity. A higher volume fraction results in more scattering due to increased interactions between microwave radiation and snow grains.

The relative permittivities ϵ_1 and ϵ_2 correspond to the dielectric properties of air (background medium) and ice (scatterers), respectively. The contrast between these permittivities ($\epsilon_2 - \epsilon_1$) dictates the scattering efficiency—larger differences lead to stronger scattering effects. The equation accounts for temperature and frequency dependence of permittivity, though these dependencies are not explicitly shown.

The polarization angle $\mathcal{X}$ describes the relationship between the incident electric field and the scattering direction. This angle is given by

$$\sin^2\mathcal{X} = 1 - \sin^2\theta\cos^2\phi \tag{4.8}$$

(Ishimaru, 1997). This term appears in the phase function equation, where it modulates how different polarization states contribute to scattering.

4.5.1 Microstructure Model

The independent spheres microstructure model provides a simplified representation of snow grain scattering in microwave radiative transfer simulations. It assumes that individual snow grains act as isolated spherical scatterers, meaning that multiple scattering effects and near-field interactions between grains are neglected. The ACF for this model is expressed as:

$$\widetilde{C_{sph}}(k_d) = f_2(1 - f_2)v(a)P(k_d a) \tag{4.9}$$

where $\widetilde{C_{sph}}(k_d)$ represents the effective scattering cross-section of independent spheres as a function of wavenumber k_d. The parameter $v(a)$ describes the number density of scatterers with a radius a, which serves as the primary microstructure parameter for this model. The function $P(k_d a)$ is the scattering phase function, which determines the angular distribution of scattered radiation.

Since this model assumes no significant near-field interactions between grains, the scattering behaviour follows Mie theory when particle sizes are comparable to the microwave wavelength. In cases where the grain size is much smaller than the wavelength, scattering follows the Rayleigh regime, which is characterized by a strong dependence on particle size and frequency.

Despite its simplicity, the independent spheres model remains useful for first-order approximations of microwave interactions with snow, particularly when snow grains are well-separated and interactions between them are minimal. However, for denser or more complex microstructures, more advanced models such as the sticky hard spheres, approaches are often necessary to accurately capture multiple scattering effects (Picard et al., 2018). However, the parameter of sticky hard spheres, stickiness, cannot be easily measured in the field (Brucker et al., 2011; Picard et al., 2014; Roy et al., 2013) and is not currently simulated by FSM.

4.5.2 SMRT Simulations

The results presented in this work use the IBA electromagnetic model, the DORT radiative transfer solver and the independent sphere snow microstructure model to simulate T_B emitted from the surface of a snowpack. ARTS will be used to account for atmospheric absorption and scattering. The substrate model used is a simple flat surface, with a temperature of 258.15K as used in previous work in TVC (King et al., 2018; Sandells et al., 2024). When comparing to nadir observations an angle of 5° is used in the simulations because SMRT simulations at exactly nadir are not possible yet.

4.6 SMRT Point Simulations

4.6.1 Sensitivity Analysis

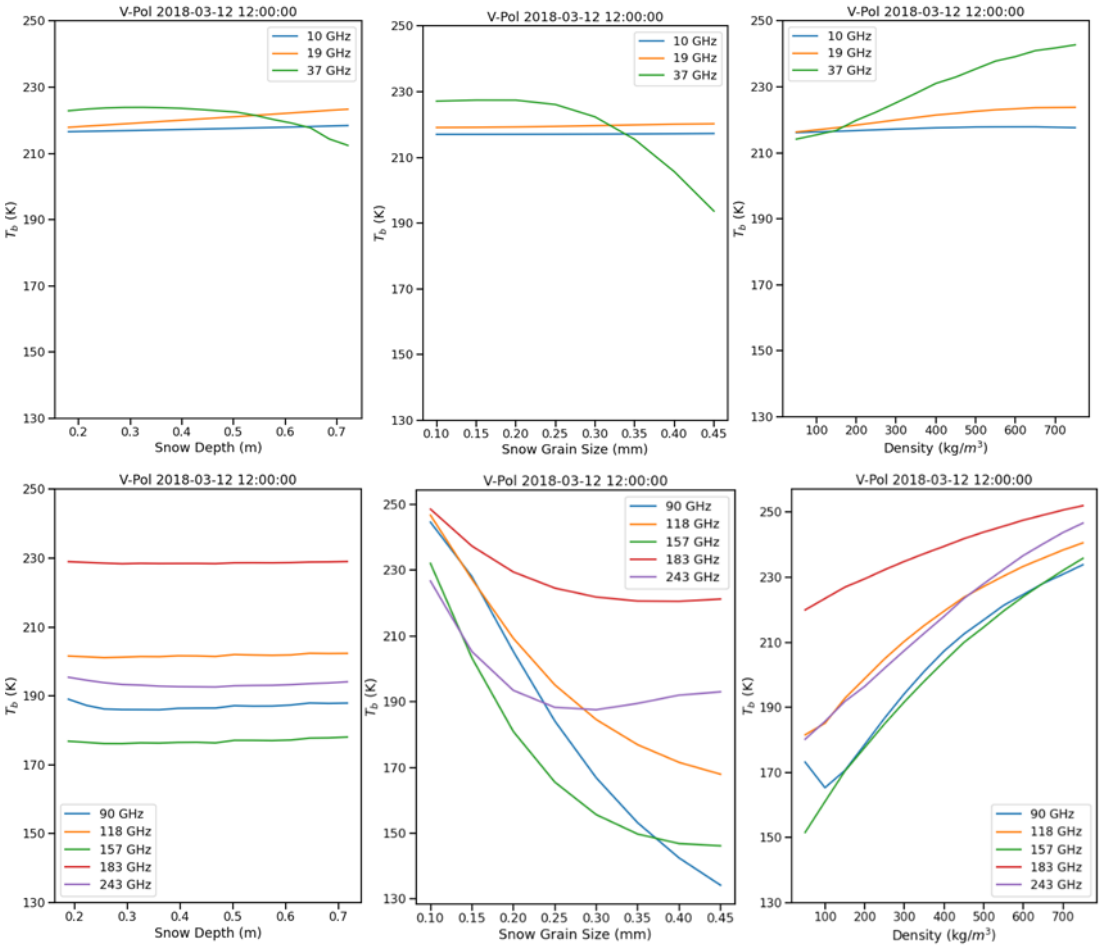

Figure 4.2 SMRT simulations of brightness temperature (T_B) with V-polarisation and near-nadir incidence on 12 March 2018 with variations in snow depth, snow grain size and density. SMRT has been run at 10, 19 and 37 GHz (upper panels), and 90, 118, 157, 183 and 243 GHz (lower panels). For frequencies 90 GHz and above, brightness temperature (T_B) is corrected for atmospheric effects.

Figure 4.2 tests the sensitivity of the SMRT model to certain input variables at different frequencies. T_B has been corrected with respect to the atmosphere. A day is picked during March and SMRT is run with FSM inputs, except for the variable being tested which was varied. For snow depth, the snowfall is scaled as an input to FSM. For all frequencies, T_B shows almost no change as snow depth increases, although at 37 GHz T_B decreases slightly as snow depth increases. This is due to the penetration depths at different frequencies. At lower frequencies (10 and 19 GHz) radiation can penetrate through the snowpack right to the substrate below, so here SMRT is simulating emission

from the soil which has been kept constant in this model run. Thus, at 10 and 19 GHz, T_B is not sensitive to changes in snow grain size and snow density because this is a measure of soil T_B, not snow T_B.

At 37 GHz, radiation can penetrate through the snow surface but not completely through to the substrate so there is more variability in T_B when snow microstructure is varied. At higher frequencies (90, 118, 157, 183 and 243 GHz) radiation cannot penetrate through the snowpack and therefore, SMRT is measuring the surface T_B. As snow grain size increases, T_B decreases consistently at 90, 118, 157 GHz. For the higher frequencies (183 and 243 GHz) T_B levels out when grain sizes go above around 0.25 mm. T_B increases as snow density increases; this is consistent for all frequencies, although T_B levels out as the density approaches 700 kg m^{-3}.

4.6.2 SMRT vs Ground-based Observations

Passive T_B measurements were obtained at TVC in March 2018 from a sled-mounted radiometer at 89 GHz using a surface-based microwave radiometer mounted on a sled at a height of approximately 1.5 m (Vargel et al., 2020).

Figure 4.3 compares SMRT-simulated T_B with ground-based observations at 89 GHz, with an incidence angle of 55° and at V-polarization. SMRT has been run with snow pit data (red circles) and three different FSM outputs; the JULES grain growth model (blue circles), the SNTHERM grain growth model (orange circles) and the deforming layers option with the wind slab and the SNTHERM grain growth options (green circles).

SMRT underestimates T_B when run using the JULES model at most sites. This is reflected by a mean error of -16.0 K and RMSE of 27.8 K. T_B is significantly underestimated when SMRT is run with the SNTHERM model. The mean error is -85.6 K and the RMSE error is 108.7 K. SMRT and JULES perform better when the SNTHERM model is coupled with deforming layers and the wind slab snow model; the mean error is -4.4 K. However, the RMSE is still high at 29 K. For the three SMRT simulation run with different FSM model configurations there is an outlier, where the observed T_B is around 240 K and SMRT has

simulated the T_B significantly lower. This occurs at AOI3W, which is a snow drift point where snow depth is significantly higher than the other pits (exceeds 1m). This shows that SMRT struggles to simulate T_B when snow is deep and heterogeneous. Overall, when SMRT is run using snow pit observations it can capture the observations. The mean error is 11.9 K and the RMSE is 22.7 K.

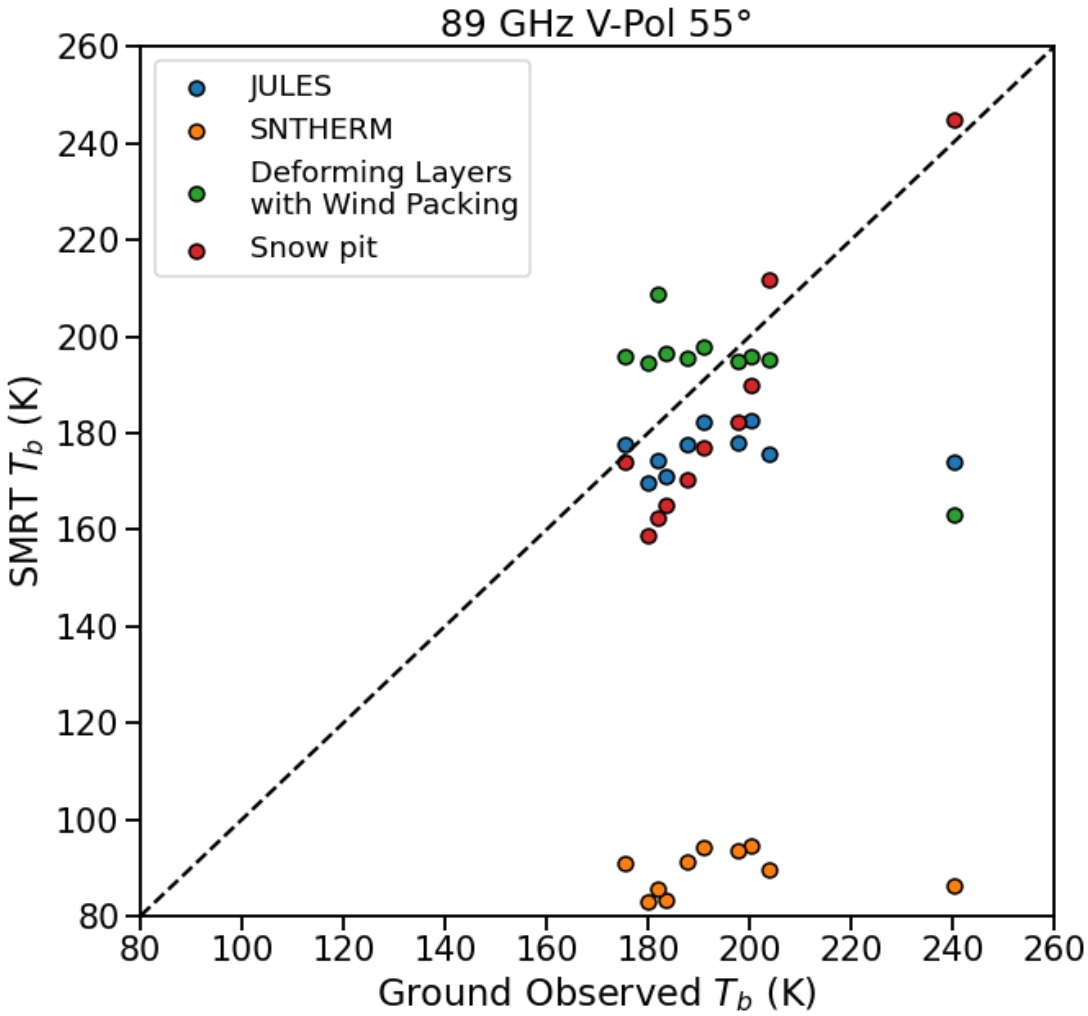

Figure 4.3 Comparisons between SMRT simulated brightness temperatures (T_B) and ground-based brightness temperatures (T_B) at 89 GHz, V-polarisation and 55° incidence angle. SMRT has been run with ground-based snow pit observations (red circles) and FSM run with the JULES snow grain configuration (blue circles), the SNTHERM snow grain configuration (orange circles) and the deforming layers and wind packing configuration (green circles). The ground-based data was collected at Trail Valley Creek in March 2018 using a sled-mounted surface–based radiometer.

These results show that T_B is sensitive to slight changes in snow microstructure particularly snow grain size and snow density. The SNTHERM grains were too large (see section 3.4.1.1), which resulted in SMRT underestimating T_B. The JULES grain growth model was a better

representation of measured grain size but underestimated grain growth. These results have been noted in previous studies (i.e. Sandells et al., 2017), indicating improved snow grain size modelling is needed.

4.7 Regional SMRT Modelling

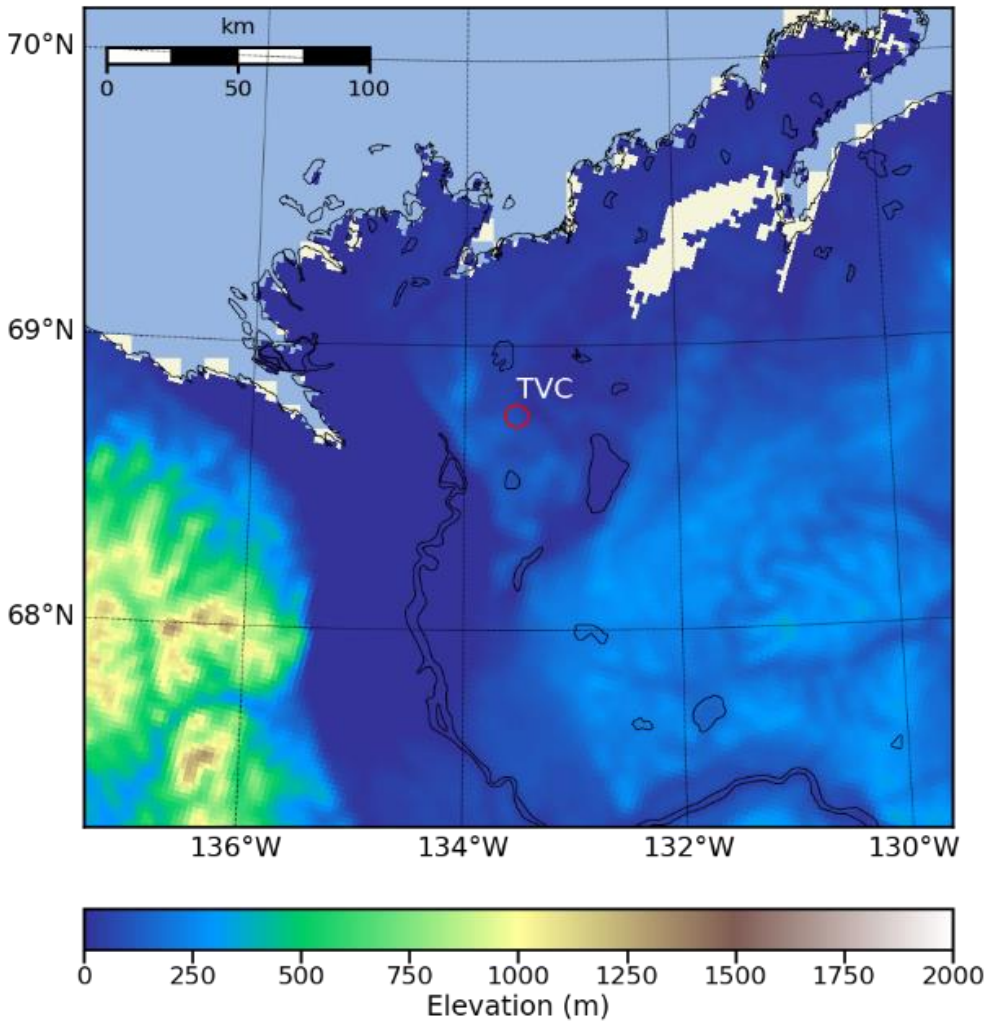

Figure 4.4 Elevation map showing SMRT domain across Northwest Canada. TVC is marked by a red circle.

SMRT was run with FSM snow layer outputs over a smaller region around TVC (see Figure 4.4). The elevation map shows high elevations greater than 1000 m in the southwest, which is part of the eastern end of the Brooks Range. For the rest of the region, elevations do not exceed 300 m. The valley where the Mackenzie River runs is among the flattest parts of the region.

Figure 4.5 shows maps of SMRT-simulated T_B at V-polarisation and 5° incidence angle on 1 April 2018 for frequencies ranging from 10.65 to 243 GHz. Overall, T_B increases as frequency increases except for the two atmospheric window channels: 157 and 243 GHz. The lowest T_Bs occur at the lowest frequencies (10.65 and 18.7 GHz) with a minimum value of 200 K and a maximum value of 220 K. The highest T_B occurs at 183 GHz, with values ranging from 237 to 250 K. Spatial variability tends to occur where topography is variable and T_B tends to increase on slopes and transitions between slopes and plateaus at the lower frequencies (≤ 37 GHz). This is contradictory at higher frequencies. Overall, T_B is more spatially variable at 37 and 89 GHz because at these frequencies T_B is sensitive to both the substrate and the snowpack. In contrast, at lower frequencies (≤ 18.7 GHz) T_B is sensitive to the ground and at higher frequencies (≥ 118 GHz) T_B is sensitive to the snow surface.

Scatter graphs in Figure 4.6a show the relationship between T_B and soil temperature at all frequencies. At the lower frequencies (≤ 37 GHz), Figure 6a shows that T_B is strongly influenced by soil temperature with a positive association and strong correlation ($r >$ 0.98). At all other frequencies, T_B decreases as soil temperature increases ($r <$ -0.6). At higher frequencies, (≥ 89 GHz) penetration depth decreases, and therefore the surface layer is expected to have more influence on T_B. Figure 4.6b compares T_B with surface snow temperatures at all frequencies. At lower frequencies (≤ 37 GHz), surface temperature has a negative influence on T_B, although this relationship is weak ($r <$ -0.36) suggesting less influence on T_B from the surface layer. At higher frequencies (≥ 118 GHz), T_B increases with surface temperature and this relationship is strong ($r >$ 0.9). At 89 GHz, T_B is less influenced by the surface because emissions can penetrate the snowpack and thus have a weaker relationship with surface temperature ($r \approx$ 0.7).

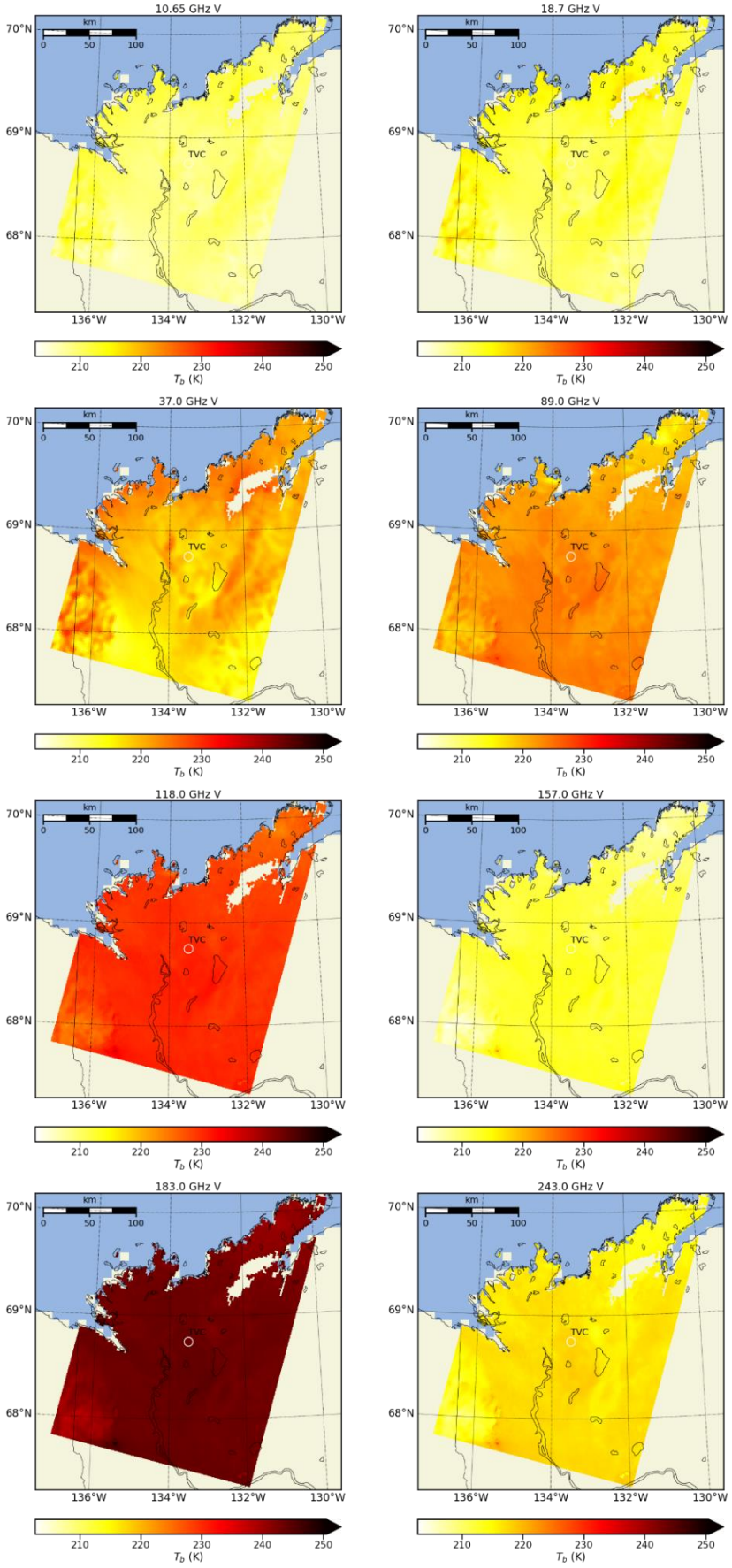

Figure 4.5 Maps showing simulated brightness temperatures (T_B) at different frequencies: 10.65, 18.7, 37, 89, 118, 157, 183 and 243 GHz.

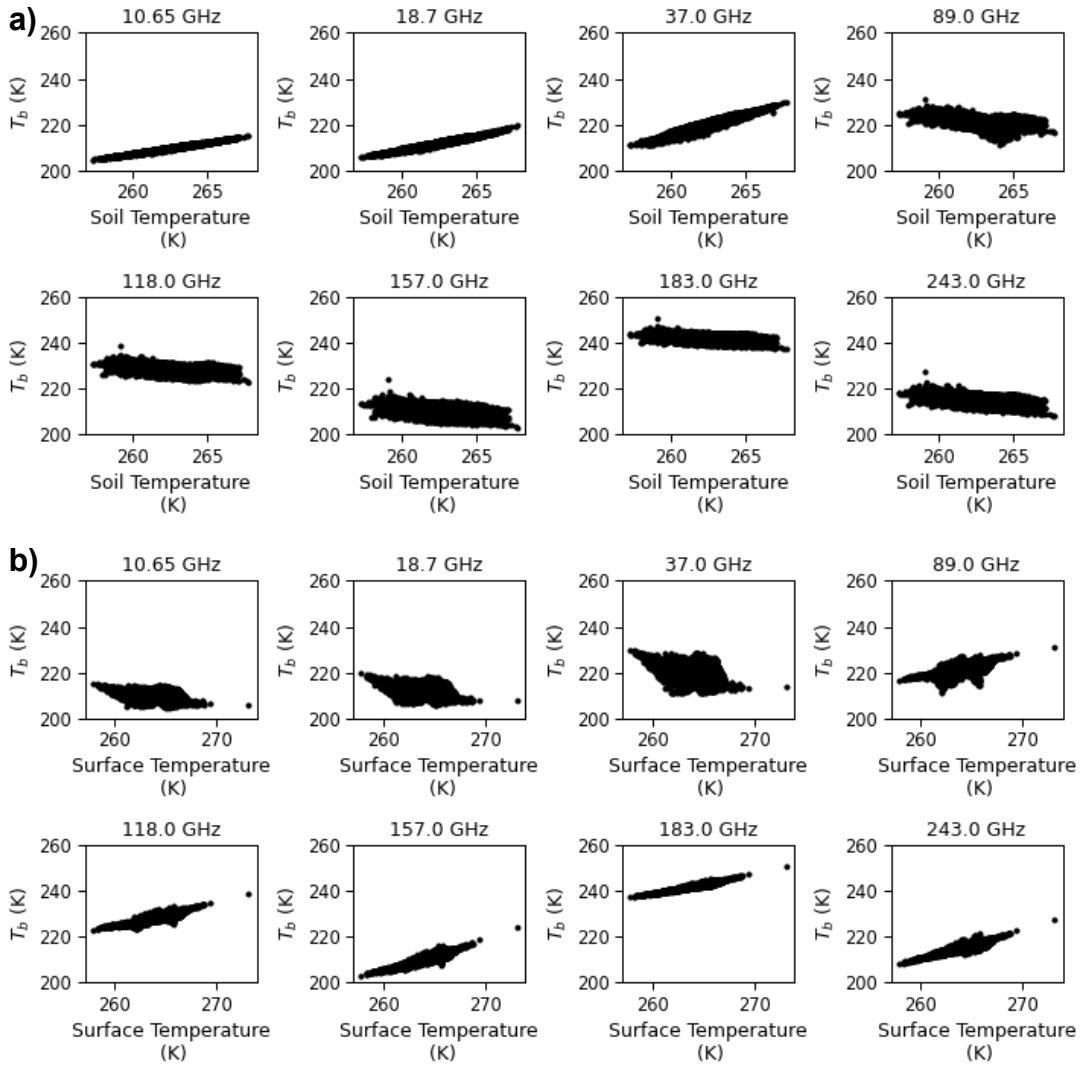

Figure 4.6 Scatter graphs comparing brightness temperatures (T_B) with a) Soil temperature and b) snow surface temperature at 10.65, 18.7, 37, 89, 118, 157, 183 and 243 GHz.

Snow microstructure has a more complex relationship with T_B. Surface snow density and T_B comparisons at all frequencies are shown in Figure 4.7a. The scatter plots show a slight negative relationship (r < -0.45) between T_B and snow density at frequencies below 37 GHz. Higher frequencies show almost no relationship between T_B and snow density ($r \approx 0$). It is expected that surface snow density would have more influence on T_B, however, the density values are high (> 200 kg m^{-3}) suggesting that the surface layer is not fresh snow. This would decrease penetration depth through the snowpack at these frequencies (Harlow, 2011). Figure 4.7b compares surface grain size with T_B at all frequencies. T_B decreases as surface grain size increases, although this

relationship is weak (overall $r <$ -0.35) and particularly weak at higher frequencies ($r \approx 0$). However, it can be noted that T_B becomes more varied as grain size goes above 0.15 mm which seems to skew the results. An increase in grain size will also decrease the penetration depth and cause T_B to be more varied.

These results show that T_B is spatially variable in the Arctic and is strongly influenced by frequency, snow properties, and substrate properties (i.e., everything below the snowpack).

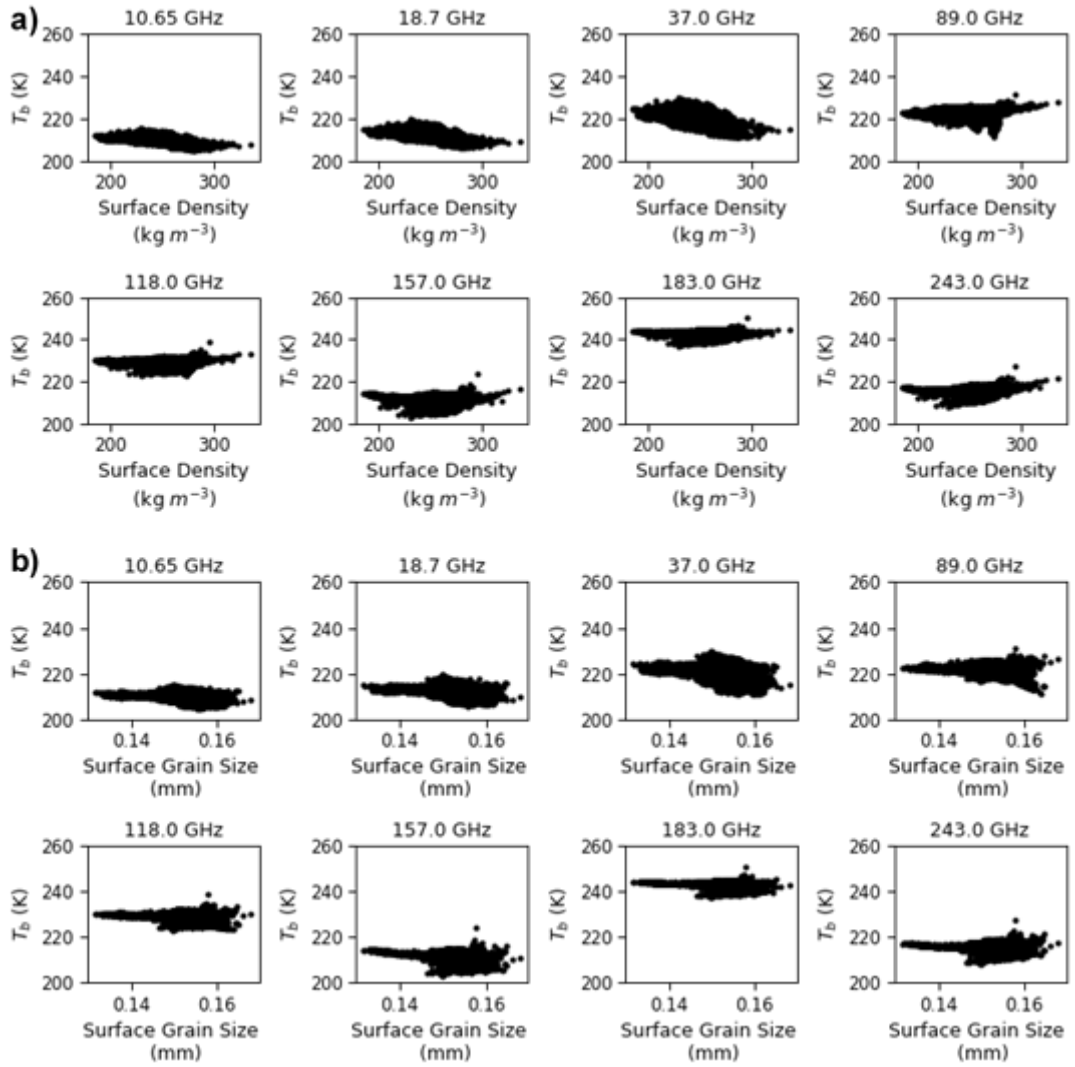

Figure 4.7 Scatter graphs comparing brightness temperatures (T_B) with a) snow surface density and b) snow surface grain size at 10.65, 18.7, 37, 89, 118, 157, 183 and 243 GHz.

4.8 Chapter Summary

In this chapter, a snow model, FSM was coupled with a snow radiative transfer model, SMRT. This began with an overview of microwave theory and how microwave emissions interact with snow and the atmosphere. The structure, physics, and parametrizations of SMRT were discussed in detail with justifications provided for the selection of specific parameters. Sensitivity analysis using SMRT showed snow grain size had the greatest impact on T_Bs, highlighting the critical role of accurate grain size modelling. This directly addresses objective iii of research question 2.

SMRT was driven by different parametrizations of FSM-simulated snow properties, as well as in-situ snow pit observations, and the simulated T_Bs were compared to ground-based radiometer measurements. This fulfils objectives i, ii and iv of research question 2 (section 1.2.2.1), by demonstrating that both modelled and observed snowpack profiles can be used to drive radiative transfer simulations.

Results showed that FSM-SMRT simulated T_Bs were broadly consistent with ground-based observations and showed comparable accuracy to simulations driven by using snow pit inputs. However, residual inaccuracies in T_B simulations were because of variations in snow grain size produced by FSM, as discussed in chapter 3. These findings confirm the model's sensitivity to microstructure, particularly grain size, and underscore the necessity of a physically robust snow microstructure model for accurately simulating microwave emissions in Arctic snowpack conditions.

Finally, SMRT was driven by FSM outputs and run across multiple points in the region surrounding TVC. Simulations showed that T_B is influenced by spatial variations in surface properties, particularly snow depth and microstructure (i.e. snow grain size and snow density). These results showed that surface emissivity is highly dependent on correctly capturing local snowpack variability. This work fulfils research question 3 objectives i, ii and iii (section 1.2.3.1), by scaling FSM and SMRT to a regional domain, assessing

the spatial variability of simulated T_Bs, and establishing relationships between T_B and snowpack characteristics.

These findings have important implications beyond the immediate scope of this thesis. They demonstrate that accurate simulation of snow microstructure – particularly grain size – is essential not only for emissivity prediction but also for improving the assimilation of satellite radiance in NWP systems. The FSM-SMRT coupling, while not perfect, offers a scalable and physically grounded approach for simulating Arctic surface emissivity, with broader applications in cryosphere monitoring, permafrost modelling, and satellite mission development in polar regions.

Chapter 5 Conclusions

This thesis aimed to improve the understanding and predictability of snow emissivity, by coupling a snow model with a snow radiative transfer model and evaluating them in comparison with observations. The concluding chapter will summarise and discuss the findings of this thesis, as well as suggest further work and applications of these findings.

5.1 Summary of Findings

The complex nature of the Arctic climate system has resulted in amplified warming of the region, resulting in a decline in snow cover and sea ice (Notz & Stroeve, 2016; Osborne et al., 2018). This has initiated a positive feedback loop that has intensified warming due to a reduction in surface albedo (Pithan & Mauritsen, 2014; Serreze et al., 2009; Stuecker et al., 2018).

To understand the local and regional effects of this warming, in-situ data is needed to improve the accuracy of climate models and weather forecasts. However, reliable in-situ data is sparse in these regions (Williamson et al., 2017). In recent years, the assimilation of microwave emissivity data has been a core content of global NWP models. At 50 and 183 GHz, atmospheric temperature and humidity profiles, which are vital for correcting initial forecast conditions, can be obtained from passive microwave satellites (English et al., 2000; Harlow, 2009; Liu et al., 2016). However, the highly variable emissivity of the snow and ice makes microwave sounding over snow difficult and datasets from microwave satellites are often not assimilated into NWP models (Geer et al., 2014). The properties of a snowpack are crucial to understanding the emissivity of snow and ice. Therefore, this thesis coupled a snow model (FSM) with a snow microwave radiative transfer model (SMRT) to accurately simulate emissivities across frequencies. FSM is an accumulation and melt model that simulates snow microstructure properties such as snow grain size, snow density, and snow temperature. SMRT is a multi-layer microwave radiative transfer model that simulates T_B. Both models were run at TVC in Canada (the study area) and compared with ground data to assess the

accuracy of the models. SMRT, with inputs from FSM, was also run at NWP grid scales to assess the impact of using alternative model configurations in FSM on simulated T_B, and to assess the applicability of this method over the model grid scale.

In chapter 2, the importance of robust and complete meteorological datasets to drive physical models was discussed. In-situ datasets in the Arctic are often sparse and unreliable due to their remote locations. A time series of eight meteorological variables at hourly intervals from October 2017 to September 2018 from two adjacent AWSs in TVC, provides an accurate dataset. However, this dataset was incomplete and needed to be gap-filled with alternative datasets. The alternative datasets, ERA5 reanalysis, bias-corrected ERA5, WFDE5, and NWP, were discussed and compared with the observations. The bias-corrected ERA5 dataset performed best across all variables and was selected as the most suitable for gap-filling the missing observations and would be used for FSM point modelling. The NWP dataset would be used for multipoint modelling, due to its high spatial coverage and resolution.

The overall objective of chapter 3 was to demonstrate how well a snow model can reproduce a typical Arctic tundra snowpack. Initially, a two-layer snowpack was proposed: a basal layer of low-density, coarse-grained snow called depth hoar, and an upper layer of dense, fine-grained snow called wind slab. This sometimes includes a third layer of fresh snow on top of the wind slab layer. The spatial and temporal variability of snow cover can make accurate modelling difficult. Therefore, snow datasets, including in-situ and estimated snow depth, in-situ and estimated SWE data, and in-situ measurements of snow properties, are crucial for evaluating the accuracy of snow models. The physics, mechanics, and parameterisations of FSM were discussed. Modifications to FSM were added, including an alternative grain growth model and the option to have deforming layers that simulate wind slabs. Finally, FSM was run at a single point (at multiple AOIs in TVC) and multiple points across the Northwest Canada and Alaska region. Overall FSM failed to accurately capture the characteristics of a typical Arctic snowpack when compared with

profiles of measured snow properties such as snow grain size, snow density, and snow temperature. The JULES snow grain model underestimated snow grain size but performed better than the SNTHERM grain growth model, which significantly overestimated grain size. This agrees with previous work when comparing both models with observations (Jordan, 1991; Sandells et al., 2017). Snow density simulations were improved by the inclusion of a wind packing model and FSM was able to simulate a dense wind slab layer in most profiles. However, FSM could not simulate the low-density basal layer of most snowpacks. This is because FSM does not simulate upward water vapour transfer which occurs in shallow Arctic snowpacks due to high vertical temperature gradients (Domine et al., 2019). Multipoint FSM simulations of SWE compared to the GlobSnow dataset SWE had high errors (RMSE = 111.34 mm) and low correlation (r = 0.07). FSM performed better for shallower snowpacks (SWE ≤ 150 mm), which is consistent with the GlobSnow comparison (i.e. Luojus et al., 2021).

Chapter 4 used FSM simulations of snow properties to run SMRT and obtain simulated T_Bs. Firstly, microwave theory and its interactions with snow and the atmosphere were explored. This was followed by a detailed description of SMRT including its structure, mechanics, and key configurations. SMRT offers many user-selected configurations and justification of these selections was discussed. To assess which snow property has the greatest influence on simulated T_B, sensitivity analysis was performed. The results indicate that snow grain size exhibited the highest sensitivity. Simulated T_bs were compared with ground-based radiometer observations of T_B. SMRT was driven by different configurations of FSM, including the JULES and SNTHERM grain growth models and the wind packing density model. Snow pit data was also used as inputs to SMRT. Results show that when SMRT was coupled with the SNTHERM grain growth model T_B was significantly overestimated at 89 GHz and errors were high (MBE = -85.6 K and RMSE = 108.7 K). The other models performed better and were like SMRT simulations driven by snow pit data.

Multipoint FSM simulations were inputted into SMRT to simulate spatial patterns of T_B. In general, T_B increased with frequency except in the two atmospheric windows around 157 and 243 GHz.

T_B at different frequencies was also compared to various properties including soil temperature, snow surface temperature, snow density, and snow grain size. At lower frequencies (≤ 37 GHz) T_B is strongly influenced by soil temperature ($r > 0.98$) and at higher frequencies (≥ 89 GHz) T_B is influenced by the surface temperature. This is expected, as at higher frequencies microwave emissions can penetrate through the snowpack. Snow microstructure showed slight negative relationships with T_B.

The main implications of this thesis, either directly obtained or otherwise can be summarised as:

- The need for complete and accurate datasets to run physical models has been demonstrated, particularly in the Arctic where weather stations are sparse. This has an impact on multiple fields including hydrology, climatology, and ecology (Slater et al., 2013)
- Many detailed snowpack models were first developed for avalanche forecasting i.e., Crocus (Vionnet et al., 2012) and SNOWPACK (Bartelt & Lehning, 2002) and are not good representations of a typical Arctic snowpack (Barrere et al., 2017; Domine et al., 2019; Fourteau et al., 2021) The testing and development of FSM in this thesis has shown its potential to replicate an Arctic tundra snowpack but has also highlighted the need for further development.
- This thesis has shown significant spatial and temporal variability in the microwave emissivity of Arctic tundra snow. This highlights the necessity of accurately simulating emissivity based on accurately modelled or observed microphysical snow properties, rather than relying on fixed emissivity values, a method currently used in many NWP systems.(Geer et al., 2014; Hirahara et al., 2020; Lawrence et al., 2019; Wivell et al., 2023)

5.2 Future Work and Applications

To further develop snow emissivity modelling and its integration into NWP models, the following research that was beyond the scope of this thesis is recommended:

- **Development of wind redistribution in FSM:** as discussed snow cover in the Arctic is shaped by the wind. Having a realistic parametrisation that models wind would increase the accuracy of snow modelling.
- **Use SMRT to retrieve SWE dataset:** Passive T_B can be used to estimate SWE at certain frequencies. This could be compared with in-situ SWE data and modelled SWE data to further test the capabilities of both models.
- **FSM driven SMRT simulations compared with microwave data from airborne and satellite sensors:** To further develop and validate SMRT it will need to be compared with larger datasets. While this thesis and others (Sandells et al., 2024) have shown SMRT's capability, comparing it with a broader dataset will help to understand if SMRT can be applied across different Arctic and sub-Arctic environments.
- **Offline coupling of SMRT, FSM, and Radiance Simulator:** Developing on the work in this thesis and others (i.e. Wivell et al., 2023), simulations from SMRT can be converted into emissivities and coupled with the Radiance Simulator to predict top-of-atmosphere radiance and compared with satellite data. This will assess the potential of modelled emissivity being assimilated into NWP models.
- **Online SMRT-NWP Coupling:** If the offline SMRT modelling shows accurate results, integration with the Met Office land surface model could be explored.

Appendix A FSM Snow Profile Simulations

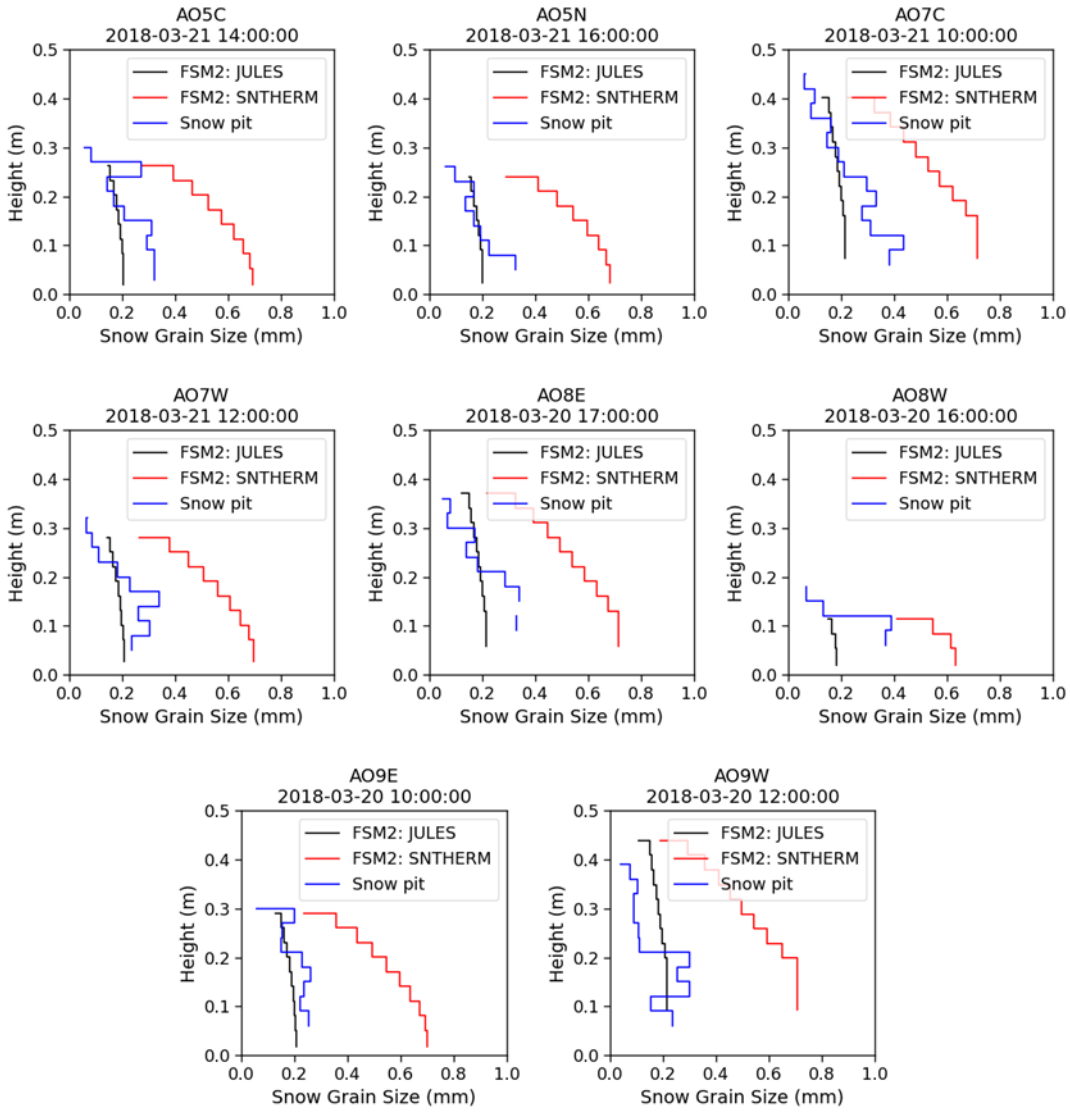

Figure A1 Vertical profiles of snow grain size comparing in-situ observations (blue line) with two FSM parametrisations: the JULES snow grain model (black line) and SNTHERM snow grain model (red line). Each panel (a-j) corresponds to a different Area of Interest (AOI) in TVC, with time and date indicating when the snow pit measurements were taken.

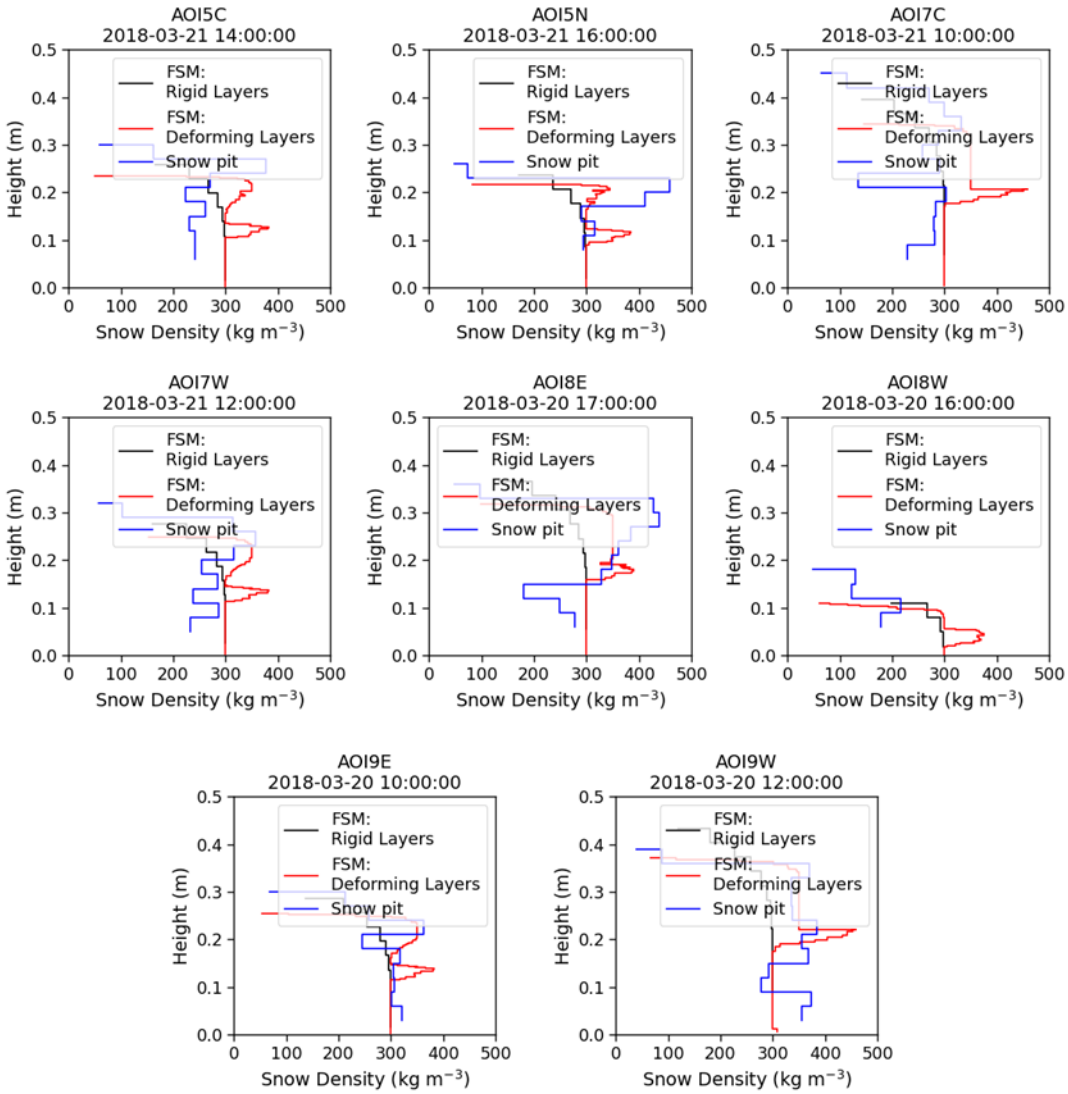

Figure A2 Vertical profiles of snow density comparing in-situ observations (blue line) with two FSM parameterizations: the rigid layers model (black line) and the deforming layers model (red line). Each panel (a–j) corresponds to a different Area of Interest (AOI) in TVC, with the date and time indicating when the snow pit measurements were taken.

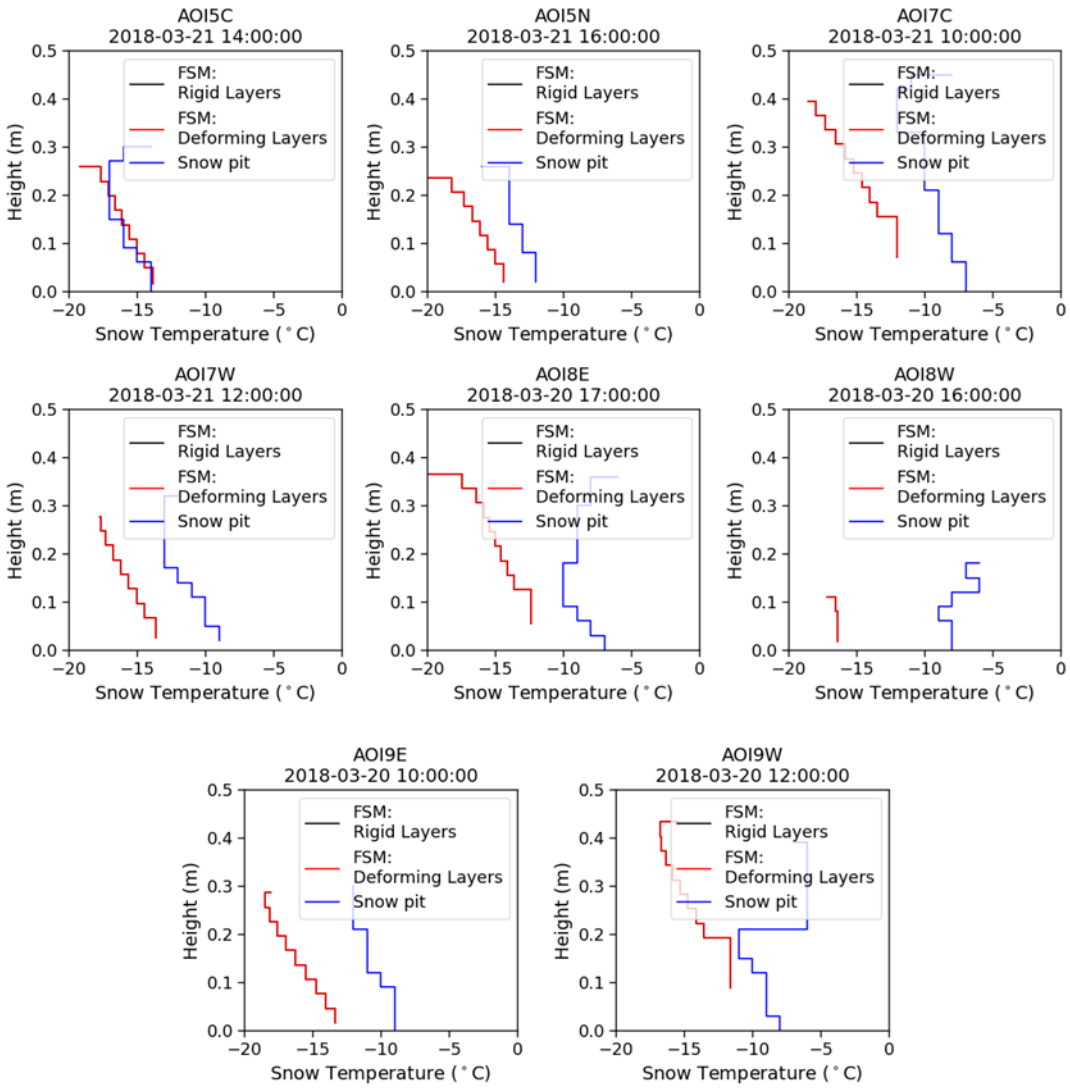

Figure A3 Vertical profiles of snow temperature comparing in-situ observations (blue line) with two FSM parameterizations: the rigid layers model (black line) and the deforming layers model (red line). Each panel (a–j) corresponds to a different Area of Interest (AOI) in TVC, with the date and time indicating when the snow pit measurements were taken.

References

Abdelhamed, M. S., Elshamy, M. E., Razavi, S., & Wheater, H. S. (2023). Challenges in Hydrologic-Land Surface Modeling of Permafrost Signatures—A Canadian Perspective. *Journal of Advances in Modeling Earth Systems*, *15*(3), e2022MS003013. https://doi.org/10.1029/2022MS003013

Albergel, C., Dutra, E., Munier, S., Calvet, J.-C., Munoz-Sabater, J., de Rosnay, P., & Balsamo, G. (2018). ERA-5 and ERA-Interim driven ISBA land surface model simulations: Which one performs better? *Hydrology and Earth System Sciences*, *22*(6), 3515–3532. https://doi.org/10.5194/hess-22-3515-2018

Alonso-González, E., López-Moreno, J. I., Gascoin, S., García-Valdecasas Ojeda, M., Sanmiguel-Vallelado, A., Navarro-Serrano, F., Revuelto, J., Ceballos, A., Esteban-Parra, M. J., & Essery, R. (2018). Daily gridded datasets of snow depth and snow water equivalent for the Iberian Peninsula from 1980 to 2014. *Earth System Science Data*, *10*(1), 303–315. https://doi.org/10.5194/essd-10-303-2018

Anderson, J., & Wirt, J. (2008). Ultrasonic snow depth sensor accuracy, reliability and performanc. *76th Western Snow Conference*, 99–105.

Andersson, E., & Thépaut, J.-N. (2008). *ECMWF's 4D-Var data assimilation system – the genesis and ten years in operations*. https://doi.org/10.21957/WNMGUIMIHE

Appel, F., Koch, F., Rösel, A., Klug, P., Henkel, P., Lamm, M., Mauser, W., & Bach, H. (2019). Advances in Snow Hydrology Using a Combined Approach of GNSS In Situ Stations, Hydrological Modelling and Earth Observation—A Case Study in Canada. *Geosciences*, *9*(1), Article 1. https://doi.org/10.3390/geosciences9010044

Baker-Jarvis, J. (2000). A generalized dielectric polarization evolution equation. *IEEE Transactions on Dielectrics and Electrical Insulation*. https://doi.org/10.1109/94.848919

Bannister, R. N. (2017). A review of operational methods of variational and ensemble-variational data assimilation. *Quarterly Journal of the Royal Meteorological Society*, *143*(703), 607–633. https://doi.org/10.1002/qj.2982

Barnhart, T. B., Molotch, N. P., Livneh, B., Harpold, A. A., Knowles, J. F., & Schneider, D. (2016). Snowmelt rate dictates streamflow. *Geophysical Research Letters*, *43*(15), 8006–8016. https://doi.org/10.1002/2016GL069690

Barrere, M., Domine, F., Decharme, B., Morin, S., Vionnet, V., & Lafaysse, M. (2017). Evaluating the performance of coupled snow-soil models in SURFEXv8 to simulate the permafrost thermal regime at a high Arctic site. *Geoscientific Model Development*, *10*(9), 3461–3479. https://doi.org/10.5194/gmd-10-3461-2017

Bartelt, P., & Lehning, M. (2002). A physical SNOWPACK model for the Swiss avalanche warning. *Cold Regions Science and Technology*, *35*(3), 123–145. https://doi.org/10.1016/S0165-232X(02)00074-5

Batrak, Y., & Müller, M. (2019). On the warm bias in atmospheric reanalyses induced by the missing snow over Arctic sea-ice. *Nature Communications*, *10*(1), 4170. https://doi.org/10.1038/s41467-019-11975-3

Bauer, P., Magnusson, L., Thépaut, J.-N., & Hamill, T. M. (2016). Aspects of ECMWF model performance in polar areas. *Quarterly Journal of the Royal Meteorological Society*, *142*(695), 583–596. https://doi.org/10.1002/qj.2449

Bauer, P., Thorpe, A., & Brunet, G. (2015). The quiet revolution of numerical weather prediction. *Nature*, *525*(7567), 47–55. https://doi.org/10.1038/nature14956

Bergman, J. A. (1989). An evaluation of the acoustic snow depth sensor in a deep Sierra Nevada snowpack. *57th Annual Western Snow Conference*.

Berrisford, P., Dee, D. P., Poli, P., Brugge, R., Fielding, M., Fuentes, M., K\r allberg, P. W., Kobayashi, S., Uppala, S., & Simmons, A. (2011). *The ERA-Interim archive Version 2.0*. *1*, 23.

Berteaux, D., Gauthier, G., Domine, F., Ims, R. A., Lamoureux, S. F., Lévesque, E., & Yoccoz, N. (2017). Effects of changing permafrost and snow conditions on tundra wildlife: Critical places and times. *Arctic Science*, *3*(2), 65–90. https://doi.org/10.1139/as-2016-0023

Best, M. J., Pryor, M., Clark, D. B., Rooney, G. G., Essery, R. . L. H., Ménard, C. B., Edwards, J. M., Hendry, M. A., Porson, A., Gedney, N., Mercado, L. M., Sitch, S., Blyth, E., Boucher, O., Cox, P. M., Grimmond, C. S. B., & Harding, R. J. (2011). The Joint UK Land Environment Simulator (JULES), model description – Part 1: Energy and water fluxes. *Geoscientific Model Development*, *4*(3), 677–699. https://doi.org/10.5194/gmd-4-677-2011

Bhardwaj, A., Sam, L., Bhardwaj, A., & Martín-Torres, F. J. (2016). LiDAR remote sensing of the cryosphere: Present applications and future prospects. *Remote Sensing of Environment*, *177*, 125–143. https://doi.org/10.1016/j.rse.2016.02.031

Billecocq, P., Langlois, A., & Montpetit, B. (2024). Subgridding high-resolution numerical weather forecast in the Canadian Selkirk mountain range for local snow modeling in a remote sensing perspective. *The Cryosphere*, *18*(6), 2765–2782. https://doi.org/10.5194/tc-18-2765-2024

Bitz, C. M., & Fu, Q. (2008). Arctic warming aloft is data set dependent. *Nature*, *455*(7210), E3–E4. https://doi.org/10.1038/nature07258

Blanchard-Wrigglesworth, E., Barthélemy, A., Chevallier, M., Cullather, R., Fučkar, N., Massonnet, F., Posey, P., Wang, W., Zhang, J., Ardilouze, C., Bitz, C. M., Vernieres, G., Wallcraft, A., & Wang, M. (2017). Multi-model seasonal forecast of Arctic sea-ice: Forecast uncertainty at pan-Arctic and regional scales. *Climate Dynamics*, *49*(4), 1399–1410. https://doi.org/10.1007/s00382-016-3388-9

Bonavita, M., Trémolet, Y., Holm, E., Lang, S. T. K., Chrust, M., Janisková, M., Lopez, P., Laloyaux, P., Rosnay, P. D., Fisher, M., Hamrud, M., &

English, S. (2017). A Strategy for Data Assimilation. *ECMWF Tech Memo*, *800*(April).

Brönnimann, S., Rajczak, J., Fischer, E., Raible, C., Rohrer, M., & Schär, C. (2018). Changing seasonality of moderate and extreme precipitation events in the Alps. *Natural Hazards and Earth System Sciences*. https://doi.org/10.5194/nhess-18-2047-2018

Brown, R. D., Fang, B., & Mudryk, L. (2019). Update of Canadian Historical Snow Survey Data and Analysis of Snow Water Equivalent Trends, 1967–2016. *Atmosphere-Ocean*, *57*(2), 149–156. https://doi.org/10.1080/07055900.2019.1598843

Brucker, L., Picard, G., Arnaud, L., Barnola, J.-M., Schneebeli, M., Brunjail, H., Lefebvre, E., & Fily, M. (2011). Modeling time series of microwave brightness temperature at Dome C, Antarctica, using vertically resolved snow temperature and microstructure measurements. *Journal of Glaciology*, *57*(201), 171–182. https://doi.org/10.3189/002214311795306736

Brun, E., David, P., Sudul, M., & Brunot, G. (1992). A nutnerical tnodel to simulate snow-cover stratigraphy for operational avalanche forecasting. *Journal of Glaciology*. https://doi.org/10.3189/s0022143000009552

Case, J. L., LaFontaine, F. J., Bell, J. R., Jedlovec, G. J., Kumar, S. V., & Peters-Lidard, C. D. (2013). A real-time MODIS vegetation product for land surface and numerical weather prediction models. *IEEE Transactions on Geoscience and Remote Sensing*, *52*(3), 1772–1786.

Colbeck, S. C., & Anderson, E. A. (1982). The permeability of a melting snow cover. *Water Resources Research*. https://doi.org/10.1029/WR018i004p00904

Collins, M., Knutti, R., Arblaster, J., Dufresne, J.-L., Fichefet, T., Friedlingstein, P., Gao, X., Gutowski, W. J., T. Johns, G., Krinner, Shongwe, M., Tebaldi, C., Weaver, A. J., & Wehner, M. (2013). Long-term climate change: Projections, commitments and irreversibility. In *Climate Change 2013 the Physical Science Basis: Working Group I Contribution to the Fifth Assessment Report of the Intergovernmental*

Panel on Climate Change.
https://doi.org/10.1017/CBO9781107415324.024

Corona, J., Muñoz, J., Lakhankar, T., Romanov, P., & Khanbilvardi, R. (2015). Evaluation of the Snow Thermal Model (SNTHERM) through Continuous in situ Observations of Snow's Physical Properties at the CREST-SAFE Field Experiment. *Geosciences*, *5*(4), 310–333. https://doi.org/10.3390/geosciences5040310

Cucchi, M., Weedon, G. P., Amici, A., Bellouin, N., Lange, S., Müller Schmied, H., Hersbach, H., & Buontempo, C. (2020). WFDE5: Bias-adjusted ERA5 reanalysis data for impact studies. *Earth System Science Data*, *12*(3), 2097–2120. https://doi.org/10.5194/essd-12-2097-2020

de Leeuw, N., Birkeland, K., & Hendrikx, J. (2023). *UNDERSTANDING METEOROLOGICAL CONTROLS ON WIND SLAB PROPERTIES*.

DeBeer, C. M., & Pomeroy, J. W. (2017). Influence of snowpack and melt energy heterogeneity on snow cover depletion and snowmelt runoff simulation in a cold mountain environment. *Journal of Hydrology*, *553*, 199–213. https://doi.org/10.1016/j.jhydrol.2017.07.051

Dee, D. P., & Uppala, S. (2009). Variational bias correction of satellite radiance data in the ERA-Interim reanalysis. *Quarterly Journal of the Royal Meteorological Society*. https://doi.org/10.1002/qj.493

Dee, D. P., Uppala, S. M., Simmons, A. J., Berrisford, P., Poli, P., Kobayashi, S., Andrae, U., Balmaseda, M. A., Balsamo, G., Bauer, P., Bechtold, P., Beljaars, A. C. M., van de Berg, L., Bidlot, J., Bormann, N., Delsol, C., Dragani, R., Fuentes, M., Geer, A. J., … Vitart, F. (2011). The ERA-Interim reanalysis: Configuration and performance of the data assimilation system. *Quarterly Journal of the Royal Meteorological Society*, *137*(656), 553–597. https://doi.org/10.1002/qj.828

Derksen, C., & Brown, R. (2012). Spring snow cover extent reductions in the 2008-2012 period exceeding climate model projections. *Geophysical Research Letters*. https://doi.org/10.1029/2012GL053387

Derksen, C., Silis, A., Sturm, M., Holmgren, J., Liston, G. E., Huntington, H., & Solie, D. (2009). Northwest Territories and Nunavut Snow Characteristics from a Subarctic Traverse: Implications for Passive Microwave Remote Sensing. *Journal of Hydrometeorology*, *10*(2), 448–463. https://doi.org/10.1175/2008JHM1074.1

Domine, F., Barrere, M., & Sarrazin, D. (2016). Seasonal evolution of the effective thermal conductivity of the snow and the soil in high Arctic herb tundra at Bylot Island, Canada. *The Cryosphere*, *10*(6), 2573–2588. https://doi.org/10.5194/tc-10-2573-2016

Domine, F., Gauthier, G., Vionnet, V., Fauteux, D., Dumont, M., & Barrere, M. (2018). Snow physical properties may be a significant determinant of lemming population dynamics in the high Arctic. *Arctic Science*, *4*(4), 813–826. https://doi.org/10.1139/as-2018-0008

Domine, F., Picard, G., Morin, S., Barrere, M., Madore, J. B., & Langlois, A. (2019). Major Issues in Simulating Some Arctic Snowpack Properties Using Current Detailed Snow Physics Models: Consequences for the Thermal Regime and Water Budget of Permafrost. *Journal of Advances in Modeling Earth Systems*, *11*(1), 34–44. https://doi.org/10.1029/2018MS001445

Dong, C. (2018). Remote sensing, hydrological modeling and in situ observations in snow cover research: A review. *Journal of Hydrology*, *561*, 573–583. https://doi.org/10.1016/j.jhydrol.2018.04.027

English, S. J., Renshaw, R. J., Dibben, P. C., Smith, A. J., Rayer, P. J., Poulsen, C., Saunders, F. W., & Eyre, J. R. (2000). A comparison of the impact of TOVS and ATOVS satellite sounding data on the accuracy of numerical weather forecasts. *Quarterly Journal of the Royal Meteorological Society*. https://doi.org/10.1256/smsqj.56914

Environment and Climate Change Canada. (2018). *Extracted from the Environment and Climate Change Canada Historical Climate Data web site on 01/10/2018* [Dataset]. (https://climate.weather.gc.ca/index_e.html)

Essery, R. (2015). A factorial snowpack model (FSM 1.0). *Geoscientific Model Development*, *8*(12), 3867–3876. https://doi.org/10.5194/gmd-8-3867-2015

Essery, R., Morin, S., Lejeune, Y., B Ménard, C., Ménard, C. B., & B Ménard, C. (2013). A comparison of 1701 snow models using observations from an alpine site. *Advances in Water Resources*, *55*, 131–148. https://doi.org/10.1016/j.advwatres.2012.07.013

Essery, R., & Pomeroy, J. (2004). Vegetation and Topographic Control of Wind-Blown Snow Distributions in Distributed and Aggregated Simulations for an Arctic Tundra Basin. *Journal of Hydrometeorology*, *5*(5), 735–744. https://doi.org/10.1175/1525-7541(2004)005<0735:VATCOW>2.0.CO;2

Fierz, C., R.L, A., Y, D., P, E., Greene, E., Mcclung, D., Nishimura, K., Satyawali, P., & Sokratov, S. (2009). *The international classification for seasonal snow on the ground (UNESCO, IHP (International Hydrological Programme)–VII, Technical Documents in Hydrology, No 83; IACS (International Association of Cryospheric Sciences) contribution No 1)*.

Flato, G., Marotzke, J., Abiodun, B., Braconnot, P., Chou, S. C., Collins W, Cox, P., Driouech, F., Emori, S., Eyring, V., Forest, Gleckler, P., Guilyardi, E., Jakob, C., Kattsov, V., Reason, C., & Rummukainen, M. (2013). Evaluation of climate models. In *Climate Change 2013 the Physical Science Basis: Working Group I Contribution to the Fifth Assessment Report of the Intergovernmental Panel on Climate Change*. https://doi.org/10.1017/CBO9781107415324.020

Fleming, S. W., Bourdin, D. R., Campbell, D., Stull, R. B., & Gardner, T. (2015). Development and operational testing of a super-ensemble artificial intelligence flood-forecast model for a Pacific Northwest river. *JAWRA Journal of the American Water Resources Association*, *51*(2), 502–512.

Förster, K., Meon, G., Marke, T., & Strasser, U. (2014). Effect of meteorological forcing and snow model complexity on hydrological simulations in the Sieber catchment (Harz Mountains, Germany). *Hydrology and Earth System Sciences*, *18*(11), 4703–4720. https://doi.org/10.5194/hess-18-4703-2014

Fourteau, K., Domine, F., & Hagenmuller, P. (2021). Impact of water vapor diffusion and latent heat on the effective thermal conductivity of snow. *The Cryosphere*, *15*(6), 2739–2755. https://doi.org/10.5194/tc-15-2739-2021

Gallet, J. C., Domine, F., Zender, C. S., Picard, G., The Cryosphere, J. C. G., Domine, F., Zender, C. S., Picard, G., & Cryosphere, T. (2009). Measurement of the Specific Surface Area of Snow Using Infrared Reflectance in an Integrating Sphere at 1310 and 1550 Nm'. *Cryosphere*, *3*(2), 167–182. https://doi.org/10.5194/tc-3-167-2009.

Gao, C., Xiu, A., Zhang, X., Tong, Q., Zhao, H., Zhang, S., Yang, G., & Zhang, M. (2022). Two-way coupled meteorology and air quality models in Asia: A systematic review and meta-analysis of impacts of aerosol feedbacks on meteorology and air quality. *Atmospheric Chemistry and Physics*, *22*(8), 5265–5329.

Geer, A. J., Baordo, F., Bormann, N., & English, S. (2014). *All-sky assimilation of microwave humidity sounders*. *November*. http://www.ecmwf.int/en/research/publications

Gelaro, R., McCarty, W., Suárez, M. J., Todling, R., Molod, A., Takacs, L., Randles, C. A., Darmenov, A., Bosilovich, M. G., Reichle, R., Wargan, K., Coy, L., Cullather, R., Draper, C., Akella, S., Buchard, V., Conaty, A., da Silva, A. M., Gu, W., … Zhao, B. (2017). The modern-era retrospective analysis for research and applications, version 2 (MERRA-2). *Journal of Climate*. https://doi.org/10.1175/JCLI-D-16-0758.1

Goosse, H., Kay, J. E., Armour, K. C., Bodas-Salcedo, A., Chepfer, H., Docquier, D., Jonko, A., Kushner, P. J., Lecomte, O., Massonnet, F., Park, H. S., Pithan, F., Svensson, G., & Vancoppenolle, M. (2018). Quantifying climate feedbacks in polar regions. In *Nature Communications*. https://doi.org/10.1038/s41467-018-04173-0

Grenfell, T. C., & Warren, S. G. (1999). Representation of a nonspherical ice particle by a collection of independent spheres for scattering and absorption of radiation. *Journal of Geophysical Research Atmospheres*. https://doi.org/10.1029/1999JD900496

Grünberg, I., Wilcox, E. J., Zwieback, S., Marsh, P., & Boike, J. (2020). Linking tundra vegetation, snow, soil temperature, and permafrost. *Biogeosciences*, *17*(16), 4261–4279. https://doi.org/10.5194/bg-17-4261-2020

Guedj, S., Karbou, F., Rabier, F., & Bouchard, A. (2010). Toward a Better Modeling of Surface Emissivity to Improve AMSU Data Assimilation Over Antarctica. *IEEE Transactions on Geoscience and Remote Sensing*, *48*(4), 1976–1985. IEEE Transactions on Geoscience and Remote Sensing. https://doi.org/10.1109/TGRS.2009.2036254

Hagenmuller, P., Matzl, M., Chambon, G., & Schneebeli, M. (2016). Sensitivity of snow density and specific surface area measured by microtomography to different image processing algorithms. *Cryosphere*. https://doi.org/10.5194/tc-10-1039-2016

Harlow, R. C. (2009). Millimeter Microwave Emissivities and Effective Temperatures of Snow-Covered Surfaces: Evidence for Lambertian Surface Scattering. *IEEE Transactions on Geoscience and Remote Sensing*, *47*(7), 1957–1970. https://doi.org/10.1109/TGRS.2008.2011893

Harlow, R. C. (2011). Sea Ice Emissivities and Effective Temperatures at MHS Frequencies: An Analysis of Airborne Microwave Data Measured During Two Arctic Campaigns. *IEEE Transactions on Geoscience and Remote Sensing*, *49*(4), 1223–1237. https://doi.org/10.1109/TGRS.2010.2051555

Harlow, R. C., & Essery, R. (2012). Tundra Snow Emissivities at MHS Frequencies: MEMLS Validation Using Airborne Microwave Data Measured During CLPX-II. *IEEE Transactions on Geoscience and Remote Sensing*, *50*(11), 4262–4278. https://doi.org/10.1109/TGRS.2012.2193132

Hersbach, H. (2019). Global reanalysis: Goodbye ERA-Interim, hello ERA5. In *ECMWF Newsletter* (Vol. 159, p. 17). https://cir.nii.ac.jp/crid/1370009142513757452

Hersbach, H., Bell, B., Berrisford, P., Biavati, G., Horányi, A., Muñoz Sabater, J., Nicolas, J., Peubey, C., Radu, R., Rozum, I., Schepers, D., Simmons, A., Soci, C., Dee, D., & Thépaut, J.-N. (2023). https://doi.org/10.24381/cds.adbb2d47

Hersbach, H., Bell, B., Berrisford, P., Hirahara, S., Horányi, A., Muñoz-Sabater, J., Nicolas, J., Peubey, C., Radu, R., Schepers, D., Simmons, A., Soci, C., Abdalla, S., Abellan, X., Balsamo, G.,

Bechtold, P., Biavati, G., Bidlot, J., Bonavita, M., … Thépaut, J. (2020). The ERA5 global reanalysis. *Quarterly Journal of the Royal Meteorological Society*, *146*(730), 1999–2049. https://doi.org/10.1002/qj.3803

Hersbach, H., Bell, B., Berrisford, P., Horányi, A., Sabater, J. M., Nicolas, J., Radu, R., Schepers, D., Simmons, A., Soci, C., & Dee, D. (2019). Global reanalysis: Goodbye ERA-Interim, hello ERA5. *ECMWF Newsletter*.

Hewage, P. R. P. G., & Padmasiri, P. R. (2020). *Empirical Evaluation of Artificial Intelligence Based Customised Weather Forecasting and Monitoring Model for the Agriculture Sector* [PhD Thesis]. Edge Hill University.

Hijmans, R. J., Cameron, S. E., Parra, J. L., Jones, P. G., & Jarvis, A. (2005). Very high resolution interpolated climate surfaces for global land areas. *International Journal of Climatology*. https://doi.org/10.1002/joc.1276

Hirahara, Y., Rosnay, P. D., & Arduini, G. (2020). Evaluation of a Microwave Emissivity Module for Snow Covered Area with CMEM in the ECMWF Integrated Forecasting System. *Remote Sensing*, *12*(18), 2946. https://doi.org/10.3390/rs12182946

Houghton, J. T., Taylor, F. W., Rodgers, C. D., & St. (1986). Remote sounding of atmospheres. In *Remote sounding of atmospheres.* https://doi.org/10.1029/eo066i029p00546-02

Huang, J., Zhang, X., Zhang, Q., Lin, Y., Hao, M., Luo, Y., Zhao, Z., Yao, Y., Chen, X., Wang, L., Nie, S., Yin, Y., Xu, Y., & Zhang, J. (2017). Recently amplified arctic warming has contributed to a continual global warming trend. *Nature Climate Change*, *7*(12), 875–879. https://doi.org/10.1038/s41558-017-0009-5

Ishimaru, A. : (1997). *Wave propagation and scattering in random media*. IEEE Press, Oxford University Press.

Jabot, E., Zin, I., Lebel, T., Gautheron, A., & Obled, C. (2012). Spatial interpolation of sub-daily air temperatures for snow and hydrologic applications in mesoscale Alpine catchments. *Hydrological Processes*, *26*(17), 2618–2630. https://doi.org/10.1002/hyp.9423

James, E. P., Benjamin, S. G., & Jamison, B. D. (2020). Commercial-aircraft-based observations for NWP: Global coverage, data impacts, and COVID-19. *Journal of Applied Meteorology and Climatology*, *59*(11), 1809–1825.

Janssen, M. (1994). *Atmospheric remote sensing by microwave radiometry*.

Jones, R. W., Renfrew, I. A., Orr, A., Webber, B. G. M., Holland, D. M., & Lazzara, M. A. (2016). *Journal of Geophysical Research: Atmospheres*. 1–18. https://doi.org/10.1002/2015JD024680.Received

Jordan, R. (1991). A One-Dimensional Temperature Model for a Snow Cover: Technical Documentation for SNTHERM.89. *U.S.Army Corps of Engineers, Cold Regions Research & Engineering Laboratory*, *Special Report 91-16*, 49.

Karbou, F., Rabier, F., & Prigent, C. (2014). The assimilation of observations from the advanced microwave sounding unit over sea ice in the french global numerical weather prediction system. *Monthly Weather Review*, *142*(1), 125–140. https://doi.org/10.1175/MWR-D-13-00025.1

Kinar, N. J., & Pomeroy, J. W. (2015). Measurement of the physical properties of the snowpack. *Reviews of Geophysics*, *53*(2), 481–544. https://doi.org/10.1002/2015RG000481

King, J. (2014). *Remote Sensing Observations of Tundra Snow with Ku- and X-band Radar*. University of Waterloo. Ontaio, Canada.

King, J., Derksen, C., Toose, P., Langlois, A., Larsen, C., Lemmetyinen, J., Marsh, P., Montpetit, B., Roy, A., Rutter, N., & Sturm, M. (2018). The influence of snow microstructure on dual-frequency radar measurements in a tundra environment. *Remote Sensing of Environment*, *215*, 242–254. https://doi.org/10.1016/j.rse.2018.05.028

Kobayashi, S., Ota, Y., Harada, Y., Ebita, A., Moriya, M., Onoda, H., Onogi, K., Kamahori, H., Kobayashi, C., Endo, H., Miyaoka, K., & Kiyotoshi, T. (2015). The JRA-55 reanalysis: General specifications and basic characteristics. *Journal of the Meteorological Society of Japan*. https://doi.org/10.2151/jmsj.2015-001

Kontu, A. (2018). *Effect of Snow Microstructure and Subnivean Water Bodies on Microwave Radiometry of Seasonal Snow; Influence of Fine Structure of Snow and Snow Covered Water Bodies on Snow Microwave Radiation'*. Aalto University; Aalto University.

Kurzrock, F., Cros, S., Chane-Ming, F., Otkin, J., Hutt, A., Linguet, L., Lajoie, G., & Potthast, R. (2018). A review of the use of geostationary satellite observations in regional-scale models for short-term cloud forecasting. *Meteorologische Zeitschrift*, *27*(4), 277–298.

Lawrence, H., Bormann, N., Sandu, I., Day, J., Farnan, J., & Bauer, P. (2019). Use and impact of Arctic observations in the ECMWF Numerical Weather Prediction system. *Quarterly Journal of the Royal Meteorological Society*, *145*(725), 3432–3454. https://doi.org/10.1002/qj.3628

Lazzara, M. A., Weidner, G. A., Keller, L. M., Thom, J. E., & Cassano, J. J. (2012). Antarctic Automatic Weather Station Program: 30 Years of Polar Observation. *Bulletin of the American Meteorological Society*, *93*(10), 1519–1537. https://doi.org/10.1175/BAMS-D-11-00015.1

Lehning, M., Bartelt, P., Brown, B., Fierz, C., & Satyawali, P. (2002). A physical SNOWPACK model for the Swiss avalanche warning Part II. Snow microstructure. *Cold Regions Science and Technology*, *35*, 147–167. https://doi.org/10.1016/S0165-232X(02)00073-3

Li, L., & Pomeroy, J. W. (1997). Estimates of Threshold Wind Speeds for Snow Transport Using Meteorological Data. *Journal of Applied Meteorology*, *36*(3), 205–213. https://doi.org/10.1175/1520-0450(1997)036<0205:EOTWSF>2.0.CO;2

Lillesand, T., Kiefer, R. W., & Chipman, J. (2015). *Remote sensing and image interpretation*. John Wiley & Sons. https://books.google.com/books?hl=en&lr=&id=AFHDCAAAQBAJ&oi=

fnd&pg=PR12&dq=Lillesand+et+al.+(2015&ots=0Ertk-fDbu&sig=X7z42lDLZfLXxv3OSj0VV-JOfnI

Lindsay, R., Wensnahan, M., Schweiger, A., & Zhang, J. (2014). Evaluation of seven different atmospheric reanalysis products in the arctic. *Journal of Climate*, *27*(7), 2588–2606. https://doi.org/10.1175/JCLI-D-13-00014.1

Liston, G. E., Haehnel, R. B., Sturm, M., Hiemstra, C. A., Berezovskaya, S., & Tabler, R. D. (2007). Simulating complex snow distributions in windy environments using SnowTran-3D. *Journal of Glaciology*, *53*(181), 241–256. https://doi.org/10.3189/172756507782202865

Liu, C. Y., Kuo, S. C., Lim, A. H. N., Hsu, S. C., Tseng, K. H., Yeh, N. C., & Yang, Y. C. (2016). Optimal use of space-borne advanced infrared and microwave soundings for regional numerical weather prediction. *Remote Sensing*, *8*(10). https://doi.org/10.3390/rs8100816

Luojus, K., Pulliainen, J., Takala, M., Lemmetyinen, J., Mortimer, C., Derksen, C., Mudryk, L., Moisander, M., Hiltunen, M., Smolander, T., Ikonen, J., Cohen, J., Salminen, M., Norberg, J., Veijola, K., & Venäläinen, P. (2021). GlobSnow v3.0 Northern Hemisphere snow water equivalent dataset. *Scientific Data*, *8*(1), 163. https://doi.org/10.1038/s41597-021-00939-2

Ma, Y., & Pinker, R. T. (2012). Modeling shortwave radiative fluxes from satellites. *Journal of Geophysical Research: Atmospheres*, *117*(D23). https://doi.org/10.1029/2012JD018332

Mätzler, C. (1987). Applications of the interaction of microwaves with the natural snow cover. *Remote Sensing Reviews*. https://doi.org/10.1080/02757258709532086

Mätzler, C. (1998). Microwave Permittivity of Dry Sand. *IEEE Transactions on Geoscience and Remote Sensing*, *36*(1), 317–319. https://doi.org/10.1109/36.655342

Mätzler, C. (2008). Physical principles of remote sensing. *Physical Principles of Remote Sensing*. https://doi.org/10.1016/0031-9201(91)90165-e

Matzler, C., Wiesmann, A., & Strozzi, T. (2000). Simulation of microwave emission and backscattering of layered snowpacks by a radiative transfer model, and validation by surface-based experiments. *International Geoscience and Remote Sensing Symposium (IGARSS)*. https://doi.org/10.1109/igarss.2000.857268

Met Office. (2016). *NWP-Global: Operational Numerical Weather Prediction (NWP) output from the UK Met Office Global Atmospheric Unified Model (UM).* Centre for Environmental Data Analysis. http://catalogue.ceda.ac.uk/uuid/e4ac04e7fa2541278ad4ad06fb4fd5f3

Mizukami, N., P. Clark, M., G. Slater, A., D. Brekke, L., M. Elsner, M., R. Arnold, J., & Gangopadhyay, S. (2013). Hydrologic Implications of Different Large-Scale Meteorological Model Forcing Datasets in Mountainous Regions. *Journal of Hydrometeorology*, *15*(1), 474–488. https://doi.org/10.1175/jhm-d-13-036.1

Montpetit, B., Royer, A., Langlois, A., Cliche, P., Roy, A., Champollion, N., Picard, G., Domine, F., & Obbard, R. (2012). New shortwave infrared albedo measurements for snow specific surface area retrieval. *Journal of Glaciology*, *58*(211), 941–952. https://doi.org/10.3189/2012JoG11J248

Mooney, P. A., Mulligan, F. J., & Fealy, R. (2011). *Comparison of ERA-40 , ERA-Interim and NCEP / NCAR reanalysis data with observed surface air temperatures over Ireland*. *557*(February 2010), 545–557. https://doi.org/10.1002/joc.2098

Mortimer, C., Mudryk, L., Derksen, C., Luojus, K., Brown, R., Kelly, R., & Tedesco, M. (2020). Evaluation of long-term Northern Hemisphere snow water equivalent products. *The Cryosphere*, *14*(5), 1579–1594. https://doi.org/10.5194/tc-14-1579-2020

Nicolas, J. P., & Bromwich, D. H. (2014). New reconstruction of antarctic near-surface temperatures: Multidecadal trends and reliability of global reanalyses. *Journal of Climate*. https://doi.org/10.1175/JCLI-D-13-00733.1

Notz, D., & Stroeve, J. (2016). Observed Arctic sea-ice loss directly follows anthropogenic CO2 emission. *Science*. https://doi.org/10.1126/science.aag2345

Olauson, J. (2018). ERA5: The new champion of wind power modelling? *Renewable Energy*, *126*, 322–331. https://doi.org/10.1016/j.renene.2018.03.056

Oleson, K., Bonan, G. B., Levis, S., Thornton, P., Vertenstein, M., & Yang, Z. (2010). Technical Description of the Community Land Model (CLM). *NCAR Technical Note*. https://doi.org/10.5065/D6N877R0

Osborne, E., Richter-Menge, J., & Jeffries, M. (2018). Arctic Report Card 2018. *NOAA*.

Østby, T. I., Schuler, T. V., & Westermann, S. (2014). Severe cloud contamination of MODIS Land Surface Temperatures over an Arctic ice cap, Svalbard. *Remote Sensing of Environment*, *142*, 95–102. https://doi.org/10.1016/j.rse.2013.11.005

Picard, G., Royer, A., Arnaud, L., & Fily, M. (2014). Influence of meter-scale wind-formed features on the variability of the microwave brightness temperature around Dome C in Antarctica. *The Cryosphere*, *8*(3), 1105–1119. https://doi.org/10.5194/tc-8-1105-2014

Picard, G., Sandells, M., & Löwe, H. (2018). SMRT: An active–passive microwave radiative transfer model for snow with multiple microstructure and scattering formulations (v1.0). *Geoscientific Model Development*, *11*(7), 2763–2788. https://doi.org/10.5194/gmd-11-2763-2018

Pimentel, D., Musilek, P., & Knight, A. (2010). Energy harvesting simulation for automatic arctic monitoring stations. *EPEC 2010 - IEEE Electrical Power and Energy Conference: 'Sustainable Energy for an Intelligent Grid'*, 1–6. https://doi.org/10.1109/EPEC.2010.5697232

Piotrowski, P., Baczyński, D., Kopyt, M., Szafranek, K., Helt, P., & Gulczyński, T. (2019). Analysis of forecasted meteorological data (NWP) for efficient spatial forecasting of wind power generation. *Electric Power Systems Research*, *175*, 105891. https://doi.org/10.1016/j.epsr.2019.105891

Pithan, F., & Mauritsen, T. (2014). Arctic amplification dominated by temperature feedbacks in contemporary climate models. *Nature Geoscience*, *7*(3), 181–184. https://doi.org/10.1038/ngeo2071

Pomeroy, J. W., Marsh, P., & Gray, D. M. (1997). Application of a distributed blowing snow model to the Arctic. *Hydrological Processes*, *11*(11), 1451–1464. https://doi.org/10.1002/(SICI)1099-1085(199709)11:11<1451::AID-HYP449>3.0.CO;2-Q

Pradhanang, S. M., Anandhi, A., Mukundan, R., Zion, M. S., Pierson, D. C., Schneiderman, E. M., Matonse, A., & Frei, A. (2011). Application of SWAT model to assess snowpack development and streamflow in the Cannonsville watershed, New York, USA. *Hydrological Processes*, *25*(21), 3268–3277. https://doi.org/10.1002/hyp.8171

Raleigh, M. S., Livneh, B., Lapo, K., & Lundquist, J. D. (2016). How Does Availability of Meteorological Forcing Data Impact Physically Based Snowpack Simulations? *Journal of Hydrometeorology*, *17*(1), 99–120. https://doi.org/10.1175/JHM-D-14-0235.1

Raup, B. H., Andreassen, L. M., Bolch, T., & Bevan, S. (2014). Remote sensing of glaciers. In *Remote Sensing of the Cryosphere*. https://doi.org/10.1002/9781118368909.ch7

Réveillet, M., Dumont, M., Gascoin, S., Lafaysse, M., Nabat, P., Ribes, A., Nheili, R., Tuzet, F., Ménégoz, M., & Morin, S. (2022). Black carbon and dust alter the response of mountain snow cover under climate change. *Nature Communications*, *13*(1), 5279.

Rohrer, M., Brönnimann, S., Martius, O., Raible, C. C., Wild, M., & Compo, G. P. (2018). Representation of extratropical cyclones, blocking anticyclones, and alpine circulation types in multiple reanalyses and model simulations. *Journal of Climate*. https://doi.org/10.1175/JCLI-D-17-0350.1

Roy, A., Picard, G., Royer, A., Montpetit, B., Dupont, F., Langlois, A., Derksen, C., & Champollion, N. (2013). Brightness Temperature Simulations of the Canadian Seasonal Snowpack Driven by Measurements of the Snow Specific Surface Area. *IEEE Transactions on Geoscience and Remote Sensing*, *51*(9), 4692–4704. IEEE

Transactions on Geoscience and Remote Sensing. https://doi.org/10.1109/TGRS.2012.2235842

Royer, A., Domine, F., Roy, A., Langlois, A., Marchand, N., & Davesne, G. (2021). New northern snowpack classification linked to vegetation cover on a latitudinal mega-transect across northeastern Canada. *Écoscience*, *28*(3–4), 225–242. https://doi.org/10.1080/11956860.2021.1898775

Ryan, W. A., Doesken, N. J., & Fassnacht, S. R. (2008). Evaluation of ultrasonic snow depth sensors for U.S. snow measurements. *Journal of Atmospheric and Oceanic Technology*. https://doi.org/10.1175/2007JTECHA947.1

Saha, S., Moorthi, S., Pan, H. L., Wu, X., Wang, J., Nadiga, S., Tripp, P., Kistler, R., Woollen, J., Behringer, D., Liu, H., Stokes, D., Grumbine, R., Gayno, G., Wang, J., Hou, Y. T., Chuang, H. Y., Juang, H. M. H., Sela, J., … Goldberg, M. (2010). Supplement to the NCEP Climate Forecast System Reanalysis. *Bulletin of the American Meteorological Society*. https://doi.org/10.1175/2010BAMS3001.2

Sandells, M., Essery, R., Rutter, N., Wake, L., Leppänen, L., & Lemmetyinen, J. (2017). Microstructure representation of snow in coupled snowpack and microwave emission models. *The Cryosphere*, *11*(1), 229–246. https://doi.org/10.5194/tc-11-229-2017

Sandells, M., Rutter, N., Wivell, K., Essery, R., Fox, S., Harlow, C., Picard, G., Roy, A., Royer, A., & Toose, P. (2024). Simulation of Arctic snow microwave emission in surface-sensitive atmosphere channels. *The Cryosphere*, *18*(9), 3971–3990. https://doi.org/10.5194/tc-18-3971-2024

Santi, E., Paloscia, S., Pampaloni, P., Pettinato, S., Brogioni, M., Xiong, C., & Crepaz, A. (2017). Analysis of Microwave Emission and Related Indices over Snow using Experimental Data and a Multilayer Electromagnetic Model. *IEEE Transactions on Geoscience and Remote Sensing*. https://doi.org/10.1109/TGRS.2016.2636363

Screen, J. A., & Simmonds, I. (2013). Exploring links between Arctic amplification and mid-latitude weather. *Geophysical Research Letters*. https://doi.org/10.1002/grl.50174

Serreze, M. C., Barrett, A. P., Stroeve, J. C., Kindig, D. N., & Holland, M. M. (2009). The Emergence of Surface-Based Arctic Amplification'. *The Cryosphere*, *3*(1), 11–19. https://doi.org/10.5194/tc-3-11-2009.

Sevruk, B., Ondrás, M., & Chvíla, B. (2009). The WMO precipitation measurement intercomparisons. *Atmospheric Research*, *92*(3), 376–380. https://doi.org/10.1016/j.atmosres.2009.01.016

Singarayer, J. S., & Valdes, P. J. (2010). High-latitude climate sensitivity to ice-sheet forcing over the last 120 kyr. *Quaternary Science Reviews*. https://doi.org/10.1016/j.quascirev.2009.10.011

Skiles, S. M., & Painter, T. H. (2019). Toward Understanding Direct Absorption and Grain Size Feedbacks by Dust Radiative Forcing in Snow With Coupled Snow Physical and Radiative Transfer Modeling. *Water Resources Research*, *55*(8), 7362–7378. https://doi.org/10.1029/2018WR024573

Slater, A. G., Barrett, A. P., Clark, M. P., Lundquist, J. D., & Raleigh, M. S. (2013). Uncertainty in seasonal snow reconstruction: Relative impacts of model forcing and image availability. *Advances in Water Resources*, *55*, 165–177. https://doi.org/10.1016/j.advwatres.2012.07.006

Smith, W., Weisz, E., & Revercomb, H. (2015). The retrieval of atmospheric profiles from satellite radiances for NWP data assimilation. *Proc. 20th Int. TOVS Study Conf., Lake Geneva, WI, International TOVS Working Group*, *4*.

Stearns, C. R., Keller, L. M., Weidner, G. A., & Sievers, M. (1993). Monthly Mean Climatic Data for Antarctic Automatic Weather Stations. In *Antarctic Meteorology and Climatology: Studies Based on Automatic Weather Stations* (pp. 1–21). American Geophysical Union (AGU). https://doi.org/10.1029/AR061p0001

Stuecker, M. F., Bitz, C. M., Armour, K. C., Proistosescu, C., Kang, S. M., Xie, S. P., Kim, D., McGregor, S., Zhang, W., Zhao, S., Cai, W., Dong, Y., & Jin, F. F. (2018). Polar amplification dominated by local forcing and feedbacks. In *Nature Climate Change*. https://doi.org/10.1038/s41558-018-0339-y

Sturm, M., Holmgren, J., & Liston, G. E. (1995). A seasonal snow cover classification system for local to global applications. *Journal of Climate*. https://doi.org/10.1175/1520-0442(1995)008<1261:ASSCCS>2.0.CO;2

Sun, H., & Xu, Q. (2021). Evaluating Machine Learning and Geostatistical Methods for Spatial Gap-Filling of Monthly ESA CCI Soil Moisture in China. *Remote Sensing*, *13*(14), 2848. https://doi.org/10.3390/rs13142848

Takala, M., Luojus, K., Pulliainen, J., Derksen, C., Lemmetyinen, J., Kärnä, J.-P., Koskinen, J., & Bojkov, B. (2011). Estimating northern hemisphere snow water equivalent for climate research through assimilation of space-borne radiometer data and ground-based measurements. *Remote Sensing of Environment*, *115*(12), 3517–3529. https://doi.org/10.1016/j.rse.2011.08.014

Tang, Q., Gao, H., Lu, H., & Lettenmaier, D. P. (2009). Remote sensing: Hydrology. *Progress in Physical Geography*. https://doi.org/10.1177/0309133309346650

Tavolato, C., & Isaksen, L. (2010). ERA report series: Data usage and quality control for ERA-40, ERA-Interim and the operational ECMWF data assimilation system. *ERA Report Series*.

Terzago, S., Andreoli, V., Arduini, G., Balsamo, G., Campo, L., Cassardo, C., Cremonese, E., Dolia, D., Gabellani, S., von Hardenberg, J., Morra di Cella, U., Palazzi, E., Piazzi, G., Pogliotti, P., & Provenzale, A. (2020). Sensitivity of snow models to the accuracy of meteorological forcings in mountain environments. *Hydrology and Earth System Sciences*, *24*(8), 4061–4090. https://doi.org/10.5194/hess-24-4061-2020

Thépaut, J.-N., & Kelly, G. A. (2006). *Assimilation only surface pressure observations in 3D and 4DVAR*.

Tomlinson, C. J., Chapman, L., Thornes, J. E., & Baker, C. (2011). Remote sensing land surface temperature for meteorology and climatology: A review. In *Meteorological Applications*. https://doi.org/10.1002/met.287

Trail Valley Creek Research Station. (2025). https://nwtresearch.com/projects/environment/trail-valley-creek-research-station

Ulaby, F. T., Moore, R. K., & Fung, A. K. (1981). Microwave remote sensing: Active and passive. Volume I: microwave remote sensing fundamentals and radiometry. *Microwave Remote Sensing: Active and Passive. Volume I: Microwave Remote Sensing Fundamentals and Radiometry.*

Ulaby, F. T., Moore, R. K., & Fung, A. K. (1986). Microwave remote sensing: Active and passive. Volume III: from theory to applications. *Microwave Remote Sensing: Active and Passive. Volume III: From Theory to Applications.*

Vargel, C., Royer, A., St-Jean-Rondeau, O., Picard, G., Roy, A., Sasseville, V., & Langlois, A. (2020). Arctic and subarctic snow microstructure analysis for microwave brightness temperature simulations. *Remote Sensing of Environment*, *242*, 111754. https://doi.org/10.1016/j.rse.2020.111754

Vionnet, V., Brun, E., Morin, S., Boone, A., Faroux, S., Le Moigne, P., Martin, E., & Willemet, J.-M. (2012). The detailed snowpack scheme Crocus and its implementation in SURFEX v7.2. *Geoscientific Model Development*, *5*(3), 773–791. https://doi.org/10.5194/gmd-5-773-2012

Vionnet, V., Mortimer, C., Brady, M., Arnal, L., & Brown, R. (2021). Canadian historical Snow Water Equivalent dataset (CanSWE, 1928–2020). *Earth System Science Data*, *13*(9), 4603–4619. https://doi.org/10.5194/essd-13-4603-2021

Viviroli, D., Archer, D. R., Buytaert, W., Fowler, H. J., Greenwood, G. B., Hamlet, A. F., Huang, Y., Koboltschnig, G., Litaor, M. I., López-Moreno, J. I., Lorentz, S., Schädler, B., Schreier, H., Schwaiger, K., Vuille, M., & Woods, R. (2011). Climate change and mountain water resources: Overview and recommendations for research, management and policy. *Hydrology and Earth System Sciences*, *15*(2), 471–504. https://doi.org/10.5194/hess-15-471-2011

Walker, B., Wilcox, E. J., & Marsh, P. (2021). Accuracy assessment of late winter snow depth mapping for tundra environments using Structure-

from-Motion photogrammetry. *Arctic Science*, *7*(3), 588–604. https://doi.org/10.1139/as-2020-0006

Walters, D., Baran, A. J., Boutle, I., Brooks, M., Earnshaw, P., Edwards, J., Furtado, K., Hill, P., Lock, A., Manners, J., Morcrette, C., Mulcahy, J., Sanchez, C., Smith, C., Stratton, R., Tennant, W., Tomassini, L., Van Weverberg, K., Vosper, S., … Zerroukat, M. (2019). The Met Office Unified Model Global Atmosphere 7.0/7.1 and JULES Global Land 7.0 configurations. *Geoscientific Model Development*, *12*(5), 1909–1963. https://doi.org/10.5194/gmd-12-1909-2019

Wang, C., Graham, R. M., Wang, K., Gerland, S., & Granskog, M. A. (2019). Comparison of ERA5 and ERA-Interim near-surface air temperature, snowfall and precipitation over Arctic sea ice: Effects on sea ice thermodynamics and evolution. *The Cryosphere*, *13*(6), 1661–1679. https://doi.org/10.5194/tc-13-1661-2019

Waqas, M., Humphries, U. W., Chueasa, B., & Wangwongchai, A. (2024). Artificial intelligence and numerical weather prediction models: A technical survey. *Natural Hazards Research*, S266659212400091X. https://doi.org/10.1016/j.nhres.2024.11.004

Warszawski, L., Frieler, K., Huber, V., Piontek, F., Serdeczny, O., & Schewe, J. (2014). The Inter-Sectoral Impact Model Intercomparison Project (ISI–MIP): Project framework. *Proceedings of the National Academy of Sciences*, *111*(9), 3228–3232. https://doi.org/10.1073/pnas.1312330110

Weedon, G. P., Balsamo, G., Bellouin, N., Gomes, S., Best, M. J., & Viterbo, P. (2014). The WFDEI meteorological forcing data set: WATCH Forcing Data methodology applied to ERA-Interim reanalysis data. *Water Resources Research*, *50*(9), 7505–7514. https://doi.org/10.1002/2014wr015638

Wegmuller, U., & Matzler, C. (1999). Rough bare soil reflectivity model. *IEEE Transactions on Geoscience and Remote Sensing*, *37*(3), 1391–1395. IEEE Transactions on Geoscience and Remote Sensing. https://doi.org/10.1109/36.763303

Weng, F., Zhao, L., Ferraro, R. R., Poe, G., Li, X., & Grody, N. C. (2003). Advanced microwave sounding unit cloud and precipitation algorithms.

In *Radio Science* (Vol. 38, Issue 4). https://doi.org/10.1029/2002rs002679

Westermann, S., Langer, M., Boike, J., Heikenfeld, M., Peter, M., Etzelmüller, B., & Krinner, G. (2016). *Simulating the thermal regime and thaw processes of ice-rich permafrost ground with the land-surface model CryoGrid 3*. 523–546. https://doi.org/10.5194/gmd-9-523-2016

Williamson, S. N., Hik, D. S., Gamon, J. A., Jarosch, A. H., Anslow, F. S., Clarke, G. K. C., & Scott Rupp, T. (2017). Spring and summer monthly MODIS LST is inherently biased compared to air temperature in snow covered sub-Arctic mountains. *Remote Sensing of Environment*, *189*, 14–24. https://doi.org/10.1016/j.rse.2016.11.009

Wivell, K., Fox, S., Sandells, M., Harlow, C., Essery, R., & Rutter, N. (2023). Evaluating Snow Microwave Radiative Transfer (SMRT) model emissivities with 89 to 243 GHz observations of Arctic tundra snow. *The Cryosphere*, *17*(10), 4325–4341. https://doi.org/10.5194/tc-17-4325-2023

Yoshida, Z. (1955). Physical studies on deposited snow, I.Thermal properties. *Contributions from the Institute of Low Temperature Science, Ser.A.*, *7*, 19–74.

Yoshida, Z. (1963). Physical properties of snow. *Ice and Snow*.

Zhang, Y., Hou, J., & Huang, C. (2022). Integration of Satellite-Derived and Ground-Based Soil Moisture Observations for a Precipitation Product over the Upper Heihe River Basin, China. *Remote Sensing*, *14*(21), 5355. https://doi.org/10.3390/rs14215355

Zheng, X., Li, X., Jiang, T., Ding, Y., Wu, L., Zhang, S., & Zhao, K. (2016). Retrieving soil surface temperature under snowpack using special sensor microwave/imager brightness temperature in forested areas of Heilongjiang, China: An improved method. *Journal of Applied Remote Sensing*, *10*(2), 1–10. https://doi.org/10.1117/1.JRS.10.026016